https://ntrs.nasa.gov/search.jsp?R=19770008019 2020-03-22T12:27:25+00:00Z

X-661-76-280

NASA TM X- 71247

# HERCULES X-1: SPECTRAL VARIABILITY OF AN X-RAY PULSAR IN A STELLAR BINARY SYSTEM

(NASA-TM-X-71247) HERCULES X-1: SPECTRAL VARIABILITY OF AN X-RAY PULSAR IN A STELLAR BINARY SYSTEM Ph.D. Thesis (NASA) 168 p HC A08/MF A01 CSCL 03A

N77-14962

Unclas G3/89 58324

STEVEN HOWARD PRAVDO

JAN 1977 RECEIVED NASA STI FACILITY INPUT BRANCH

DECEMBER 1976

GSFC

GODDARD SPACE FLIGHT CENTER

GREENBELT, MARYLAND

For information concerning availability
of this document contact.

Technical Information & Administrative Support Division
Code 250
Goddard Space Flight Center
Greenbelt, Maryland 20771

(Telephone 301–982–4488)

"This paper presents the views of the author(s), and does not necessarily reflect the views of the Goddard Space Flight Center, or NASA."

# HERCULES X-1: SPECTRAL VARIABILITY OF AN X-RAY PULSAR IN A STELLAR BINARY SYSTEM*

by
Steven Howard Pravdo

Dissertation submitted to the Faculty of the Graduate School
of the University of Maryland in partial fulfillment
of the requirements for the degree of
Doctor of Philosopy
1976

*Work supported by NASA Grant NGR 21-002-316

APPROVAL SHEET

Title of Thesis: Hercules X-1: Spectral Variability of an X-ray Pulsar in a Stellar Binary System

Name of Candidate: Steven Pravdo
Doctor of Philosophy, 1976

Thesis and Abstract Approved:

Frank B. McDonald
Professor (Part-time)
Department of Physics

Date Approved:

VITA

Name: Steven Howard Pravdo

Permanent address: 8507 Greenbelt Road, Greenbelt, Maryland 20770

Degree and date to be conferred: Ph.D., 1976

Date of birth: [redacted]

Place of birth: [redacted]

Secondary education: East Brunswick High School, 1968

| Collegiate institutions attended | Dates | Degree | Date of Degree |
|---|---|---|---|
| Haverford College | 1968-1972 | B.S. | May 1972 |
| University of Maryland | 1972-1976 | M.S. | August 1974 |
| University of Maryland | 1972-1976 | Ph.D. | December 1976 |

Major: Physics, Astronomy

Publications:

"K-alpha X-rays from Cosmic Ray Oxygen", S. H. Pravdo and E. A. Boldt, Astrophysical Journal (Ap.J.), 200, 727, 1975.

"Her X-1 OSO-8 GSFC Results", S. H. Pravdo, R. H. Becker, E. A. Boldt, S. S. Holt, R. E. Rothschild, P. J. Serlemitsos, and J. H. Swank, X-ray Binaries, NASA SP-389, 1976.

"Cen X-3 OSO-8 GSFC Results", J. H. Swank, R. H. Becker, E. A. Boldt, S. S. Holt, S. H. Pravdo, R. E. Rothschild, and P. J. Serlemitsos, X-ray Binaries, NASA SP-389, 1976.

"X-ray Results OSO-8", P. J. Serlemitsos, R. H. Becker, E. A. Boldt, S. S. Holt, S. H. Pravdo, R. E. Rothschild, P. J. Serlemitsos, and J. H. Swank, X-ray Binaries, NASA SP-389, 1976.

"Observation Programs OSO-8", R. H. Becker, E. A. Boldt, S. S. Holt, S. H. Pravdo, R. E. Rothschild, P. J. Serlemitsos, and J. H. Swank, X-ray Binaries, NASA SP-389, 1976.

"Iron Line Emission from a High Temperature Plasma in Cas A", S. H. Pravdo, R. H. Becker, E. A. Boldt, S. S. Holt, R. E. Rothschild, P. J. Serlemitsos, and J. H. Swank, Ap. J. (Letters) 206, L41, 1976.

"Spectral Variability in the X-ray Pulsar GX 1+4", R. H. Becker, E. A. Boldt, S. S. Holt, S. H. Pravdo, R. E. Rothschild, R. E. Rothschild, P. J. Serlemitsos, and J. H. Swank, Ap. J.(Letters) 207; L167, 1976.

"X-ray Observations of the Vela Pulsar: Statistics and Spectrum", S. H. Pravdo, R. H. Becker, E. A. Boldt, S. S. Holt, R. E. Rothschild, P. J. Serlemitsos, and J. H. Swank, Ap. J.(Letters) 208, L67, 1976.

"Variations in the Spectra and Pulse Period of GX301-2", J. H. Swank, S. H. Pravdo, R. H. Becker, E. A. Boldt, S. S. Holt, R. E. Rothschild, P. J. Serlemitsos, and J. H. Swank, Ap. J. 209, in press.

"X-ray Emission from the Supernova Remnant G287.8-0.5", R. H. Becker, E. A. Boldt, S. S. Holt, S. H. Pravdo, R. H. Rothschild, P. J. Serlemitsos, and J. H. Swank, Ap. J. 209, in press.

"Evidence for a 17-d Periodicity from Cyg X-3", S. S. Holt, E. A. Boldt, P. J. Serlemitsos, L. J. Kaluzienski, S. H. Pravdo, A. Peacock, M. Elvis, M. G. Watson, and K. A. Pounds, Nature 160, 592, 1976.

"Spectral Evolution of a Long X-ray Burst", J. H. Swank, R. H. Becker, E. A. Boldt, S. S. Holt, S. H. Pravdo, P. J. Serlemitsos, to be published in Ap. J., 1976.

"Spectra of Her X-1 Near a Turn-on in the 35-day Cycle", R. H. Becker, E. A. Boldt, S. S. Holt, S. H. Pravdo, R. E. Rothschild, P. J. Serlemitsos, B. H. Smith, J. H. Swank, to be published in Ap. J.,

Positions held: Post-doctoral Research Associate
Laboratory for High Energy Astrophysics
NASA/Goddard Space Flight Center
Greenbelt, Maryland 20771

ACKNOWLEDGMENTS

I wish to thank Dr. Frank McDonald, my thesis advisor, for giving me the opportunity to conduct this research with the X-ray Group of the Laboratory for High Energy Astrophysics at NASA/Goddard Space Flight Center, and for his critical appraisal of this work. I would also like to thank Dr. Howard Laster and Dr. Alexander Dragt, the former and present Chairman of the Department of Physics and Astronomy at the University of Maryland, who have approved this research position.

In the X-ray Group, I would especially like to acknowledge Dr. Peter Serlemitsos and Dr. Elihu Boldt for helping to make my graduate research both productive and enjoyable. Dr. Stephen Holt, Dr. Richard Rothschild, Dr. Robert Becker, and Dr. Jean Swank are also thanked for their valuable assistance.

In the construction and testing of the experiment on OSO-8, I note Messrs. C. Glasser, F. Birsa, T. Kaminski, L. Noordzy, S. Jones, and E. Mundy I also thank Ms. Julie Saba as well for my introduction to the X-ray Group.

The drafting department, Messrs. A. Thompson, H. Trexel, and F. Shaffer, provided excellent support. Also Ms. Barbara Dallas, Ms. Barbara Shavatt, and certainly Ms. Sandra Shrader, who typed this manuscript, are acknowledged for their good-natured assistance.

The people involved in the OSO-8 data analysis software--Mr. L. Perrazoli, Mr. P. Yu, Dr. A. Stottlemyer, Mr. A. Chatterjee, Ms. K. Tolbert, and Ms. S. Gutt--are also thanked.

Mr. Roger Bussard is acknowledged for many simulating discussions.

TABLE OF CONTENTS


| Chapter | | Page |
|---|---|---|
| ACKNOWLEDGMENTS | | ii |
| LIST OF TABLES | | v |
| LIST OF FIGURES | | vi |
| I. | INTRODUCTION | 1 |
| | A. X-ray Astronomy | 1 |
| | B. X-ray Production Mechanisms | 7 |
| | C. X-ray Binaries | 17 |
| | D. Hercules X-1 | 23 |
| II. | EXPERIMENT | 33 |
| | A. General Description | 33 |
| | B. The Detectors | 35 |
| | C. The Photoelectric and Other Physical Effects | 39 |
| | D. Fields of View | 44 |
| | E. Data System | 46 |
| | F. Data Transmission | 49 |
| III. | OBSERVATIONS AND ANALYSIS | 51 |
| | A. Observations | 51 |
| | B. Methods of Analysis | 54 |
| IV. | RESULTS | 61 |
| | A. Binary Period | 62 |
| | B. Pulsations | 65 |
| | C. High-Low Cycle | 71 |

Chapter Page

V. DISCUSSION. . . . . 74

A. HZ Herculis . . . . . 74

B. Accretion Disk. . . . . 76

C. Iron Band Emission. . . . . 78

D. Alfvén Surface. . . . . 80

E. Hercules X-1. . . . . 82

F. Spectrum. . . . . 88

G. Summary . . . . . 89

APPENDIX A. CXS RESPONSE FUNCTION . . . . . 92

APPENDIX B. CHARGE EXCHANGE FROM ACCRETING MATTER . . . . . 96

REFERENCES . . . . . 98

LIST OF TABLES


| Table | | Page |
|---|---|---|
| 1-1 | Atomic Line Energies of Abundant Elements in the Hard X-Ray Range. . . . . | 105 |
| 1-2 | Fluorescence Yields and Abundances Relative to Hydrogen of Abundant Elements . . . . . | 106 |
| 2-1 | Characteristics of the OSO-8 Detector Complement. . . . . | 107 |
| 3-1 | Chi Squared Versus Degrees of Freedom (from Handbook of Chemistry and Physics 1963). . . . . | 108 |
| 3-2 | Confidence Limits on Deviations from Minimum Acceptable Chi Squared. . . . . | 109 |
| 4-1 | Temporal Boundaries of Spectra by Binary Phase. . . . . | 110 |
| 4-2 | Line Energies and Equivalent Widths (keV) of Spectra by Binary Phase . . . . . | 111 |
| 4-3 | Parameters of HER X-1 Spectra Observed with Xenon (A) Detector. . . . . | 112 |

FIGURE CAPTIONS


| Figure | | Page |
|---|---|---|
| 1-1 | Orbiting Solar Observatory 8. . . . . | 113 |
| 1-2 | Iron Photoelectric Absorption Cross Section (from Hubble 1971). . . . . | 114 |
| 1-3 | Schematic Representation of the Hercules X-1 Periodicities . . . . . | 115 |
| 2-1 | Cosmic X-ray Spectroscopy Experiment (CXS) View Looking Inboard . . . . . | 116 |
| 2-2 | CXS View Looking Forward at Aft Side of Shelf . . . . . | 117 |
| 2-3 | CXS View Looking Aft at Forward Side of Shelf . . . . . | 118 |
| 2-4 | Signal Handling of OSO-I Detectors. . . . . | 119 |
| 2-5 | OSO Detector Window Transmission. . . . . | 120 |
| 2-6 | Block Diagram of Experiment . . . . . | 121 |
| 2-7 | Xenon Photoelectric Absorption Cross Section (from Hubble 1971). . . . . | 122 |
| 2-8 | B Detector Collimator Response of 25 keV Bremsstrahlung Radiation . . . . . | 123 |
| 2-9 | Arrangement of Cosmic X-ray Experiment. . . . . | 124 |
| 2-10 | Representation of the OSO-8 Spin Axis Path Including the Observation of Hercules X-1 (Source Code BN) which is Centered in a Five Degree Circle . . . . . | 125 |
| 2-11 | Data System, Part 1 . . . . . | 126 |
| 2-12 | Data System, Part 2 . . . . . | 127 |
| 2-13 | A-D Converter Transfer Function (A and C) . . . . . | 128 |
| 3-1 | Plot of the CXS Count Rates from Detectors A, B, and C Showing Areas of Enhanced Precipitating Particle Contamination . . . . . | 129 |

| Figure | | Page |
|---|---|---|
| 4-1 | Background-Subtracted Counting Rate of Hercules X-1 in the Xenon (A) Detector Versus Day of Year. . . . . | 130 |
| 4-2 | Background-Subtracted Counting Rate of Hercules X-1 in the Argon (B) Detector Versus Day of Year. . . . . | 131 |
| 4-3 | Her X-1 RL2. Spectrum of Hercules X-1 for Times Defined in Table 4-1. . . . . | 132 |
| 4-4 | Her X-1 RN1. Spectrum of Hercules X-1 for Times Defined in Table 4-1. . . . . | 133 |
| 4-5 | Her X-1 Light Curves for High State in Five Energy Bands . . . . . | 134 |
| 4-6 | Rates During Transition from Eclipse. . . . . | 135 |
| 4-7 | RL Pulse Shape Defining the Pulse Regions . . . . . | 136 |
| 4-8 | RN Pulse Shape Defining the Pulse Regions . . . . . | 137 |
| 4-9 | RN Pulse Shape by Binary Phase. . . . . | 138 |
| 4-10 | RL Pulse Light Curve in Six Energy Bands . . . . . | 139 |
| 4-11 | Spectrum by Pulse Phase . . . . . | 140 |
| 4-12 | Her X-1 RL:OP Off Pulse Spectrum. . . . . | 141 |
| 4-13 | Hercules X-1 RL:FP1 First Half of First Peak with Off Pulse Background. . . . . | 142 |
| 4-14 | Hercules X-1 RN:FP2 Second Half of First Peak with Eclipse Background. . . . . | 143 |
| 4-15 | Hercules X-1 RN:SP Second Peak Spectrum with Pulse Minimum Background. . . . . | 144 |
| 4-16 | Her X-1 RL:PM Pulse Minimum Spectrum. . . . . | 145 |
| 4-17 | Hercules Dip Pulse Profiles . . . . . | 146 |
| 4-18 | Spectra of Hercules X-1 from Xenon (A) Detector Observations. . . . . | 147 |

| Figure | | Page |
|---|---|---|
| 4-19 | Hercules X-1 RL Dip Spectra . . . . . | 148 |
| 5-1 | Hercules X-1/Hz Herculis System Schematic . . . . . | 149 |
| 5-2 | Tilted and Twisted Accretion Disk . . . . . | 150 |
| 5-3 | Hercules X-1 Spectrum Prior to High State Turn-On Superimposed on Model High State Spectrum Modified by Compton Scattering through Three Optical Depths. . . . | 151 |
| 5-4 | Hercules X-1 Pulse, Scattering Region Optical Depth, and "DeScattered" Pulse . . . . . | 152 |
| 5-5 | Twisted Accretion Column. Dotted Curve Represents Compton Scattering Optical Depth. . . . . | 153 |
| A-1 | OSO-I Detector C-1 Response to Calibration Sources. . . . | 154 |

ABSTRACT

Title of Thesis: Hercules X-1: Spectral Variability of an X-ray Pulsar in a Stellar Binary System

Steven Howard Pravdo, Doctor of Philosophy, 1976

Thesis directed by: Professor Frank B. McDonald

Hercules X-1 is an X-ray pulsar in a stellar binary system. It is believed to be a neutron star. The Goddard Space Flight Center Cosmic X-ray Spectroscopy experiment onboard the earth-orbiting satellite, Orbiting Solar Observatory 8 (OSO-8), observed Her X-1 continuously for $\sim$ 8 days from August 26 to September 3, 1975. Spectral-temporal correlations of the X-ray emission were obtained.

The major results concern observations of 1) iron band emission, 2) spectral hardening (increase in effective X-ray temperature) within the X-ray pulse, and 3) a transition from an X-ray low state to a high state. The spectrum obtained prior to the high state can be interpreted as reflected emission from a hot coronal gas surrounding an accretion disk, which itself shields the primary X-ray source from the line of sight during the low state.

The spectral hardening within the X-ray pulse is probably indicative of the beaming mechanism at the neutron star surface. If the hardest spectrum by pulse phase is identified with the line of sight close to the Her X-1 magnetic dipole axis, then the X-ray "pencil" beam becomes harder with decreasing angle between the line of sight and the dipole axis. The intensity asymmetry in the X-ray pulse can be explained by the attenuation of the beam caused by an intervening region with Compton scattering optical

REPRODUCIBILITY OF THE ORIGINAL PAGE IS POOR

depth $\lesssim 1$. This region could be the accretion column.

The iron band emission is the most puzzling result because the line energies change within the band (5.5 $\sim$ 8.2 keV) without apparent periodicity. Iron line fluorescence provides the correct line intensity if the fluorescing region is a shell of material at the Alfvén radius which is optically thick to Compton scattering. The absence of correlations between the intensity of this feature and binary phase indicates that most of the emission is not produced in the atmosphere of the optical binary companion, HZ Herculis. Alternatively, line emission from the surface of Her X-1 is discussed.

# CHAPTER I

## I. INTRODUCTION

### A. X-ray Astronomy

The first extra-solar-system X-ray source was discovered by R. Giacconi and his colleagues at American Science and Engineering in 1962 during a rocket flight ostensibly designed to observe X-rays from the lunar surface. (Giacconi et al., 1962). Soon afterward this result was confirmed by a group at the Naval Research Laboratory under H. Friedman. Previous observations of X-rays from solar flares had led scientists to believe that other stars would be X-ray sources but at much lower intensities than that actually seen. This first source, later called Sco X-1, was a new class of celestial object whose existence had not been predicted and whose nature is only slowly becoming known. It is not surprising that Sco X-1 has been found to be the brightest steady X-ray source as well as the first. In addition this initial experiment detected a diffuse isotropic celestial X-ray background, again at a much higher level than expected. These two discoveries were the impetus for the development of the field of X-ray astronomy. Since that time a wide variety of strong X-ray sources have been identified. While theoretical models exist for many of these--supernova remnants, binary stellar systems--these models came after the experimental fact.

The earth's atmosphere is opaque to celestial X-rays. As early as post-WWII the technology existed which could place X-ray detectors above substantial portions of the atmosphere. However a celestial X-ray experiment was not performed till much later. In the early 1960s sounding rockets, and later balloons were used to lift experimental payloads to the necessary altitudes. During this period many other bright X-ray sources were discovered ( $\gtrsim$ 40) and improved experimental techniques

were developed. The use of slow-scanning attitude-controlled rockets and modulation collimators led to greater precision in detecting sources and determining their locations. This in turn aided optical and radio astronomers in finding counterparts to the X-ray sources. The first X-ray source identified with a previously known celestial object was the Crab nebula (Bowyer et al., 1964). Galactic sources were found to be of different types. Some were stellar point sources, like Sco X-1. Others were more extended, like the Crab nebula. Spectroscopy became a useful tool in the investigation of X-ray production mechanisms. The X-ray luminosities of these objects was found to be orders of magnitude larger than the total luminosity of the sun. Also, extragalactic objects such as peculiar energetic galaxies had strong X-ray fluxes. Rockets and balloons, however, were limited in the continuing survey of the X-ray sky by experimental considerations. Typical rocket flights last on the order of minutes and can observe only limited areas of the sky. Balloon observations extend over hours but can detect only X-rays with $E \gtrsim 20$ keV because of the low energy attenuation by residual atmosphere. X-ray sources, however, have shown to be variable on time scales from fractions of a second to months. Also, unexpected and dramatic transitions sometimes occur. Ideally, an experiment should have several characteristics: the capability to monitor interesting sources for long time periods; large photon collecting areas; excellent temporal, spatial, and spectral resolution; and the ability to point towards sources undergoing unusual activity. These goals are being attained in part or full by satellite observatories.

UHURU (SAS A) was the first satellite observatory devoted solely to the study of celestial X-rays. It was launched in December 1970 and initiated a great quantum leap forward in the knowledge and understanding

of the X-ray environment. Over 150 X-ray sources were discovered. Periodicities on all time scales were observed. A general picture of the X-ray sky emerged. Several categories of galactic sources existed. Supernova remnants expanding through the interstellar medium created X-rays. The Crab nebula and the Vela remnant are examples of this. Other sources exhibited clear binary properties. Her X-1, Cen X-3, and Vela X-1 have regular eclipses (period $\sim$ days) of their X-ray luminosity leading to their binary interpretation. In addition, many sources of both preceding types are known to pulse on time scales $\lesssim$ 1 second. These short-term periodicities are due to an object, which while not new theoretically (Oppenheimer and Volkoff 1939), is new in terms of experimental justification: the neutron star. Initially the existance of neutron stars was invoked to explain the phenomonom of radio pulsars. Regular radio pulsations from compact objects were explained as periodic views of the magnetic poles of rapidly rotating neutron stars. The Crab pulsar (NP0531) is the fastest known rotator with a 33 msec period.

X-ray pulses from the Crab pulsar at the radio period were first observed by Fritz et al. (1969). The energy released in X-rays from this object is a factor of $\sim 10^5$ larger than the radio power (cf. Gorenstein and Tucker 1974). With this knowledge came the understanding that neutron stars could be important X-ray sources as well as radio sources. The Crab, however, is not a typical neutron star X-ray source. It is a recent supernova (age $\sim 10^3$ yrs.) and is not in a binary stellar system. Rotational energy of the compact object is, without doubt, the energy source for the X-rays. As this energy is radiated away the pulsar slows down in agreement with observations. The Vela pulsar (PSR0833-45) is a likely candidate for similar emission but to date (cf. Pravdo et al., 1976c) the Crab is the only identified X-ray pulsar of this type.

Another variety of X-ray pulsar occurs in binary stellar systems. In addition to regular eclipses of the X-ray source by the normal star, periodic variations in the pulse period as a function of binary phase are well understood as orbital Doppler shifts. This effect was first observed and discussed in the discovery of Her X-1 by Schreier et al. (1972). The energy source for this X-ray emission is thought to be quite different from that in Crab-type objects. In this case, matter from the normal star accretes onto the surface of the collapsed star, and converts with substantial efficiency, its gravitional potential energy into X-rays. For typical neutron star parameters (mass $2 \times 10^{33}$ g $\approx M_{\odot}$, radius $\sim 10^6$ cm) the gravitational potential energy is about ten per cent of the rest mass of the accreting material. Realistic mass transfer rates and conversion efficiencies create sufficient X-ray fluxes to explain high luminosity ($10^{37-38}$ erg $sec^{-1}$) objects (see following Section C). Infalling matter can also transfer angular momentum to the neutron star. This effect is observed as a spin-up in binary pulsars, while as mentioned before, solitary Crab-like pulsars spin down.

There are a wide variety of extra-galactic X-ray sources. Nearby normal galaxies such as M31 (Andromeda) are weak but observable X-ray emitters. Unusual individual galaxies can be strong sources. Cen A, for example, is a strong radio source and has been described as "one of the most peculiar objects in the sky", (Sandage 1961) and was once thought to be the result of two galaxies in collision. It is a strong X-ray source with luminosity of $\sim 10^{43}$ erg $sec^{-1}$ (cf. Serlemitsos et al., 1976). Some Seyfert galaxies (NGC4151) and quasistellar objects (3C273) have been identified as X-ray sources. Discrete sources within the neighboring Large and Small Magellanic clouds have been observed. Clusters of galaxies--Virgo, Coma, Perseus, and many Abell clusters--

emit X-rays, possibly from a hot intra-cluster gas. Finally some part of the diffuse isotropic X-ray background may be locally extra-galactic or even cosmological in origin.

In recent years the second generation of satellite observatories has lead to the discovery of new X-ray phenomona, and to the further understanding of previously known sources. Copernicus (OAO), OSO-7, ANS, Ariel 5, SAS-3, and OSO-8 have all made contributions to this research. The central regions of globular clusters of stars within our galaxy have been identified as X-ray sources (Clark et al., 1976). X-ray pulsars with much longer pulse periods on the order of hundreds of seconds have been discovered (McClintock et al., 1976). Whether these long period pulsars are theoretically similar in principle to the canonical X-ray pulsars is still a topic for discussion. A whole new class of X-ray sources--the burster--has been discovered (Grindlay et al., 1976). These objects exhibit semi-regular high intensity bursts of X-rays lasting on time scales of 10-100 seconds. Even the bursters are not a homogeneous group and different subtypes have been identified (Lewin et al., 1976; Swank et al., 1976b). In X-ray astronomy unexpected phenomena have been discovered with each new experimental capability. The field has been broadened by each satellite observatory. In the future (1977 and on) a series of High energy Astronomical Observatories (HEAO A and B) will be orbited with increased sensitivity and the exciting new possibility of obtaining X-ray images. Some current questions in X-ray astronomy will be answered, and undoubtedly new ones will arise.

This thesis is based on data obtained from Orbiting Solar Observatory 8 (OSO-8). OSO-8 (Figure 1.1) was launched in June 1975 and has completed one year of nearly flawless operations. A second year of observations

has been planned. The Goddard Space Flight Center Cosmic X-ray Spectroscopy experiment (CXS) is one of seven experiments on the satellite. It consists of three gas proportional counter X-ray detectors which are described in Chapter II. As its name implies, a primary goal of the CXS is to obtain spectra of celestial X-ray sources. Because the CXS has moderately large collecting areas and is able to remain pointed at sources for days at a time, many photons can be detected from each source to yield spectra with small statistical errors. In fact, in some cases, systematic errors arising from incomplete knowledge of detector response can exceed pure statistical error. The excellent temporal resolution allows examination of short-term temporal-spectral correlations. Other general experimental goals include detection of weak sources and observations of the diffuse X-ray background.

The purpose of this thesis is to discuss observations of spectral variability in X-ray binaries with particular emphasis on Hercules X-1. Binary stellar systems contain half of the $10^{11}$ stars in the galaxy. However, only $\sim$100 intense X-ray binaries have been discovered. The small number of such sources may be due to small probability for their formation or a short (on galactic time scales $<<10^9$ yr.) X-ray lifetime. They can be useful in the studies of galactic and stellar evolution. Most of the binary X-ray sources are thought to be compact stars--neutron stars and black holes. The creation and properties of these objects have important links with supernova studies and general relativity. Compact stars may be the residue of supernova explosions of normal stars. If this is the case, the properties and very existence of these objects can have significance in the supernova process, which itself can be important in large-scale galactic phenomena (cosmic ray creation, high-Z element formation, etc).

Compact stars are composed of matter in extreme conditions of density, temperature, and electromagnetic fields. Neutron stars have core densities, $\gtrsim 10^{15}$ g/cc, which could exceed nuclear density. Surface magnetic fields are thought to be $\sim 10^{12}$ gauss. When compact stars are in close binary systems with normal stars they become X-ray sources. X-ray observations of these binaries are an important new technique to study their properties. The high gravitational potential is responsible for their X-ray emission (see Section C). X-ray measurements can thus be related to the masses and radii of these objects. The neutron star is the only present laboratory in which matter in superstrong magnetic fields can be examined.

Black holes are general relativistic objects. They are physical examples of the mathematical singularity in relativity theory which results when an object collapses through its gravitional radius. The black holes' very existence is an important question in gravitational theory. X-rays may be the only means of detecting this object.

Hercules X-1 is thought to be a neutron star in a binary system. X-rays from Her X-1 can provide information about the binary system as well as the neutron star. Mass exchange between members of the binary system can create new regions of physical interest--Roche lobes, accretion disks, etc. Spectral variability occurs in Her X-1 because of geometrical reasons (partial and total eclipses, line of sight changes) as well as changing physical conditions (varying mass transfer rates, temperatures). The CXS as discussed above is well suited to these observations. The following introductory sections will discuss in more detail X-ray production mechanisms, binaries, and Her X-1.

## B. X-ray Production Mechanisms

The cosmos is a setting in which extremes of physical conditions exist. Temperatures, densities, and field strengths span tens of orders

of magnitude. X-rays are high energy photons produced in regions of space where conditions cause interactions of sufficient energy to take place. Continuum X-rays are formed when forces act upon distributions of charged particles. If the forces are caused by magnetic fields, photons, or electric fields, the production mechanisms are called respectively, synchrotron, inverse Compton, and bremsstrahlung. Since many excellent discussions of these mechanisms already appear in print (cf. Boldt 1969; Blumethal and Tucker 1974) the discussion presented below will be brief. Resonant processes can form X-ray lines whose energies and widths fix many of the parameters in their regions of origin. Finally absorption process, or "inverse production", will be discussed.

1. X-ray Continua

The X-ray spectrum which is observed from a source region can be written as (Boldt 1969)

$$\frac{dN}{dE}\left(\text{PHOTONS CM}^{-2}\,\text{SEC}^{-1}\,\text{SR}^{-1}\,\text{ERG}^{-1}\right) = \frac{1}{4\pi}\int_0^\infty q\,dr \qquad (1\text{-}1)$$

where r is the distance between the observer and the source and q, the photon source function is given as

$$q\left(\text{PHOTONS CM}^{-3}\,\text{SEC}^{-1}\,\text{ERG}^{-1}\right) = \frac{1}{E}\int \frac{d}{dE}\left(\frac{dW}{dt}\right)\frac{d}{dW}\left(\frac{d^3f}{dx^3}\right)dW \qquad (1\text{-}2)$$

where E is the radiated photon energy, W is the radiating particle energy, and f is the number of particles. In order to determine the output spectrum it is necessary to know in equation (1-2) the particle distribution and the form of the radiation loss mechanism. Because radiated power goes as acceleration squared, and acceleration is inversely proportional to mass for a given force, the electron is by far the strongest radiator. The Larmor formula for the total power radiated by an accelerated charge (cf. Jackson 1962) is given by

$$\frac{dW}{dt} = -\frac{2}{3}\frac{e^2}{c^3}a^2 \qquad (1\text{-}3)$$

where a is the acceleration. If the acceleration of a relativistic charge (Lorentz factor $\gamma$ ) in a magnetic field is substituted into equation (1-3) the result is

$$\frac{dW}{dt} = -2\gamma^2\sigma_T U_B c \qquad (1\text{-}4)$$

where $U_B$ is the magnetic field density and $\sigma_T = \frac{8}{3}\pi\left(\frac{e^2}{mc^2}\right)^2 = 6.7 \times 10^{-25}$ cm$^2$ is the Thomson scattering cross section. The spectrum of radiation emitted by a monoenergetic electron source can be approximated by a $\delta$-function at the peak energy of the emitted photons. This energy is given by (cf. Ginzburg and Syrovatskii 1974)

$$\langle E\rangle = 044\,\gamma^2\hbar\omega_c \qquad (1\text{-}5)$$

where the cyclotron energy $\hbar\omega_c = 9.30 \times 10^{-20}\ (U_B)^{1/2}$ ergs for randomly oriented magnetic field lines. If the electron number spectrum is a power law with index $\Gamma$ and normalization A then using equations (1-2), (1-4), and (1-5) the photon source function is

$$q_B = 198\times10^{-2} A U_B \left(499\times10^{-8} U_B^{\frac{1}{2}}\right)^{\Gamma-3/2} E^{-\frac{\Gamma+1}{2}} \qquad (1\text{-}6)$$

for synchrotron radiation. Similarly for inverse Compton radiation the magnetic field energy density is replaced by the electromagnetic energy density, U, in equation (1-4) and the average emitted photon energy is

$$\langle E\rangle = 4/3\ \gamma^2\langle h\nu\rangle$$

where $\langle h\nu\rangle$ is the average photon energy of the target photons. In this case,

$$q_{IC} = 1.98\times10^{-2} A U (1.99\times10^{12}\langle h\nu\rangle)^{\Gamma-3/2} E^{-\frac{1+1}{2}} \qquad (1\text{-}8)$$

There is evident similarity between the spectral forms in equations (1-6) and (1-8). In both synchrotron and inverse compton processes a power law input electron spectrum yields a power law photon spectrum.

The acceleration of charged particles in electric fields requires a slightly different analysis because macroscopic electric fields do not exist under steady state conditions with free charges. Instead fluctuating electric fields exist near charged particles within plasmas which have no net charge. In a plasma collisional energy losses dominate radiation losses by a factor of $\sim 10^4$ (cf. Boldt 1974). Also, non-relativistic electrons create X-rays in this case. This can be seen as follows (cf. Jackson 1962). The coulomb collision time is on the order of b/v, where b is the impact parameter and v is the electron velocity. If the electron de Broglie wavelength is used as the minimum b, the emitted photon energy via the uncertainty principle is on the order of the electron kinetic energy. Kilvolt electrons are considered non-relativistic.

Bremsstrahlung can be thermal or non-thermal depending on the electron source distribution. For a non-thermal power law electron source distribution the spectrum is given by

$$q_{NB} = 1.19\times10^{-19} f(\Gamma) A n_0 E^{-(\Gamma+\frac{1}{2})} \qquad (1\text{-}9)$$

where f( ) is of the order unity and $n_o$ is the proton plasma target density. For a Maxwellian distribution of electrons (cf. Holt 1974)

$$q_{TB} = 1.21\times10^{-19} g(T)(kT)^{-\frac{1}{2}} E^{-1} Z^2 n_e n_0 e^{-E/kT} \qquad (1\text{-}10)$$

where Z is the target atomic number, $n_e$ the electron density, T the plasma

REPRODUCIBILITY OF THE
ORIGINAL PAGE IS POOR

temperature, and g(T) is the free-free Gaunt factor (Karzas and Latter 1961). The Gaunt factor is the logarithmic term containing the ratio of maximum and minimum impact parameters.

2. Resonant Processes

X-ray lines can be superimposed upon the X-ray continua. These X-ray lines are produced during interactions involving atomic electrons with binding energies in the X-ray regime. The K-shell binding energy, $E_K \simeq Z^2$ (0.0136) keV, is in the X-ray range for atoms with atomic number $Z \geq 8$. However, the lines which are observable in practice by OSO-8 are limited by the following considerations. The windows in the CXS are opaque to X-rays with energies less than $\sim$ 2 keV. Cosmic elemental abundances are to zeroth order assumed to be equal to their solar system values (Cameron 1973 - see Table 1-2). Evidence suggests this is a good assumption (cf. Serlemitsos et al. 1976b). Because of their low abundance, elements with Z > 30 are not expected to contribute significant line fluxes. The line energies of elements in the relevant energy range are shown in Table 1-1.

Line emission can be produced by a number of different mechanisms. The three which are probably most important are thermal emission, charge exchange, and fluorescence. Each forms lines at the resonant energy but with widths and strengths characteristic of the emitting region and the mechanism.

Thermal X-ray line emission occurs in a high temperature ($T \sim 10^{6-8}$K) plasma at or near thermal equilibrium. Each atomic species reaches an ionization equilibrium determined by the temperature and density of the plasma. Lines are formed by the decay of excited electrons to more tightly bound states following either collisional excitation or capture

into an excited state. An early calculation of this total spectrum (which because of its complexity must be done numerically) is given by Tucker and Koren (1971). They also include the continuum contribution due to radiative recombinations and the two-photon decay of the metastable 2S states as well as that due to bremsstrahlung. The more recent work of Raymond, Smith and Cox (1975) includes Gaunt factor calculations of Mewe (1972), line emission contributions from dielectronic recombinations, and new calculations of ionization equilibrium. Both preceeding models refer to low density optically thin models. That is, the optical thickness of the emitting region is so small that little of the radiation is re-absorbed in the plasma. In thermal equilibrium the volume emissivity due to excitations of level n' of ion Z in the ground state n, by electron collisions is given by (Blumenthal and Tucker 1974)

$$\epsilon_L = 1.9 \times 10^{-16} T^{-\frac{1}{2}} \bar{\Omega} \left(\frac{\Delta E}{I_H}\right) e^{-\Delta E/kT} n_e n_z \qquad (1\text{-}11)$$

where T is the gas temperature, $\Delta E$ the line energy, $I_H$ the hydrogen ionization potential, and $\bar{\Omega}$ the effective collision strength (see Table 1-1).

Charge exchange between subrelativistic cosmic rays and the interstellar gas could lead to detectable X-ray line emission (Silk and Steigman 1969). Cosmic ray nuclei which are initially stripped of their atomic electrons will capture electrons from ambient material. If the electron is captured into an excited orbital, it will subsequently cascade down to the ground state, emitting a characteristic $K_\alpha$ X-ray in the final transition. An approximation for the charge exchange cross section is given by Schiff (1975), viz:

$$\sigma_{i,i-1}^{Z} = \frac{2^{18}}{5}\pi a_0^2 \frac{i^5}{n^3} Z\left(\frac{v}{v_0}\right)^8 \left[\left(\frac{v}{v_0}\right)^4 + 2\left(\frac{v}{v_0}\right)^2\left(Z^2 + \frac{i^2}{n^2}\right) + \left(Z^2 - \frac{i^2}{n^2}\right)^2\right]^{-5} \qquad (1\text{-}12)$$

where i and i-1 are respectively the initial and final cosmic ray ion charges, n is the principal quantum number of the orbital into which the electron is first captured, $a_o$ is the Bohr radius, $v_o$ the corresponding electron velocity, Z the atomic number of the medium, and v the ion velocity. Improvements and other calculations of this cross section can be found in Omidvar et al. (1976) and references cited therein. Applications of this theory to X-ray observations have been made in previous works (cf. Serlemitsos et al., 1973; Pravdo and Boldt, 1975). Charge exchange which leads to X-ray production is strongly peaked around particle velocities $\sim Z_c v_o$, where $Z_c$ is the cosmic ray atomic number. At velocities higher than this the nuclei remain fully stripped, while at lower velocities the K shell remains occupied. This fact leads to the distinguishing characteristic of lines formed via the charge exchange mechanism: if the cosmic ray velocities are isotropically distributed, the characteristic line energy will be doppler broadened by a significant amount. For iron nuclei this velocity is 0.19c which leads to a line width in excess of 2 keV. In contrast, thermal line widths are on the order of a few eV.

Fluorescence of atoms with binding energies in the kilovolot range can also yield X-ray line emission. This is accomplished by a high energy (higher than the relevant ionization energy) beam of photons or particles incident upon the target material. The volume emissivity for fluorescent lines of an element with density $n_z$ in a plasma is given by

$$\epsilon_f = (n_o v)\,\Delta E\,\sigma_i\,\omega(Z)\,n_Z \qquad (1\text{-}13)$$

REPRODUCIBILITY OF THE
ORIGINAL PAGE IS POOR



where $(n_o v)$ is the flux of projectiles, $\Delta E$ is the line energy, and $\sigma_i$ is the ionization cross section. The fluorescence yield, $\omega(Z)$, is the probability that an atom will redistribute its electrons to fill inner shell vacancies by emitting a characteristic photon. Table 1-2 shows the fluorescent yield and abundances of elements with X-ray lines. The ionization cross section $\sigma_i$ is the photoelectric cross section if the ionization is due to photons or the collisional cross section if it is due to particles.

The most prominant X-ray lines in the CXS energy range are those due to iron with energies near 7 keV. Satellite observatories with adequate resolution at this energy (the CXS has a resolution of 1.1 keV FWHM at 6.7 keV) and excellent photon statistics have recently identified source spectra as optically thin thermal plasmas with this line emission (cf. Becker et al., 1976a). The equivalent width of a line is the width in energy space of the corresponding continuum centered at the line energy, which contributes an energy flux equal to the energy flux in the line. By comparing equivalent widths predicted by models and those observed in the data, estimates can be made of elemental abundances in the emitting plasmas. Pravdo et al. (1976b) observed a narrow iron line in an optically thin thermal spectrum from the supernova remnant Cas A, at an intensity consistent with normal cosmic abundance of iron.

3. X-ray Absorption and Scattering.

X-ray spectra are modified by absorption and scattering processes. This can take place within the source itself if it is optically thick, within an intervening region, or both. Free-free absorption is the inverse process to bremsstrahlung. The absorption coefficient in a plasma in thermal equilibrium at temperature T is given by (Blumenthal and Tucker 1974)

$$K(E) = 0.2\, h^2 Z^2 g(T) n_e n_z E^{-2} T^{-3/2} \qquad (1\text{-}14)$$

The optical depth of an emitting region is $\tau = kR$ where R is the scale size of the region. As $\tau$ becomes greater than 1, the region becomes increasingly optically thick and an observer sees less deeply into the source. In the limiting case of infinite optical thickness only the surface layer is observed and the spectrum has the Planckian form

$$\frac{dN}{dE} = \frac{8\pi}{c^3 h^2} E^2 / \left[ e^{E/kT} - 1 \right] \qquad (1\text{-}15)$$

where T is the blackbody temperature. Intermediate optical thicknesses produce spectra in the range between the exponential optically thin spectrum (equation 1-10) and the blackbody spectrum (equation 1-15).

Compton interactions can also modify a source spectrum. The optical depth for Compton scattering is $\tau_c = n_e \sigma_T$ where $\sigma_T = 6.7 \times 10^{-25} \text{cm}^2$ is the Thomson cross section. The X-ray regime is non-relativistic Thomson scattering because photon energy and kT are $< M_e c^2$. Photons of energy E transfer an average energy equal to (Novikov and Thorne 1973)

$$\Delta E = \frac{E}{m_e c^2} \left( E - 4kT \right) \qquad (1\text{-}16)$$

in a gas of temperature T. The photons gain energy if $4\ kT > E$ and the spectrum is Comptonized (cf. Illarionov and Sunyaev 1972). If $t_c >> 1$ the photons reach equilibrium with the electron gas and emerge with the electrons' Boltzman energy distribution.

Compton scattering is energy dependent in a strong magnetic field. Lodenquai et al. (1974) have shown that the Thomson cross section is

modified under these conditions and becomes

$$\sigma_T \propto \sigma_0 \left(\frac{E}{E_H}\right)^2$$

Boldt et al. (1976 have suggested that this effect could lead to a high energy spectral cut-off of the form

$$I_{MC} = \left[\exp\left(-\tau_0\left[\frac{E_H}{E}+1\right]^{-2}\right) + \tau_0 \frac{E}{E_H} \exp\left(-\tau_0\left[\frac{E_H}{E}-1\right]^{-2}\right)\right] / \left(\tau_0 \frac{E_H}{E}+1\right) \qquad (1-17)$$

where $E_H$ is the electron cyclotron energy and $t_o$ is the optical depth to Compton scattering. The two terms correspond to the ordinary and extra-ordinary waves. Photons in a beam with increasing energy and $E \lesssim E_H$ are preferentially scattered out of the light of sight.

Photoelectric absorption can significantly modify X-ray spectra. It occurs within optically thick sources and in the interstellar medium between the source and the observor. (See Chapter II for a further discussion of the photoelectric effect in connection with the CXS proportional counters). The interstellar medium is opaque to photons with energies less than a few hundred eV. For example, for photon energy, E = 100 eV, and hydrogen density, $N_H$ = 1 $cm^{-3}$, unit photoelectric optical depth extends to < 10 pc, which is small in terms of the galactic diameter of 3 x $10^4$ pc. However, the photoelectric cross section is a steep function of energy, $\sigma_p \sim E^{-3}$. Above 2 keV the interstellar medium is essentially transparent. Absorption edges appear at ionization energies of the absorbing elements. Brown and Gould (1970) and Fireman (1974) have calculated the photoelectric absorption cross section for X-rays in material with normal cosmic abundances. Figure 1-2 shows the absorption cross section for iron as a function of incident photon energy. The absorption intrinsic to a source can be separated from that due to the interstellar

medium if an independent measure is known of the column density of matter in the line of sight to the source (cf. Ryter 1976).

This concludes the brief discussion of the fundamental physical processes relevant to cosmic X-rays. The following section deals with applications of these effects in close X-ray binary systems. Finally in the last introductory section specific features of the unique Hercules X-1 system are discussed.

## C. X-ray Binaries

Accretion of matter onto compact stars was recognized as a possible source for cosmic X-rays by early theorists (cf. Zel'dovich and Shakura 1969). The X-ray luminosity due to accretion on an object of mass M and radius R is given by

$$L_x = \epsilon GM\dot{M}/R \qquad (1\text{-}18)$$

where $\dot{M}$ is the mass accretion rate and $\epsilon \lesssim 1$ is the efficiency at which gravitational potential energy is converted to X-rays. For an isolated compact star in the interstellar medium Zel'dovich and Novikov (1971) give an estimate for the accretion rate, viz:

$$\dot{M} = \alpha R_g^2 c \rho_\infty \left(\frac{Mc^2}{kT_\infty}\right)^{3/2} \qquad (1\text{-}19)$$

where $\rho_\infty$ and $T_\infty$ are the density and temperature of the medium beyond $R_c$, the mass capture radius, $R_g = \frac{2GM}{c^2}$ is the gravitational radius, and $\alpha$ is a function of the adiabatic index of the order unity. The gas at the mass capture radius is ionized by the accretion X-rays so that $T_\infty \sim 10^{4\text{-}5}$K. For the extreme values of the parameters and with $M = M_\odot$ and $R = 10^6$ cm (typical neutron star values) the X-ray luminosity is about $10^{31}$ ergs/s which is orders of magnitude below the luminosities of the

weakest celestial X-ray sources. It is interesting to note that this accretion rate and luminosity is calculated with the assumption that the accreting matter forms a hydrodynamic fluid. For an interstellar medium of non-interacting particles the accretion rate is lower by a factor of $\sim 10^9$. In binary systems, however, the ambient mass density, accretion rate, and X-ray luminosity can be greatly increased.

Mass accretion in close binaries was introduced as a possible source for X-ray emission by Hayakawa and Matsuoka (1964). If one member of the binary system is a neutron star or black hole, it is necessary that the system remained bound following the supernova explosion which lead to the formation of the collapsed object. The star which is originally more massive evolves faster. As its radius increases it will eventually exceed the critical Roche lobe radius and matter will be transferred onto the smaller companion. If the supernova occurs when the companion star has more mass, then the system is less likely to be disrupted due to loss of gravitational binding energy (cf. Tananbaum and Tucker 1974). The force of the supernova explosion itself could also disrupt the system (Sofia 1967). Recent results of McKee, Lecar, and Wheeler (1976) show that neutron stars formed in supernova explosions can remain bound in binary systems. However their orbits must have finite eccentricity. The observations of nearly circular orbits in the X-ray binaries Her X-1 and Cen X-3 can be explained in terms of tidal forces which circularize orbits.

Binaries become X-ray sources when the mass transfer reverses, and matter flows from the star which was originally less massive onto the evolved star--a neutron star or black hole. The evolved star could also be a white dwarf. There is no chance of disrupting the binary system in this case since the white dwarf is the endpoint of non-catastrophic

(i.e. no supernova explosion) stellar evolution. There are several possible mechanisms by which matter from the normal star (secondary) is deposited onto the compact star (primary). The three major mechanisms are normal stellar wind, Roche lobe overflow, and X-ray induced stellar wind. Mass ejection rates in stars via stellar wind are dependent upon the star's spectral type. The solar wind corresponds to $\dot{M} \sim 10^{-14} M_\odot/yr$ while stellar winds driven by radiation pressure in OB supergiants are deduced to yield $\dot{M} \sim 10^{-6}$ to $10^{-8}$ $M_\odot/yr$. (cf. Kraft 1975 and references cited therein). This latter mass loss rate is sufficient to explain the most luminous X-ray sources as can be seen by substituting the value for $\dot{M}$ into equation (1-18). The normal star in the Cen X-3 system has been identified as a BO supergiant (Krzeminsky 1973) which suggests the stellar wind accretion mechanism (cf. Davidson and Ostriker 1973).

The Roche surfaces are surfaces of equipotential in the gravitational field. Stable Roche lobes exist in binary systems in which stars co-rotate. The critical Roche surface is the one at which the gravitational attractions from the two stars are equal and opposite. Matter crossing this surface is free to move from one star to the other. For stars in circular orbit the critical Roche surface forms a figure eight pattern consisting of two lobes which encircle the stars. After the initial supernova explosion the secondary continues to evolve. When it expands to fill its Roche lobe, matter will be transferred through the inner Lagrangian point onto the compact object. If $M_1$ is the primary mass, $M_2$ the secondary mass, and $R_s$ the separation between the stars, the radius of the critical Roche surface is given approximately by (Tananbaum and Tucker 1974)

$$R_c = [0.38 + 0.2 \log M_2/M_1] R_s \qquad (1\text{-}20)$$

If the stars do not co-rotate, larger tidal lobes (Davidson and Ostriker

1973) may be relevant for mass transfer.

A coupling can exist between the X-ray emission from the primary and the secondary mass loss. The X-rays which originate from the accreted matter heat the secondary driving off more matter. This model along with Roche lobe overflow has been suggested by Basko and Sunyaev (1973).

For the case of Roche lobe overflow an additional complication is added to the accretion process. Matter from the secondary must first dissipate the system angular momentum which it carries before it can be accreted. A viscous accretion disk serves to do this. As material drifts inward from the outer to the inner disk radius it loses angular momentum until it can infall radially. Prendergast and Burbidge (1968) discuss this process for white dwarfs and Pringle and Rees (1973) do so for neutron stars and black holes. Magnetic fields effect the location of the inner disk radius. At the Alfven radius, $R_A$, the magnetic field energy density just equals the kinetic energy density of the infalling matter and the disk is unstable at smaller radii. It can be approximated in (cf. Lamb 1974)

$$\frac{B^2(R_A)}{8\pi} \simeq \rho V^2(R_A) \qquad (1\text{-}21)$$

where B is the magnetic field strength, $\rho$ is the mass density, and V is its radial velocity. Within this radius matter which is hot and therefore ionized will follow the field lines inward. For a black hole the accretion disk is the source of X-rays while for a neutron star most of the emission arises from material falling onto the stellar surface after leaving the inner portions of the disk.

The magnetic field in a neutron star is approximately a dipole (cf. Zel'dovitch and Novikov 1971). Within the Alfven radius accreting

matter is tied to the field lines and will flow onto the magnetic poles creating an X-ray "hot spot" on the stellar surface. The shape and dimensions of a typical hot spot are given by Basko and Sunyaev (1974) as an accretion funnel with radius $\sim 0.1R$ and wall thickness $\sim 5 \times 10^3$ cm, with R the neutron star radius. If the magnetic dipole axis is not aligned with the rotation axis and if the magnetic axis passes an observer's line of sight, he will see periodic X-ray pulses as the hot spot on the pole sweeps by. An approximately constant X-ray background in addition to the pulse can originate from reflected pulse X-rays from the accretion disk, or from the rest of the stellar surface (Davidson 1973). The shape and duty cycle of the pulse are not determined by the size of the hot spot which radiates isotropically. Rather the pulse profile is probably determined by scattering processes in the accreting atmosphere after the X-rays are emitted from the surface. In one model (Lamb et al. 1973) the optical depth to electron scattering across the accretion column is much less than that along the flow so that photons escape preferentially in directions parallel to the surface forming a "fan" beam. Alternatively, a "pencil" beam will be produced in a strong magnetic field because the scattering cross section, $\sigma_\tau \sim \sigma_o \sin^2\theta$, where $\theta$ is the angle between the photon propagation direction and the magnetic field lines (cf. Basko and Sunyaev 1974 and references cited therein) and $\sigma_o$ is the zero field cross section. In this model only photons with small $\theta$ will escape unscattered from the pole leading to a pulse with small angular extent.

Matter accreting from a disk can transfer angular momentum to the neutron star. The star will spin-up or down depending upon whether the sense of its rotation is parallel or anti-parallel to the disk rotation.

An estimate for the magnitude of the spin-up case is given in Pringle and Rees (1972), viz:

$$\frac{P}{\dot{P}} = -1.4\times10^{5}\left(\frac{10^{17}}{\dot{M}}\right)\left(\frac{M}{M_{\odot}}\right)^{\frac{1}{2}}\left(\frac{R_A}{10^{6}}\right)^{-\frac{1}{2}}\left(\frac{R}{10^{6}}\right)^{2} \text{ yr.} \qquad (1\text{-}22)$$

where P is the period, $R_A$ the Alfven radius, and R the star radius as before.

The luminosity of an X-ray source is limited by a general principle which applies to any stellar radiation. Radiation from the star exerts pressure on material near the surface. This radiation pressure will drive off the atmospheric layers if it exceeds the gravitational binding energy. Compton scattering is the most effective photon-to-electron energy transfer mechanism. The so-called Eddington limiting luminosity can be expressed as (cf. Maraschi et al. 1974)

$$L_E = 4\pi G M \mu_e m_p c/\sigma_T \simeq 1.2\times10^{38}\,\mu_e\left(\frac{M}{M_{\odot}}\right) \text{ erg/s} \qquad (1\text{-}23)$$

where $\mu_e$ is the atomic weight per electron. Although the photons transfer most of their energy to electrons ($\sigma_T \sim M^{-2}$), the ions are tied to the electrons by Coulomb forces. It is evident that radiation pressure is an important force in high luminosity accreting X-ray binaries. If these sources have masses on the order $M_{\odot}$, as is believed, then their luminosities are close to $L_E$. Recent works have shown that if accreting matter temperatures reach values $\gtrsim 10^{9}$K, $L_E$ can be exceeded by neutrino fluxes (Ruffini and Wilson 1974). Basko and Sunyaev (1976) point out that the actual limiting luminosity is dependent on the accretion geometry and given by

$$L^{**} = \frac{a_0}{\pi d_0} L_E \qquad (1\text{-}24)$$

where the accretion funnel thickness $d_0$ can be much smaller than its radius $a_0$.

Many X-ray sources are believed to be members of stellar binary systems. However a large diversity exists in their observable behavior. Three such sources were viewed during a single Goddard rocket flight in 1973. Her X-1 exhibited regular 1.2 second pulsations indicating perhaps that it is a neutron star. Cyg X-3 showed a white noise temporal profile . This source is known to have a 4.8 hour intensity modulated cycle. The X-ray source and cycle are still not well understood. During a later rocket flight iron line emission was seen from this source (Serlemitsos et al. 1975). Finally Cyg X-1 showed intense X-ray bursts with millisecond temporal structure (cf. Rothschild et al. 1974). Independent measurements of the mass of Cyg X-1 suggest that it is more massive than the theoretical upper limit for a neutron star mass. For these reasons Cyg X-1 is the most likely candidate for a black hole. There are even observational differences between similar sources such as Cen X-3 and Her X-1, which are the only known fast X-ray pulsars. Specific models have to be adapted to the observable peculiarities of each object.

Hercules X-1 is a binary X-ray source which exhibits many periodicities. Its spectral properties can be correlated with system periodicities to varying extents. The next section discusses the properties and models of Her X-1.

## D. Hercules X-1

The Hercules X-1/HZ Herculis binary system exhibits periodicities on several time scales. Some of these periodicities are well understood

while for others, there are no universally accepted explanations. Figure 1-3 shows a schematic representation of these periods. Each will be discussed below along with some of the suggested interpretations. Knowledge of the source spectra prior to this work will also be presented.

1) 1.7 day period.

This period is understood to be the binary period of revolution (see Figure 1-3a). Regular eclipses are observed at this period lasting for 0.24 day (Tananbaum et al. 1972). Giacconi et al. (1973) report transitions to and from eclipse occurring in less than 700 seconds implying an X-ray emitting region size $\lesssim 10^{10}$cm. The optical companion, HZ Herculis, was confirmed when Bahcall and Bahcall (1972) and Liller (1972) discovered in it 1.7 day optical variations in phase with the X-ray period. Keplers third law gives for the binary star separation

$$R_s = 3.5 \times 10^{11} \left(\frac{M_1 + M_2}{M_\odot}\right)^{\frac{1}{3}} \left(\frac{P}{1\ \text{day}}\right)^{2/3} \text{cm.} \qquad (1\text{-}25)$$

Sinusoidal Doppler shifts of the 1.2 sec pulse period confirm the binary interpretation. They indicate that the orbit is nearly circular with a maximum orbital speed of (170 sin i) km $\text{sec}^{-1}$, where i is the inclination angle between the normal to the orbit and the line of sight. With this information equation (1-25) can be expressed as the mass function (cf. Boynton 1975)

$$\frac{M_2^3 \sin^3 i}{(M_1 + M_2)^2} = f\left(P, V_{\text{HER X-1}} \sin i\right) = 0.85\, M_\odot \qquad (1\text{-}26)$$

with $M_1 = M_{\text{Her X-1}}$. Because the X-ray source is dramatically eclipsed i is believed to be close to 90°. From optical data Bahcall and Bahcall

(1972) have estimated $i \geq 85°$. The duration of the eclipse defines a radius of occultation $R_o$ in the expression

$$(R_o/R_s)^2 = \cos^2 i + \sin^2 \frac{b}{2} \sin^2 i \qquad (1\text{-}27)$$

where b is the angular extent of the eclipse, b = 0.89. For $i = 90°$, $(R_o/R_s) = 0.43$. If HZ Her transfers mass via Roche lobe overflow then it is possible that $R_o \sim R_c$ as defined in equation (1-20). Using equations (1-26) and (1-20) we obtain $M_1 \sim 1\ M_o$ and $M_2 \sim 2\ M_o$. Because X-rays from Her X-1 substantially heat the facing side of HZ Her, it is difficult to determine its spectral type. However, mass estimates on the basis of spectral type yield similar results. (Crampton and Hutchings 1972). If HZ Her is a main sequence star in the spectral range A to F (cf. Forman et al. 1972) then it is reasonable to assume that the mass transfer mechanism is Roche lobe overflow rather than a strong stellar wind which would be present from a supergiant.

The photoelectric U band flux from HZ Her changes by a factor of $\sim$ 12 over the 1.7 day period (Boynton 1975). This large effect is probably due to X-ray heating of the visible side of the star by Her X-1. Basko and Sunyaev (1973) suggest that this heating can induce a stellar wind which supplies enough mass to Her X-1 to maintain its X-ray luminosity. Even in the case of Roche lobe overflow the X-ray heating initially has an important positive feedback effect. Eventually as the gas outflow increases it will absorb the X-rays and thus regulate the mechanism. Alme and Wilson (1974) and McCray and Hatchett (1975) found the induced mass transfer rate to be too small to produce the X-ray luminosity. In the latter calculation although the mass loss rate is marginally sufficient, the mass capture rate (i.e. capture by Her X-1 of the outflow)

REPRODUCIBILITY OF THE
ORIGINAL PAGE IS POOR



is substantially less. A recent calculation of this mechanism which includes the effect of the large soft X-ray flux from Her X-1 suggests that the induced stellar wind, much of whose mass is lost by the system, while not of primary importance as a source, can regulate Roche lobe overflow which otherwise would runaway. Finally, these authors have jointly decided (Basko, Hatchett, McCray, and Sunyaev 1976) that the soft X-ray flux can induce a subsonic mass flow through the inner Lagrangian point, which is sufficient to explain the X-ray luminosity.

2) 1.2 Second Pulsation.

The existence of regular 1.2 second (the period has been determined to seven decimal places) pulsations limits the models for Her X-1. Figure 1-3b depicts this effect. There is no known mechanism for an accreting black hole to produce stable pulsations. Either a rotating magnetic neutron star or the non-radial pulsations of a white dwarf (DeGregoria and Woltjer 1973) could be responsible. However a white dwarf may not be able to pulsate so quickly (Ostriker 1971) or with such stability (Salpeter 1973). For a review of arguments for and against the white dwarf model see Kraft (1975). Generally the neutron star model has gained acceptance because of its compatibility with other system properties (i.e. the $\sim$ 35 day period--see below). The lower limit for a neutron star rotation period is well below 1.2 seconds (cf. Tananbaum and Tucker 1974).

In addition to sinusoidal Doppler variations in the pulse period due to the binary orbit, Giacconi _et al._ (1973) reported a long term period decrease of 4.5 μs over seven months. This spin-up is explained by the angular momentum transferred to the neutron star by matter infalling from the accretion disk (Pringle and Rees 1972). Later observations

(Giacconi 1974) show that this trend continues and that the decrease is not monotonic. In fact short term period increases are observed. Brecher and Wasserman (1974) have suggested that these variations may be due to Doppler shifts caused by an as-of-yet undiscovered third member of the system. Lamb, Pines, and Shaham (1976) conclude that either excitations of the long period Tkachenko modes of the rotating neutron superfluid or short time-scale fluctuations in the accretion torques could explain the observed spin-up. The former mechanism produces a periodic variation superimposed on a general period decrease, while the latter produces non-periodic variations.

The shape of the Her X-1 X-ray pulse has been well studied. Giacconi et al. (1973) observed variability in the pulse shape on the time scale of an hour. The main pulse was double peaked. When the dip between the double peaks disappeared an interpulse appeared. The double peak structure and following minimum is also seen by Doxsey et al. (1973). About 40 per cent of the source counts fall in the main pulse which has a duty cycle of 0.4. At higher energies the first peak is more intense. Holt et al. (1974) observed a pulse similar to that in the preceding reference. They also report that the peaks are narrower for energies $\gtrsim$ 12 keV and lag the low energy pulse by about 5 per cent of the pulse period. Doxsey et al. (1973) interpret the pulse shape as a fan beam of an oblique magnetised rotating neutron star inclined to the line of sight. Tsuruta (1974) and Basko and Sunyaev (1975) suggest a pencil beam with central absorption to explain the double peaked main pulse. The former model predicts pulse shape changes with energy similar to those observed. It also predicts significant linear and circular polarization in various regions of the pulse.

3) $\sim$ 35 Day Cycle.

The X-ray luminosity from Her X-1 exhibits a $\sim$ 35 day on-off cycle (see Figure 1-3c). The source is at high level for 11-12 days followed by a 24 day off state (Giacconi et al. 1973). This is the least precise of the Her X-1 periodicities and the least well understood. The $\sim$ 35 day cycle is only approximately periodic. Her X-1 exhibits a quick turn-on and rise to maximum intensity followed by a gradual decline into the off state. Turn-on times can not be precisely predicted but seem to occur only at certain orbital phases clustered around $\phi \sim .25$ and $\phi \sim .68$. The 1.7 day optical variations continue with a similar amplitude throughout the 35 days. There are optical properties however which depend on the 35 day phase. For example, a secondary minimum appears in the optical light curve before and during the X-ray on period (cf. Boynton 1975 and references cited therein).

Many precessionary models have been discussed to explain this effect. Free precession of the neutron star spin axis which removes the magnetic pole periodically from the field of view was suggested by Brecher (1972). The accretion disk itself could precess and periodically occult the X-ray source (Katz 1973). Further modifications of this last idea were made by Roberts (1974) in which the disk is tied to the precessing HZ Her, and by Petterson (1975) in which the disk is twisted as a result of HZ Her precession. In this last model the twisted disk cuts the line of sight more abruptly on one side than on the other in agreement with the quick onset and gradual decline. Also, during the X-ray on state the disk obscures enough of the normal star to explain the observed secondary optical minimum.

There is a final aspect of the Her X-1 behavior which is probably associated with the 35 day behavior. Intensity dips are observed during the non-eclipsed X-ray on state (Giacconi et al. 1973). These dips first appear at a late orbital phase contiguous to the eclipse. They move progressively backward in phase during each successive orbit. The period of the dips is 1.6 days (cf. Jones and Forman 1976) which corresponds to a beat frequency between the 35 day and 1.7 day periods (see Figure 1-3a). In addition extra dips sometimes occur soon after turn on at a phase inconsistent with the 1.6 day period. The dips are thought to be caused by absorption of the X-rays by a region of gas, perhaps an accretion wake. A low energy cutoff is observed in the dip spectrum suggesting this interpretation (cf. Tananbaum and Tucker 1974).

It has been observed that the X-ray off state of Her X-1 is better described as a "low" state. In fact at certain times the low state intensity approaches that of the maximum during the high state (Fabian et al. 1973, Cooke and Page 1975). Jones and Forman (1976) in a re-examination of UHURU data find off-state emission at about 10% of the on-state intensity. If zero phase for the 35 day cycle is defined at the maximum X-ray intensity, then they find that at $\phi_{35} \sim 0.45$ and $\phi_{35} \sim .6$ the low state emission reaches about 30% of the maximum. Also eclipses and dips are observed. These authors interpret the observations in terms of a model by Roberts (1974) in which the accretion disk is inclined to the orbital plane.

4) Spectrum

The Her X-1 spectrum has been measured by many observors. These measurements have either been "snapshot" pictures of Her X-1 taken during rocket flights or integrated spectra over long periods of time by satellites. Up to now it has not been possible to examine spectra

with good statistics, as functions of orbital and pulse phase. Schreier et al. (1972) and Clark et al. (1972) fit the 2-20 keV emission by a power law in photon number with spectral index $\sim 1$ or a thermal with $kT = 60 \pm 20$ keV. This is a very hard spectrum which is perhaps typical of this class of object--for example Vela X-1 Rothschild et al. (1976). Ulmer et al. found that the number index steepens by $\sim 2.5$ for energies greater than 25 keV. Holt et al. (1974) describe a spectrum with excellent statistics as being flat below $\sim 20$ keV (number index 1.0) with an abrupt cutoff in intensity at $\sim 24$ keV. This cutoff can be interpreted as energy dependent Thomson scattering in the intense magnetic field at the neutron star pole (Boldt et al. 1976).

Giacconi et al. (1973) observe a similar low energy high state spectrum. During dips and turn on they see a substantial low energy cutoff suggesting absorption. The low state spectrum is found to be similar in shape but at a lower level than the spectrum during the high state (Jones and Forman 1976). The dip spectra during high and low states are comparable in the same way.

Hard X-ray observations ( $\gtrsim 20$ keV) in balloon flights have confirmed the spectral trend mentioned above. Kurfess and Crosa (1973), Sharma et al. 1973, and Manchanda et al. 1973 all report that the Her X-1 spectrum steepends at higher energies. Sharma et al. (1973) also report the absence of hard X-rays during the low state which implies that the same physical region is responsible for their emission. The pulsed fraction at these energies may be considerably lower than in the 2-20 keV range (Iyengar et al. 1974).

A soft X-ray flux has been discovered from Her X-1 with a luminosity comparable to and perhaps larger than the $> 2$ keV emission (Schulman

et al. 1975, Catura and Acton 1975). Fritz et al. (1976) have found that this soft flux is also modulated in the ∿ 35 day cycle.

5) Concluding Introductory Remarks.

Much of the progress in X-ray astronomy to date has resulted from temporal studies. In particular, periodic behavior can reveal many source properties. However, the understanding of many other source properties is dependent on spectroscopy. The spectrum of continuum X-rays indicates the production mechanism--blackbody emission, optically thin thermal emission, non-thermal processes, etc. Spectral features--lines, edges--also indicate source parameters such as temperatures, optical thickness, and elemental abundance. For the particular case of X-ray binaries, a combined spectral and temporal analysis is most useful. Her X-1 exhibits diverse temporal behavior, but no systematic examination of spectral correlations has yet been made. Spectral variability can reveal specific properties of the source regions responsible for the observed periodicities.

This work will present results (Chapter IV) of spectral observations of Her X-1. Most of the data were obtained with an argon detector in the energy range 2-20 keV. Much of this was received with 20 msec temporal resolution. This is an important aspect of the data because it allows examination of spectra as a function of the 1.2 second pulse phase. With this temporal resolution, data can be separated into 62 independent spectra each of which contains part of the substructure of the pulse. If these spectra are found to vary, it may be possible to discover information regarding the pulse formation and the geometry of the emitting region.

Her X-1 was observed continuously for 5 days or ∿ 3 complete binary periods. Spectra can thus be compared as a function of binary phase.

If part of the X-ray emission is reflected by HZ Her it would be expected to have an angular (binary phase) dependence which could be observed with this data.

Other data were obtained with a Xenon detector (2-60 keV) before, during, and immediately after an X-ray turn-on. The extended energy range of this detector allows examination of the previously observed high energy spectral change. Spectra during turn-on may indicate the ionization state of a possible occulting region. These results will be discussed (Chapter V) with the goal of discovering more clues to the nature of this source.

# CHAPTER II

## THE EXPERIMENT

### A. General Description

Orbiting Solar Observatory 8 (OSO-8) orbits the earth every ∿ 95 min in a nearly circular orbit of altitude ∿ 550 Km. It is a spin stabilized spacecraft with a despun "sail" section and a spinning "wheel" section (see Fig. 1-1). In overall dimension the rectangular sail is 218 cm by 246 cm, and the cylindrical wheel has radius 71 cm and height 53 cm. The spacecraft weights ∿ 1000 Kg.

The Goddard Space Flight Center Cosmic X-ray Spectroscopy experiment (CXS) consists of three X-ray detectors. It weighs ∿ 50 Kg. It is mounted on the wheel section of the satellite. Three views of the experimental package are shown in Figures 2-1,2,3. The detectors have small angular fields of view and are in or near alignment with the spacecraft spin axis. For this reason, the CXS is a "pointing" experiment--i.e. X-ray sources in the field of view are continuously observed for a fixed spin axis position. This is in contrast to an UHURU-like experiment which performs a slow scan along a great circle in the celestial sphere.

The CXS is designed to measure the X-ray spectra of celestial sources. The detectors are gas proportional counters. They cover a broad energy range (2-60 keV) with an energy resolution close to the theoretical limiting value for the resolution of proportional counters (see Section C). X-ray photons (counts) are recorded by the detectors and analyzed simultaneously in two different ways. One output is the total number of counts received during an integration period--normally 160 msec. This is called "rates" data. The second output is called "histogram" data. Each count is converted to an electrical signal by the detector,

and by a process known as pulse-height analysis, distributed among 64 pulseheight channels, each of which corresponds to a definite photon energy range. The counts are referred to as pulse-height-analyzed (PHA) counts, and their distribution is a histogram which can be related to the incident X-ray energy spectrum. The finest temporal resolution normally available for analysis of PHA counts is 20 msec.

The CXS is a unique experiment because it combines and extends the capabilities of other X-ray observatories. Its energy range (2-60 keV) is larger than that of UHURU (2-10 keV) with better resolution. Spectra can be obtained from weak sources near the UHURU detectability limit because the detectors are pointing and therefore have large duty cycles (percentage time on source). Experiments onboard the contempory satellites Ariel 5 and SAS C concentrate on spectral and temporal analysis respectively. The CXS does both. This is important because the flux from some X-ray sources is variable on short time scales ($\lesssim$ 1 sec). The exclusive capability of the CXS is to measure spectral-temporal correlations for these sources. The resulting disadvantage of a pointing experiment is that a limited area of the sky can be studied at a given time. Over the experiment lifetime of 1-3 years, however, most of the interesting celestial sources will be observed at least once.

The following section (B) is a short description of the CXS detectors. Section C discusses the physical principles underlying the detector's operation. The next two sections describe in more detail the fields of view and the data system. The last section (F) is a brief discussion of how data acquired by the experiment is compiled by the spacecraft and transmitted to earth.

## B. The Detectors

Three X-ray detectors comprise the Cosmic X-ray Spectroscopy Experiment (CXS). They are multi-anode, multi-layer gas proportional counters. Two of these detectors (hereafter called A and B) each contain a single gas volume while the third (detector C) has a second independent gas volume of neon-propane. The active gas is xenon in counters A and C, and argon in counter B. Methane is used in all three as a quench gas (10% by pressure). The gases are maintained at a pressure of 1.1 atmospheres in sealed volumes. X-rays enter the detectors through windows of material of low atomic number, either beryllium or plastic (mylar). Table 2-1 summarizes the important characteristics of each counter.

The active gas volumes in each detector are subdivided by grounded wire boundary layers into grids of rectangular cells with central wire anodes. The anodes are connected in a logic system which records valid X-ray events and rejects invalid particle events. The basic principle of this efficient background rejection scheme is that X-rays will usually interact in one cell, while a charged particle will interact in more than one cell. If two or more cells or layers receive coincident signals, these events are not accepted as true X-rays. In addition the boundary cells adjacent to the detectors sides are used as anticoincidence layers. Compton electrons produced by low energy $\gamma$-rays are generated in the counter wall material and increase the background in these outer cells. Only the C or two-gas detector has a veto layer on the top of the active cell array. This is in the form of the neon-propane gas volume, which is transparent to X-rays with energy, $E > 2$ keV, but records the passage of charged particles. This logic arrangement is shown schematically in Figure 2-4.

The windows through which X-rays enter the A and B detectors are thin sheets of 0.005 cm (2-mil) beryllium foil. Half the area of the B detector window is covered with strips of 0.002 cm aluminum, and the other half is covered by an additional 0.003 cm of Be. These thicknesses are chosen so that the Al and Be widths measured in $gm/cm^2$ are equivalent. Therefore while the "X-ray side" (Be) and the "electron side" (Al) transmit X-rays differently, they transmit charged particles identically. The difference between valid events on both sides is due solely to X-rays. The C detector has two windows of 0.003 cm aluminized mylar. One separates the two gas volumes and the other seals in the outer volume. All three windows become opaque to X-rays with energies less than $\sim$2 keV. Figure 2-5 shows detector window transmission as a function of X-ray energy for the three detectors.

Each detector has an onboard calibration source. Detectors A and C feature small ionization chambers containing 1 nc. of $Am^{241}$ located beneath the active gas volumes. The characteristic X-rays of $Am^{241}$ decay (at 13.9, 17.8, and 59.6 keV) are accompanied by alpha particles which are detected in the chamber. Any X-ray event in coincidence with an event in the ionization chamber is routed through the logic to an independent calibration counter which is monitored continuously in the telemetry. The B detector calibration must be commanded into operation. It consists of a 10 $\mu$c. $Fe^{55}$ point source located on a motor-controlled rotating rod directly above the beryllium window on the X-ray side. An impulse command transmitted to the satellite causes the rod to rotate the $Fe^{55}$ into and out of the field of view of the detector. In order to guard against the possibility that the radioactive source becomes stuck in the detector field of view, a separate similarly mounted sleeve can be

rotated by another impulse command to cover the rod. In practice, the rod has been left in the "calibrate" position and the sleeve rotated off whenever a calibration is desired. These B detector calibration tests, which last about five minutes each are run periodically either during real time satellite passes (and thus recovered immediately) or during times which are later examined in the data tapes.

The experiment includes a radiation monitor to measure the ambient charged particle density. Large particle fluxes can degrade the detectors by generating methane polymers which are deposited on the anodes and interfere with their operation. The monitor automatically turns off the experiment high voltages whenever a critical charged particle flux is reached. It is basically a Geiger-Mueller tube and a ratemeter which converts the rate of particles per second into a d.c. level. The threshold has a high and a low setting. In normal operation thus far, the low level has been used. Whenever the preset threshold is crossed a SAA event flag is sent to the spacecraft Event Flag Processor. The acronym SAA is taken from the South Atlantic Anomaly which is a major magnetic area in the satellite orbit where high electron fluxes cause an SAA start flag to be sent by the monitor. This flag causes the detectors' high voltages to be shut off until the electron flux drops below the threshold. The monitor then sends a SAA stop flag to automatically turn the high voltage back on. The radiation monitor can be disabled if necessary and its job taken over by the Spacecraft Stored Command Processor (SCP) which performs the same function for other X-ray experiments. The monitor has its own independent power supply whose +12V input bus comes from the experiment low voltage converter.

Each of the three detectors has a high voltage power supply and

independent redundant supply in case of failure. The high voltages are used to maintain a positive potential on the anodes to multiply and collect electrons freed by X-ray interactions in the gas. The normal operating voltages are 2047V, 1773V, and 2097V for the A, B, and C detectors respectively. In addition the detectors have four lower and three higher voltage levels separated by 34V steps. These steps are included in order to compensate for those degradations in the counters, such as loss of active gas pressure, which affect the gain. These additional voltage levels have also been used to examine special features in source spectra by slightly changing the energy range observed by the individual detector. The D.C. high voltages are regulated to 0.2 percent.

A low voltage converter accepts a 28V input from the spacecraft power supply and converts it to the various voltages used by different parts of the experiment. A redundant low voltage converter is available. As a safety feature a temperature sensing network shuts down the converter if it gets too hot. The high voltage control selects which low voltage converter is used. This separate unit also is the centralized control to switch the high voltages on and off. Thermal shields of 0.0008 cm Kapton with an aluminum side facing out are used to protect the experiment from heat loss and exposure to direct sunlight.

A major safety feature of the detectors is the modular design of the entire system. Each counter layer can be shut off individually in case it becomes too noisy or starts arcing. Vertical and horizontal anticoincidences can be interrupted if necessary. A schematic of the experiment is shown in Figure 2-6. This concludes the general physical description of the experiment. Further details can be found in the Goddard Space Flight Center's Cosmic X-ray Spectroscopy Experiment Technical Manual.

C. The Photoelectric and Other Physical Effects

The basic physical principle underlying the operation of the gas proportional counter is the photoelectric effect. The interaction of X-rays with the atomic electrons of the gases can be described in terms of a quantum efficiency, $\mu$, which is a function of the energy of the X-ray and the atomic number of the gas. The quantum efficiency is a smooth decreasing function of energy except for sharp discontinuities at absorption edges corresponding to ionization energies of atomic electrons in shells with different principle quantum numbers. Figure 2-7 shows the quantum efficiency of xenon. In the 2-60 keV range of interest, experimental points and theory are well matched. The K edge occurs at 34.6 keV and the three L edges average out at $\sim$ 4.8 keV. Aside from these edges, $\mu$ can be approximated by the expression

$$\mu \alpha E^{-2.7}$$

where E is the photon energy. The K edge of argon occurs at 3.2 keV and is the only argon edge in the relevant energy range, 2-20 keV. Photons with energies greater than the K(L) edge in a gas, have energies sufficient to photoionize a gas atom by knocking out a K(L) electron. The electrons are ejected with kinetic energies equal to the difference between the photon energy and the ionization energy. They ionize surrounding gas atoms creating one electron-ion pair per $\sim$30 eV of kinetic energy.

The resolution of the counters is limited by the statistical nature of the number of ion pairs formed by an electron. The error in this number is Poisson and equal to $\sim (E/30)^{-1/2}$ where E is the electron energy in eV. Resolution can be measured with the calibration sources. For example, the monoenergetic decay line of $Fe^{55}$ at 5.89 keV has a resolution of $\sim$17 percent in the B detector. The theoretical lower limit to this

number based on Poisson statistics is ∿ 10% in the initial ionization. During the multiplication process this percentage almost doubles. The approach of the resolution to the limit attests to the purity of the gas. In argon and xenon free electrons attach to impurities to form negative ions which move too slowly to form other pairs or to be collected by the anodes. This effect disturbs the Poisson distribution and also lowers the resolution. In detector assembly great care is taken in cleaning the inner counter surfaces. They are baked at 80°C while being evacuated to allow the Al surfaces to outgas. Also a "getter" in the form of an evaporated film of calcium metal is placed inside. The effect of this resolution is to distribute a monoenergetic photon source of energy E according to the expression

$$\frac{\text{Probability}\ (E')}{\text{Photon at } E} = [2\pi\sigma^2(E)]^{-\frac{1}{2}} \exp\left[\frac{(E-E')^2}{2\sigma^2(E)}\right] \qquad (2\text{-}1)$$

where $E^1$ is the measured energy and $\sigma^2$ can be expanded in a power series, $\sigma^2(E) = A_1E+A_2E^2+\ldots$ The coefficients in this last expression are determined experimently, with $A_i = 0$ for $i > 2$.

The probability that an X-ray will interact in the gas depends upon the quantum efficiency and the thickness of gas traversed. The units of $\mu$ are $cm^2/g$ and the interaction probability $\varepsilon_g$ is given by

$$\varepsilon_g(E) = \int_0^{D_g} \exp\left[-\mu_g(E)\,x\right] \mu_g(E)\,dx = 1-\exp\left[\right.$$

where $D_g$ is the gas thickness in $g/cm^2$. Photons can also interact photo-electrically within the window material. Similar quantum efficiencies exist for Be and mylar. In this case the transmission probability is

relevant and is given by

$$\epsilon_w = \exp\left[-\mu_w(E)\, D_w\right] \qquad (2\text{-}3)$$

where $D_w$ is the window thickness and $\mu_w(E)$, the quantum efficiency, is again a function of energy.

The production of fluorescence radiation can affect the determination of the X-ray photon energy. Since the fluorescence yield of argon and xenon is only a few per cent, this is a small effect. However it is important for two reasons. First the statistical accuracy in many spectra is sufficiently great that effects of a few per cent are noticeable. Second, if the source spectrum is very hard (many more high energy than low energy counts), then a high per centage (much higher than a few per cent) of the low energy counts originated from high energy photons which lost energy via fluorescence escape.

This escape process occurs as follows. When inner shell electrons are ionized there is a probability that an outer shell electron will cascade down to fill the vacancy by emitting a characteristic X-ray, with energy equal to the difference between the shell binding energies. This resonant radiation will sometimes leave the cell in which the original photon interacted. The net energy recorded for the event will be less than the actual photon energy by this amount. The probability of resonant radiation escape is the product of three probabilities: 1) that a photon with energy E will create an inner shell vacancy, 2) that the ionized atom will redistribute its atomic electrons by emitting an X-ray rather than, for example, by the Auger effect; and 3) that this X-ray will escape the cell. This product is given by

REPRODUCIBILITY OF THE
ORIGINAL PAGE IS POOR



$$P = \frac{1}{4\pi N} \int_0^{r_{max}} \exp\left[-\kappa(E) r\right] \kappa(E) f_n g_{n\ell n'\ell'} \times \int \exp\left[-\kappa(E_c) r_c\right] \kappa(E_c) r_c^2 dr_c d\Omega_c dr \qquad (2\text{-}4)$$

where E is the initial photon energy, $f_n$ is the flourescent yield of shell n, $g_{n\ell n'\ell'}$ is the transition probability from orbital $n\ell$ to $n'\ell'$, and $E_c$ is the characteristic X-ray energy. The other quantities are: $r_{max} = Z/\cos\Theta_i$: where Z is the detecting gas thickness = $D_g/\rho$ ($\rho$ is the gas density) and $\Theta_i$ the polar angle between the Z axis and the initial photon direction; $r_c$ is the distance between the detector walls and the origin; $\kappa(E) = \mu(E)\rho$; $d\Omega c$ is the solid angle of the detector seen by the escaping X-ray; and the normalization N is the probability that the initial interaction will take place, given by

$$N = \int \exp\left[-\kappa(E) r\right] \kappa(E) r^2 dr d\Omega \qquad (2\text{-}5)$$

Escape of flourescent radiation can cause anticoincidence losses.

End effects play an important role in the detection process. Photoelectrons will sometimes be freed with sufficient energy to leave the interaction cell and be lost to the collection process. They could also cause anticoincidence losses by being detected in another cell. This effect can be parameterized by the range, R, of the photoelectron. In the energy regime of interest the electron range can be approximated by $R \sim E^2$ where E is the electron energy. Photoelectrons produce other free electrons by acting as ionizing particles within the gas. Subsequently, these random walk toward the high positive potentials maintained in the anodes by the high voltages. These electrons are often freed with $\sim$ eV kinetic energies. This random motion interferes with the

anode collection process. However, this motion is suppressed when the electrons transfer energy to the $\sim$ eV excited levels of the methane quench gas.

The number of free electrons undergoes a multiplication process and this multiplicative factor, or gain, is directly related to the value of the the high voltage. Far from the anodes, the free electrons have insufficient energy to ionize other atoms. This is because the electric field from the anodes is too weak at this distance. When the free electrons approach within about one anode diameter from the anode, they acquire sufficient energy from the field to ionize other atoms. The multiplication process predominately occurs close to the individual anodes.

The gain in the CXS detectors is between 2-4 x $10^3$. The linearity, slope, and intercept of the gain can be determined by calibration. In addition to the onboard calibration sources, there is a calibration facility at Goddard Space Flight Center consisting of a beam of high energy ( $\gtrsim$ 25 keV) electrons and metallic targets. The fluorescent X-rays from the metals with their well established energies are used to determine the gain parameters for each detector.

There are many sources which can contribute to internal and ambient inflight background by masquerading as valid X-ray events. Precipitating charge particles have been discussed in relation to the radiation monitor. $\gamma$-rays can interact in the counter material via Compton collisions and eject Compton electrons. In the Compton effect, the electron binding energies are so small compared to the photon energies that even before the collision the electrons are essentially "free". This scattering effect becomes dominant, however, for photon energies greater than those in the CXS range. Using the Thomson scattering cross section as the

strict upper limit to the Compton cross section, a simple calculation shows that the Compton interaction probability in the detector is very small. The Thompson cross section, $\sigma_T \sim 6.7 \times 10^{-25}$ cm$^2$, is several orders of magnitude less than the photoelectric cross section (see Figure 2-7) below 100 keV and is an insignificant effect even when the larger number of available scattering electrons is taken into account.

Fluorescence of counter material can produce spurious X-rays. During periods of high ambient charged particle density, an 8 keV fluorescence line from the copper collimator tubes is observed. This effect is similar to that obtained in the calibration facility when metal targets are bombarded with high energy electrons. However in particle-free regions of the satellite orbit this contamination is not observed. The possibility also exists that counter material may become radioactive by nuclear reactions caused by the intense particle fluxes in heavily contaminated regions like the South Atlantic Anomaly. This effect has not been seen. The C detector which is periodically occulted by shields mounted on the spacecraft sail which are opaque to X-rays, gives the best measure of internal background during the occulted times.

## D. Fields of View

The CXS fields of view are defined by the detectors themselves and by their orientations on OSO-8. Mechanical collimators are mounted above the exterior windows of each detector. These are closely packed arrays of BeCu circular tubes, with 0.008 cm wall thickness and 0.4686 cm ID. The length of these tubes defines a full-width-half-maximum (FWHM) angle for a circular field of view. In the B detector this angle is 3.34 degrees, and 5.09 degrees in detectors A and C. Figure 2-8 shows the counts per second in the B detector in a calibration test as a function of angle between look direction and X-ray beam direction. In order to

identify source intensity variations it is essential to know to high accuracy this angle of incidence so that detection efficiency changes can be taken into account. Star trackers onboard OSO-8 relay optical pictures of the celestial sphere back to earth. These pictures are interpreted using reference stars in the field of view to determine the spin axis direction (and thus the detectors' directions-see below) relative to the fixed stars. The accuracy of this determination is nominally within 0.1 degrees which introduces negligible error in CXS source intensity measurements.

The detectors' mounting on the satellite is depicted in Figure 2-9. OSO-8 is primarily a solar observatory. The solar experiments are located on the fixed sail portion of the spacecraft which remains pointed at the sun to within $\sim$ 3 degrees. The CXS is on the spinning wheel section and the detectors are in or near alignment with the satellite spin axis. Two detectors, B and C, are pointed respectively opposite and along the spin axis. The A detector is tilted 5 degrees off the negative spin axis so that it sweeps out a small cone in the sky with nodes at $\sim$ 0 degrees and at $\sim$ 10 degrees. Since the spin axis is perpendicular to the sail direction the CXS points generally in directions normal to the earth-sun line. As the sun moves across the sky at $\sim$ 1 degree per day, the CXS look direction does also, so that all directions on the celestial sphere are attainable annually, or semiannually with oppositely facing detectors.

A spin axis program is planned in a cooperative manner by the seven OSO-8 experiment teams. The individual needs of each experiment in satisfying its scientific objectives are taken into account in this program. Figure 2-10 shows the route of the spacecraft spin axis near the vicinity

of Hercules X-1. The observation of Her X-1 which will be discussed in a later section was performed during this time. Hercules X-1 is circled with a 5 degree circle in the Figure and the other known X-ray sources are identified in Table 2.2 by their code letters. Abell clusters and other potential sources are also shown.

A final aspect of the CXS field of view concerns the C detector and an objective of the experiment not directly related to this work. The C detector field of view is periodically occulted by tantalum shields opaque to X-rays. This is done, as mentioned before, to get a measure of internal detector background to use as background in observations of the diffuse cosmic X-ray emission. A two-gas detector with its increased efficiency in rejection of spurious events is admirably suited to this goal.

## E. Data System

The CXS data system assembles scientific and housekeeping information from the detectors. Figure 2-11,12 show a block diagram of this system. Housekeeping information includes detectors and electronics temperatures, high and low voltage values, threshold levels, and experiment mode settings. The scientific information obtained varies with the experiment operation mode. This section will deal with the scientific uses and capabilities of the data system rather than the hardware. The latter is located in a black aluminum box outside of and separable from the detector complement (Figures 2-1,2,3).

Telemetry from OSO-8 is organized in the following manner. A "minor frame" contains 128 data words. A "major frame" contains 128 minor frames. The temporal spacing between words, minor frames, and major frames is 1.25 msec, 160 msec, and 20.48 sec respectively. The

CXS is normally assigned 10 words per minor frame. The other words are used for other experiments and spacecraft operations. Three of the 10 data words are used for the three detector rates. These rates indicate source (or background) intensities in counts per 160 msec. This fine temporal resolution is necessary because X-ray sources are variable on similar time scales.

The other seven words per minor frame are used to compile histogram data. This is the spectral information as described in Section A. Every signal from a valid X-ray event is pulse-height-analyzed by an analogue-to-digital (A-D) converter and added to a storage buffer. The detectors' energy ranges are divided into 64 pulse height channels. For the B (argon) detector the channel energy varies linearly with photon energy. In the xenon detectors the channel energy range is approximately linear but the slope doubles at channel 32 and doubles again at channel 48. This A-D converter transfer function is illustrated in Figure 2-13.

In the normal "stored" mode of operation, 5 of the seven words transmit A histograms. The A detector describes 5 degree circles in the sky. Because the look direction changes, A histograms are accumulated for only one fourth wheel rotation and stored in four separate sectors. These sectors correspond to $\sim$ 2.5 sec each (exactly 2.5 sec for a wheel spin rate of 6 rpm) and many wheel rotations can be overlayed to obtain pulse height spectra for each of the four quarters of the A scan.

B and C data are transmitted by another histogram data word. These histograms are accumulated for 40.96 sec, or two major frames of the spacecraft telemetry, and then are dumped in subsequent alternating major frames. Since detector C points forward, its field of view is periodically occulted by the tantalum shields and the pointed instrument (solar

experiments) assembly. C data therefore is accumulated in two separate histograms. The one discussed above corresponds to counts received when the field of view is open. A separate "C occult" histogram consists of counts received when the detector is under the shield. The aft-facing B detector is always open.

The phase of the sectored A data and the C open-occult data is determined by the Master Index Pulse (MIP), a pulse received from the sun every satellite spin. The sector size is determined by experiment hardware. This method of A data sectoring is called spin synchronized sectoring.

There are three command registers in the experiment which consist of 16 bits each. These bits indicate and control many of the possible experiment states. They can be changed by commands from the ground. Each command register is associated generally with one detector, and controls such things as high voltage levels and layer interrupts. Also, several bits in some registers affect two or more detectors. There are two important examples. First, the "BC rate control" bits affect the B and C detectors rates words. There are four possible settings. In the normal setting B X-ray side (BX) (see Section B) and C rates are read out every 160 msec. The BC rate control bits can be changed to read out instead either BX or C rates twice per minor frame to obtain 80 msec resolution. Or, the two B detector rates, BX and B electron side (Be) can be read out. In short the four possibilities are BX-C, BX-BX, C-C, or BX-Be. These modes improve the resolution of one detector at the expense of losing data from the other.

The second example is the most important alternate data mode. It is called "real time" and affects the seven histogram data words.

In this mode all seven words are dedicated to one detector. No histogram data comes from the other two. However the PHA counts coming from the real time detector (i.e., that detector commanded into the real time mode) are individually timed with a temporal resolution of 20 msec. This is a vast improvement over the PHA temporal resolution in the stored mode of $\sim$ 10 to 40.96 sec. This mode sacrifices histogram data from two detectors to obtain better temporal resolution with the third. The ideal opportunity to use real time occurs when a source of moderate strength (If more than one count from a strong source is received within 20 msec, all counts except the last, which is pulse-height-analyzed, are lost. This is known as a dead-time effect and can be corrected for when necessary using Poisson statistics.) is in the field of view of one detector, while the other detectors' fields of view are empty.

In addition to the data read out every minor frame, other data is sent with major frame periodicity. Fifty one words in each major frame contain C occult histograms, calibrate histograms, radiation monitor rates, commutated rates, and experiment status data. The commutated rates are 31 different detector rates (for example, B detector vertical anticoincidence rate) which are sequentially sampled in a $\sim$ 10 min cycle.

Other experiment mode settings and data system features are present. They will not be discussed here since they are not relevant to this particular work. The following chapters describe how the experiment capabilities were employed and the results thereof.

## F. Data Transmission

Data transmitted by OSO-8 is received by the NASA communications network, centered at Goddard Space Flight Center. Tape recorders on the spacecraft accumulate experiment data. They are periodically dumped

at high speed during ground station passes. The ground stations are located worldwide, with the closest being Rosmond, North Carolina. This station has a direct link to GSFC and provides preliminary "quick look" data whenever the tapes are dumped there (approximately 10% of the time).

There is an onboard spacecraft clock which is accurate to one part in $10^7$ (approximately 1 sec per year). It serves to temporally label each event to the nearest millisecond. The Her X-1 observation spanned $\sim$ 8 days which corresponds to an inaccuracy of less than 0.1 sec over the entire time. Universal time is measured as Greenwich mean time (Zulu).

Star trackers on OSO-8 are used to determine the direction towards which the spacecraft spin axis points. These positions are updated every major frame ( $\sim$ 20 s). For circular colimators the detection efficiency, $\varepsilon$, to a point source is given by

$$\varepsilon(\theta) = \frac{2}{\pi}\left[\cos^{-1}\frac{\theta}{\theta_{max}} - \sqrt{1-\left(\frac{\theta}{\theta_{max}}\right)^2}\ \frac{\theta}{\theta_{max}}\right] \qquad (2\text{-}6)$$

where $\theta_{max}$ = 5.09° for detectors A and C, $\theta_{max}$ = 3.34° for detector B, and $\theta$ is the angle between the source and detector pointing direction. The normal after-the-fact pointing accuracy is 0.1 degrees. This introduces a source intensity uncertainty of less than 5% for the A and C detectors if the source is within 2 degrees of the pointing direction. Similarly the uncertainty is less than 6% for a source within 1 degree of the B detector direction.

OSO-8 data tapes containing experiment, temporal, and pointing information are assembled by the Information Processing Division of GSFC. Chapter III discusses the analysis of these tapes.

# CHAPTER III

## OBSERVATIONS AND ANALYSIS

### A. Observations

Hercules X-1 was discovered in 1972 (Schreier et al. 1972). Its binary nature was recognized by the regular sinusoidal pattern in time of the value of the X-ray pulse period. This discovery prompted a search for an optical companion of Her X-1, and it (HZ Herculis) was found soon afterwards (Liller 1972). The celestial coordinates of the Her X-1/HZ Herculis system are known accurately by X-ray (Doxsey et al. 1973) and optical observations (Liller 1972). They are $\alpha(1950) = 254.0088 \pm 0.004$ and $\delta(1950) = 35.4175 \pm 0.0003$, so the uncertainities in the detection efficiency (see Chapter II, Section F) introduced by these measurements are negligible.

The aft spin axis of OSO-8 arrived in the Her X-1 vicinity on August 26, 1975. At this time the satellite spin axis was pointed toward $\alpha(1950) = 251\overset{\circ}{.}3$, $\delta(1950) = 30\overset{\circ}{.}8$. The xenon filled A detector thus scanned across Her X-1 once every satellite spin ($\sim$ 10s). An X-ray turn-on was expected near this time from extrapolations of the $\sim$ 35 day period. This detector observed Her X-1 before, during, and shortly after turn-on.

After turn-on a satellite gas manuever was performed to point the aft axis directly toward Her X-1. In order to satisfy the stringent pointing requirement of the Columbia polarimeter experiment also observing Her X-1, great care was taken to minimize drifting from this aspect. Thus, from the start of August 29 (day 241.03) until the middle of September 3 (day 246.5) the argon-filled B detector observed the source with near maximum efficiency.

During the $\sim$ 5 day B detector observation several experiment mode

changes were instituted. Until day 243.1 the experiment remained in the normal stored operational mode (see Chapter II), which yields 40.96 sec temporal resolution for spectral data. At this time three changes were made. The B real time mode was activated improving the temporal resolution to 20 msec for spectral data. Also the B detector high voltage power supply was lowered one step in order to extend the detectable energy range to higher energies. A similar gain shift had been performed several days earlier when no source was in the field of view, to obtain a "low gain" background. The final change was to set the BC ratemeter to BB so that rates from Her X-1 could be obtained every 80 msec. On day 244.8 the gain was restored to its normal value but the detector was left in the "real time mode. In summary, the argon detector observations included one binary orbit with 40.96 sec temporal resolution for spectral data and two binary orbits with 20 msec temporal resolution for spectral data. During one of the latter orbits the detector high voltage was lowered one step.

Her X-1 appears in the B detector with a counting rate of $\sim$ 7 times background. Therefore slight fluctuations in the intrinsic X-ray background of this region of space should not significantly affect spectral measurements. In general data from source free regions accumulated before and after acquisition of Her X-1 are used for background subtraction. The scanning A detector accumulated background spectra simultaneously with source spectra from off-source sectors. Possible source contamination from 3U1702+32 has been suggested by Becker et al. (1976b). This weak source is only about 2 degrees from Her X-1 and is expected to contribute $\sim$ 5% to the total intensity according to the previous reference. Background taken during eclipsed portions of the binary orbit is also

used to further eliminate any source contamination problems.

After the scientific data is received from the satellite, the spin axis solutions, as well as the spin rate, longitude, latitude and height of the spacecraft as functions of time, are merged onto the tapes. The data from each experiment is stripped out and sent to the respective experimentors approximately two months after the observations are made. The CXS data are then incorporated onto a data base which is accessible for analysis by the computer facilities at GSFC, including IBM 360/91, 360/75, 360/95, and a partly dedicated minicomputer, PDP 11/70. The OSO-8 data base is divided into two parts. One contains rates data and the other PHA (spectral) data.

Figure 3.1 displays one orbit rate plots for detectors A, B, and C. At each abscissa are plotted points corresponding to every 160 msec rate during one satellite spin. There are evident times at which the counting rates rise abruptly followed by a loss of data. These correspond to times of increased ambient electron contamination. An automatic program was developed to define areas of clean data. This is accomplished by noting that high channel (high energy) rates in Xenon detectors remain fairly low for both source and source-free clean regions. The A detector data usually contains at least one source-free sector in its scan. This data is used to set a threshold for high energy counts beyond which data is considered to be contaminated. Figure 3-1 demonstrates that in contaminated regions the entire A detector rate is increased including the base line. Data drop-outs occur when the electron contamination level triggers the radiation monitor to shut off the high voltages.

Periodically each detector will be pointed at the earth. With knowledge of the spin axis position and the satellite ephemeris, the

times of earth occultation can be determined for each detector. Automatic programs thus remove these contaminated and occulted periods. The following section describes the analytical methods employed with the remaining data.

## B. Methods of Analysis

Three categories of information can be obtained from the Her X-1 OSO-8 data: spatial, temporal, and spectral. The first is discussed briefly since we are unable to approach the accuracy of previous experiments in this area. Temporal analysis has yielded a new determination of the pulsar period. The bulk of the results deal with the analysis of spectral data which is discussed last.

### 1) Spatial analysis

Her X-1 appears as a point source in the CXS. The B detector with a 3.34° FWHM collimator can only make a rough a priori estimate of its position. The scanning A detector is the most efficient in locating a source. With the knowledge of the peak in the azimuthal rate distribution, sun position, and the fixed-angle offset of the detector from the satellite sun sensor it is possible to determine a line containing the source position. The intersection of many lines obtained from different spin axis positions defines the source position. Alternatively the shape of the azimuthal profile can indicate the polar as well as the azimuthal source angle. Any of these methods however, as stated before, can not approach the accuracy at which this position has already been determined.

### 2) Temporal analysis

Temporal analysis of the Her X-1 data has proceeded in the following way. Before the exact period is known and to search for unknown

periodicities a fast Fourier analysis is performed on the data (Cooley et al. 1967). When a period is determined the data stream is folded over that period.

As mentioned before, since Her X-1 is in a binary system, its pulse period is Doppler shifted by this motion. In order to determine a best value for this period making use of data spanning several binary periods, it is sufficient to correct photon arrival times for this effect. The effects of satellite and earth motion during the observation are small but included. This was done in Paper 1 making use of the values 1.7001656$\pm$.0000006 days for the binary period and 13.183$\pm$.006 light seconds for the orbital radius (Schreier 1975). The best period was identified as the one which yielded the maximum $\chi^2$ value. The zero phase time was left as a free parameter in the fitting procedure.

The chi-square ($\chi^2$) test mentioned above has become standard in the analysis of X-ray data, both temporal and spectral. In general, X-ray data is grouped into K bins. A model is constructed with P independent free parameters to predict an expected value for each bin. If the data in the $i^{th}$ bin is $D_i$ and the model predicts $M_i$, $\chi^2$ is defined

$$\chi^2 = \sum_{i=1}^{K} (D_i - M_i)^2 / (\delta D_i)^2 \qquad (3\text{-}1)$$

where $(\delta D_i)^2$ is the variance associated with the measurement $D_i$. The number of degrees of freedom in this test equals (K-P). A table of probability for values of $\chi^2$ versus number of degrees of freedom can be found in the Handbook of Chemistry and Physics (1963) and is reproduced in Table 3.1. Model fits to the data are acceptable if the $\chi^2$ value obtained is acceptable. If K $\gtrsim$ 30 the probability of $\chi^2$ distribution is nearly Gaussian and can be written

REPRODUCIBILITY OF THE
ORIGINAL PAGE IS POOR



$$P(\chi^2) \simeq \frac{1}{2\sqrt{2\pi}} \exp\left[-\frac{1}{2}\left(\sqrt{2\chi^2} - \sqrt{2(K-P)-1}\right)^2\right] \qquad (3\text{-}2)$$

The mean value of $\chi^2 \simeq (K - P)$ and the variance of the probability distribution $\sigma^2(\chi^2) \simeq 2\ (K - P)$.

In the context of temporal analysis the $\chi^2$ test can be used in several ways. If periodic pulsed data is hypothesized, a period, phase, and pulse shape can be used as free parameters and tested against the data in order to obtain a minimum acceptable $\chi^2$. Alternatively, the data can be tested against a model in which no periodicity exists, to observe deviations from randomness. If the actual value of $\chi^2$ exceeds the expected value by $n\sigma(\chi^2)$ then a positive effect has been observed to $n\sigma$ confidence. Conversely if no positive effect is observed an upper limit to the pulsed fraction in the data can be obtained. Boldt et al. (1970) have given an expression for the average deviation of $\chi^2$ from its expectation value where the test described above is performed and where the data contain a pulsed component. This deviation is given by

$$\Delta\chi^2 = \left(\frac{f}{1+f}\right)^2 \left(\frac{1-\beta}{\beta}\right) N_T \qquad (3\text{-}3)$$

where f is the pulsed fraction, $\beta$ is the pulse duty cycle, and $N_T$ is the total number of counts. The variance of this distribution whose expected value is $(K-P) + \Delta\chi^2$ is

$$\sigma_f^2 = 2(K-P) + 4\Delta\chi^2(1+\varepsilon) \qquad (3\text{-}4)$$

where $\varepsilon = \left(\frac{f}{1+f}\right)\left(\frac{1-2\beta}{\beta}\right)$. Deviations of $\chi^2$ from the modified expected value are interpreted using $\sigma_f^2$ to get n sigma pulsed fraction upper limits (see Pravdo et al (1976c) for a fuller discussion of this technique).

The $\chi^2$ test is discussed further below in connection with spectral analysis.

3) Spectral analysis

The response of an X-ray detector can be described in terms of a response matrix R(E,E′) which accepts an ensemble of X-rays of energy E and distributes them over the energies E′. If I(E) is the input spectrum and O(E) the output spectrum, they are related by the response matrix through the expression

$$O(E') = \int I(E)\, R(E,E')\, dE \qquad (3\text{-}5)$$

However, with knowledge of R(E,E') and O(E') there is no straightforward method of deriving I(E). This is because R(E,E') is a singular and thus non-invertible matrix. R(E,E') is calculated making use of the principles described in Chapter II, section B. In practice the integral in equation (3-5) is replaced by a sum over the 63 detector pulse height channels and energy steps which are fine at low energies and coarse at high energies where count rates and detection efficiency are low. The response matrix incorporates energy-dependent window transmission efficiencies (equation 2-3) gas quantum efficiencies (equation 2-2), resonance escape probabilities (equation 2-4), detector resolution (equation 2-1), and a correction to gas efficiencies due to electron escape path lengths (equation 2-7) (see Appendix A).

It is also necessary to know what energies correspond to each pulse height channel in the three detectors. These calibrations were carried out preflight by the electron beam facility at GSFC and on a continuing basis by the onboard calibration sources. Parameters specifying the offset, gain and resolution of each detector are continually updated.

The relevant parameters are then used to analyze a particular data sample. In general the detectors have been remarkably stable in flight with minimal gain and resolution changes. The knowledge of these parameters is especially important when gain level shifts are made.

Spectral analysis proceeds as follows. Models $I_M(E)$ are postulated with P free parameters. The discrete sum form of equation (3-5)

$$O_M(E') = \sum_E I_M(E)\, R(E,E') \qquad (3\text{-}6)$$

is then used to obtain a model output, $O_M(E')$. This is then $\chi^2$ tested against the actual data $O(E')$ which is similarly divided into discrete energy bins. As before

$$\chi^2 = \sum_{E'} \left[O_M(E') - O(E')\right]^2 / O(E') \qquad (3\text{-}7)$$

In this case $(\delta O(E'))^2 = O(E')$ because the counts in each bin are assumed to be Poisson distributed, in which case the variance equals the number of counts. If the probability of $\chi^2$ is less than 10% it is unlikely that this model describes the data. However if the model fit is acceptable it is now possible to place confidence limits on the values of the parameters. Let $\chi^2_{min}$ represent the minimum acceptable value of $\chi^2$ obtained with (by definition) the best fit parameters. By varying these parameters the value of $\chi^2$ must increase. The limits on the parameters are those for which $\chi^2$ increases to a limiting value defined by (Lampton et al. 1976)

$$\chi^2_{LIM} = \chi^2_{MIN} + \chi^2(P) \qquad (3\text{-}8)$$

where $\chi^2(P)$ is the $\chi^2$ distribution with P degrees of freedom. The n sigma limits on $\chi^2(P)$ also define n sigma limits on the parameters. Table 3.2 demonstrates the deviations in $\chi^2_{min}$ necessary to achieve n sigma confidence limits for different numbers of free parameters.

The standard models used in first-cut spectral analysis are those calculated in Chapter I, Section B. They include power laws (equations (1-6), (1-8), and (1-9)), thermal exponential forms (equation [1-10]), the Planckian form (equation [1-15]), and linear combinations of these. Also photoelectric absorption (Brown and Gould 1970) with iron included is added as a free parameter which serves as a low energy cutoff. Compton scattering in a strong magnetic field is a high energy cutoff (see equation 1-17). In addition a pure exponential model (i.e. no gaunt factor and no inverse power of energy) has been found to fit certain data (Swank et al. 1976, Pravdo et al. 1976a).

Models also incorporate possible line emission. These lines are added to the continuum models as Gaussian forms

$$I_L(E) = a_1 \exp\left[-a_2 (E-E_L)^2\right] \qquad (3\text{-}9)$$

where $E_L$ is the line energy in keV, $a_1$ is a normalization factor proportional to the line intensity, and the FWHM of the line measured in keV is $\simeq 1.67\ a_2^{-1/2}$.

This section will be concluded with some remarks on the process of estimating confidence limits on model parameters using the $\chi^2$ test. In theory, to determine the range of one parameter, it is necessary to hold it fixed while varying all other parameters until a (secondary) minimum of $\chi^2$ is attained. When the number of independent parameters is > 3 this process becomes very computer time consuming. Many complex

spectra have on the order of $\sim$ 10 such parameters. Fortunately many of these parameters (such as those describing emission lines) effect only limited energy ranges of the spectrum and are thus not so strongly coupled to continuum and other parameters. In this case even if all the parameters are not varied, reasonably accurate confidence limits on the others are still achieved.

# CHAPTER IV

## RESULTS

The CXS observed Hercules X-1 with two detectors, and in a number of different experiment modes. First, the coning xenon (A) detector was positioned to scan across Her X-1 shortly before, during, and shortly after the initiation of an X-ray high state in the ∿ 35 day precessional cycle. Figure 4-1 shows the rates record of this detector for the quarter of the scan containing Her X-1. This data is a direct representation of the background-subtracted X-ray intensity from the source. The typical fast onset of the high state is evident early in day 240 when the intensity jumps from near background level to the normal Her X-1 high state level. Spectral analysis of the data represented in this Figure, including the X-ray intensity dip late in day 240, is presented in Section IV. C.

After the time of the observation represented in Figure 4-1, the negative spacecraft spin axis was pointed directly towards Her X-1. The argon (B) detector then monitored the source continuously (except for times of particle contamination and earth occultation) for ∿ 3 binary orbital periods. The rates record of this observation is shown in Figure 4-2. Once again the vertical scale is the background-subtracted X-ray intensity. Regular eclipses during which the flux is close to the background level are evident. Intensity dips in early binary orbits in the Figure merge with the eclipses and increase their apparent duration. The dips on days 244 and 246 are progressively more distinct from the eclipses, demonstrating their "march backward" in binary phase.

The B detector was commanded into different modes for each of the three orbital periods. There is a large amount of spectral data from this observation. Spectra will be identified according to which

experimental mode they were acquired in. During the first orbital period the detector was in the normal "stored" mode of operation. This yields temporal resolution of 40.96 sec for spectral data (see Chapter II). These spectra are useful for examining spectral correlations with the 1.7 day binary phase, but are useless for examining correlations with the 1.24 sec pulse phase. The spectra are labelled by the letter, "S", denoting stored mode.

In order to examine spectral correlations with the 1.24 sec pulse phase, the detector was commanded into the "real time" mode. This yields 20 msec temporal resolution for spectral data (see Chapter II). The data from the second and third binary orbits was acquired in this mode and identified by the letter "R". During the second orbit the detector gain was lowered to extend the detectable energy range from 24 keV to 31 keV. "RL" will identify real time low gain spectra. The detector gain was restored to its normal value for the third orbit. These spectra are called "RN" for real time normal gain.

The data from all three orbits are used to study spectral changes with binary phase (Section IV. A). Data from the last two orbits are used to examine spectral correlations with pulse phase (Section IV. B). Results are organized by the particular Her X-1 periodicity upon which they comment (see Section I. D for further introduction to these periodicities). This organizational separation is difficult to make at times as will be seen.

## A. Binary Period

The data from the argon detector were divided into time intervals corresponding to 0.10 binary period. Spectra were compiled for these times to see if there was any correlation between high state spectra

and binary phase. Table 4-1 shows these divisions and spectra. The data during times not corresponding to named spectra in the Table contain eclipses and intensity dips and will be considered elsewhere. Each spectra contains all good data beginning at the phase for which it is named and ending 0.10 phase later. The times of spectra S7a and S7 with asteriks beside them were modified respectively because of a gas manuever and to avoid the beginning of a dip. There are twenty spectra with usually three representative spectra for each phase value.

The general nature of each spectrum is the same and similar to that reported in Holt et al. (1974). They are acceptably fit by a power law model with number index between 0.84 and 1.05 and absorption by a hydrogen column density $N_H$ of few x $10^{21}$ $cm^{-2}$. The model includes a high energy cutoff of the form in equation 1-17. In addition there exists considerable spectral activity in the energy region between 5.5 and 8.2 keV. In some cases, for example RL2 shown in Figure 4-3, a single narrow line feature centered at 6.3 keV acceptably fits the data with $\chi^2 = 12$ for 11 degrees of freedom. Without the line, $\chi^2 = 64$. In other cases, RN1 shown in Figure 4-4, there is a deficiency near 6 keV and statistically significant line features near 5.5 and 7.4 keV. Spectrum S1 has a significant enhancement near 2.8 keV. Many spectra have enhancements near 15 keV, but only a few of these are statistically significant. The effect of the high energy cutoff is not seen fully enough for detailed study in the argon observations but $\tau_o \sim 10$ (the region scattering optical depth) and $E_H \sim 110$ keV ($B\text{-}10^{13}$g) fit most data (see equation 1-17).

There does not seem to be any simple correlation between spectral features and binary phase. Within an individual binary cycle, the total line equivalent width remains approximately constant with phase, whether

one or two features appear. This equivalent width is between 200 and 400 eV in most cases, and in all cases error estimates are consistent with this range. There is no correlation between the number of line features and binary phase. Such a correlation does exist from cycle to cycle however. The S data seldom (S3 and S6) need a double feature for an acceptable fit. The RL data are always able to be fit by a single feature, while the RN data have a double feature in all spectra but one (RN5). These results are summarized in Table 4-2. All the models fit the data acceptably except for S6.

The total high state spectrum was compiled for the times during which the experiment was in the normal gain setting (S and RN). This spectrum was fit well by a model with a single broad line centered at 6.5 keV. Using Table 3-2 the following 3σ confidence limits (these will be the standard confidence limits used throughout) are placed on this total spectrum: The line equivalent width is $0.335^{+0.140}_{-0.111}$ keV, the line energy $6.5 \pm 0.4$ keV, the number index $0.91^{+0.03}_{-0.05}$, and the absorption by a hydrogen column density of $(3.0^{+1.3}_{-1.6}) \times 10^{21}$ atoms $cm^{-2}$. A similar model with a single narrow line will not fit this data. The FWHM of the acceptable broad line is $2.4 \pm 0.7$ keV.

Figure 4-5 displays the Her X-1 light curve in five energy bands, corresponding to high state (without eclipses or dips) times during the argon detector observations. Generally, within statistics, the curves track each other. In particular the "iron-band" curve 5.7 - 7.7 keV shows consistent behavior with the neighboring energy ranges, again demonstrating the absence of correlation between the strength of features in this band and the binary phase.

The X-ray eclipse is an important aspect of the binary period.

During eclipses the detector counting rate increased slightly over the average rate in background celestial regions adjacent to Her X-1. This increase corresponds to about one per cent of the Her X-1 high state intensity and six per cent of the background rate. Possible explanations for this increase include emission from 3U1706+32, X-rays from Her X-1 during eclipse, or less likely, a background fluctuation. Even if 3U1706+32 is the cause, this suggests negligible contamination in the Her X-1 spectra. Much of this emission is concentrated in the iron band.

An observed transition to eclipse occurs in 107 seconds (Figure 4-6). During this time the counting rate increases from eclipsed to normal high state level. This rise time implies an absorbing region which ranges from opaque to transparent over $3.7 \times 10^9$ cm. A small post-eclipse dip is seen in the Figure. There is no significant hardness change during egress. Eclipse occurs at a distance of $\sim 3.1 \times 10^{11}$ cm perpendicular to the line of sight from the center of the occulting object, while the transition occurs in about $10^{-2}$ of this distance. More will be said concerning the relation of eclipses to pulsations in the next section.

## B. Pulsations

The argon detector pointed at Her X-1 for $\sim$ 5 days with temporal rate resolution of at least 160 ms. A $\chi^2$ analysis, leaving as free parameters the zero phase orbital time and the pulse period, yielded 241.506 $\pm$0.002 day of 1975 for the zero phase ephemeris and 1.2378065$\pm$0.0000001 sec for the pulse period (Becker et al. 1976b). This last result demonstrates that the Her X-1 pulsar has continued to spin up. The earliest reported value of this period (Giacconi 1974) on Dec. 8, 1971 is 1.2378200$\pm$ .0000002. Combined with the OSO-8 result, the average value $\frac{P}{\dot{P}} = 3.4 \times$

$10^5$ yr is calculated for the characteristic spin-up time. This is consistant with the value obtained with a significantly smaller temporal base line (cf. Lamb et al. 1976). The time of zero orbital phase is delayed by 0.002 days from that expected by an extrapolation of UHURU results (Schreier 1975). This effect, while not of great statistical significance, suggests a binary period increase, similar to that observed in Cen X-3 (Tuohy, 1976).

The real time mode obtains temporal resolution of 20 msec for pulse-height-analyzed events. After the pulse period was accurately determined, this spectral data was folded at the period and divided into 62 independent temporal bins. Figures 4-7 and 4-8 show the resultant energy integrated light curves for the pulses obtained respectively with the total RL and the RN data. There is evident similarity between the two. They both show a double peaked pulse, with a dominant first peak, and an intensity minimum following the second peak. This pulse shape is the same as that shown in Doxsey et al. (1973) and Holt et al. (1974). If the RN data are divided by binary phase as in the preceeding section, the resultant pulse shapes are shown in Figure 4-9. Again there is a remarkable consistency in these forms. If the pulse is examined on shorter time scales (10 min, 30 min) there are still no significant departures from this shape. Other investigators have suggested the existence in their data of a small additional pulse in the flattened region away from the major double-peaked pulse. It is clear from this data that a stable minimum region directly follows the major pulse. The succeeding flattened portion of the light curve is a relative maximum. If another pulse does in fact exist in this region, it is very small relative to the main pulse and

the emission there is dominated by the off-pulse component (i.e. that component immediately prior to the main pulse).

There are spectral changes, sometimes dramatic, with pulse phase. The RL pulse light curve divided into six energy bands is displayed in Figure 4-10. Generally, the pulse shape is seen from 2 to $\sim$ 30 keV. The first peak becomes noticeably narrower with energy. This is shown best in the 12.6 - 19.1 keV energy range. The rise is slower than that at lower energies, and the peak occurs at a later phase. Similar results were reported by Doxsey et al. (1973) and Holt et al. (1974). At this time spectra are shown for different portions of the pulse. Figure 4-11 shows the results of an automatic computer spectral fitting program which was applied to each of the 62 RL pulse bins. The simple model chosen for this procedure was a power law with absorption and a narrow iron line centered at 6.7 keV. The positions of the first and seconds peaks are illustrated. Although there is a lot of scatter in the histograms there is one clear trend. In the second half of the first peak the spectrum hardens and absorption disappears, as perhaps does the iron line. This spectral break occured in the RN data also, but one fold bin later. (The reference time for all real time pulse period folds is day 243.0). This implied an error of 0.0000002 sec in the pulse period, if the spectral break actually occurs at the same phase. This error is smaller than the error calculated based on the pulse shape coherence principle, and is used to suggest a more accurate period.

In order to improve the statistical quality of spectra by pulse phase, several bins corresponding to the same pulse region are combined. Bins 1-10 and 52-62 in both RL and RN are called the off-pulse spectrum (OP). The first peak (FP1 and FP2), the second peak (SP), and pulse

minimum (PM) spectra are defined on Figures 4-7 and 4-8. Only the feature separating FP1 and FP2 is sharp enough to necessitate a choice of different bins for the two data sets.

The total OP spectra have the same form as the total Her X-1 spectrum. They are fit by a power law model with a single line near 6.5 keV, and similar number index and absorption. The line must be broad to fit the RN data, while a narrow line also fits the RL data. However, the line equivalent width is now 0.690 keV $\pm$ 0.216 keV. The OP rate is approximately half the average total Her X-1 rate. Since this measured equivalent width is about twice the equivalent width in the total spectrum (see Section A), it is possible that all of the iron emission originates in the OP spectrum. This emission may extend over phase regions including the pulse, suggesting the use of this spectrum as background for peak spectra. Figure 4-12 displays the RL : OP spectrum.

The FP1 spectra display iron band features when the eclipsed spectrum is used for background. However, when the respective OP spectra are used for background, the resulting net spectra are simple power laws with absorption. The RN parameters are number index, $\alpha = 1.15^{+0.25}_{-0.15}$, and hydrogen column density, $N_H$ (atoms $cm^{-2}$) $= 9.0^{+11.0}_{-5.4} \times 10^{21}$. The corresponding RL parameters are $\alpha = 1.48^{+0.22}_{-0.23}$ and $N_H = 2.7^{+1.1}_{-1.3} \times 10^{22}$. The FP1 spectra are generally steeper with more absorption, and simpler than the average or OP spectra, when examined in this manner. The RL:FP1 spectrum is shown in Figure 4-13.

The second half of the first peak is harder than the first and without a low energy cutoff, as mentioned before. A direct comparison is made between the two halves by using FP1 as background for FP2 to detect net spectral changes. The result is a flat spectrum above $\sim$ 7 keV with

no emission whatever below this energy. If the source and background in this last analysis are interchanged, the result is a flat spectrum up to $\sim$ 7 keV with no emission above this energy. There is clearly a significant spectral change within the first peak. With the eclipse spectrum for background, the FP2 spectra can not be fit by a simple power law. For a power law with slope 0.7-0.8 and no absorption the low energy data ( $\lesssim$ 3 keV) are still significantly above the model. In order to account for this low energy excess, a line feature is included in the model. When this is done an acceptable fit is obtained with power law index $\alpha = 0.44^{+0.25}_{-0.24}$ and varying strengths of the low energy feature. Since this feature is near the detector low energy cut-off it is used as an artifact to simulate an additional low energy component and an actual line is not suggested. The strength of this feature indicates that the flux in the low energy excess is on the same order as that of the continuum for E $\lesssim$ 3 keV. Figure 4-14 shows the RN:FP2 spectrum.

The difference between the first and second peaks goes beyond an intensity difference. The spectral nature of the second peak is homogeneous. This is demonstrated in both RL and RN data when the peak is divided into two parts which are subtracted from each other in a procedure identical to the one described before for FP1 and FP2. The spectra resulting from these subtractions are flat over the entire energy range. In fact they are all fit acceptably by the function $E^{\circ}$ (i.e. an energy independent spectrum) which is never the case for first peak spectra. The SP spectra themselves differ somewhat in the RL and RN data sets. The RN:SP spectrum is fit by simple power law with number index $\alpha = 1.15^{+0.15}_{-0.10}$ and $N_H$ (atom $cm^{-2}$) $= 1.1^{+0.7}_{-0.4} \times 10^{22}$. The corresponding RL:SP spectrum is also steep ($\alpha = 1.3$) with high absorption ($N_H = 1.4 \times 10^{22}$),

REPRODUCIBILITY OF THE
ORIGINAL PAGE IS POOR



but with a line at 6.8 keV with equivalent width of 0.24 keV. The preceeding analysis used eclipsed spectra for background. If instead the pulse minimum (PM) spectra, discussed below, are used as background acceptable fits are obtained with simple, steep, highly-absorbed power law models reminiscent of the FP1 spectrum with OP background. The parameters are $\alpha = 1.55 \pm 0.20$, $N_H = 2.5^{+0.9}_{-1.1} \times 10^{22}$ for the RL data, and $\alpha = 1.2^{+0.3}_{-0.2}$, $N_H = 1.4^{+1.3}_{-0.9} \times 10^{22}$ for the RN data. If the OP spectra are used as SP background, deficiences appear in the iron band and acceptable fits are not obtained. The RN:SP spectrum with PM background is shown in Figure 4-15. The iron band deficiency has two sigma significance.

The RN:PM spectrum displayed in Figure 4-16 is the most stable of the spectra compiled by pulse phase. Both with regards to binary phase and from binary cycle to cycle its features remain unchanged. This spectrum is similar to the OP spectrum because strong iron band emission is present. The line equivalent width is $0.450 \pm 0.300$ keV in this case. One narrow line at $6.4 \pm 0.2$ keV is always present.

Pulsations continue during intensity dips. Figure 4-17 shows the pulse shape during the RN dip early on day 246. Even when the dip intensity is lowest (see RND2 in the Figure), the pulse is still apparent and the pulse fraction remains constant at approximately 0.4 the total emission.

The dip spectrum is grossly different from the high state spectrum (see next section). However the relative spectral changes with pulse phase remain. In particular the spectral break in the first peak is seen throughout the dips. Spectral variability with pulse phase implies differing physical conditions, source emitting regions, and/or geometries. This will be discussed in the following chapter.

The real time data taken during X-ray eclipses were also folded at the pulse period. No pulsations were detected at this period and a 3 sigma upper limit to the pulsed fraction of 8 per cent is obtained (cf. Pravdo et al. 1976c). If the assumption is made that the pulse has the same phase and duty cycle during eclipse, then the upper limit becomes one per cent. This last upper limit and the fact that the excess emission during eclipse is about 6 per cent of background (see Section A) implies that if this emission is from Her X-1, the pulsed fraction is decreased from the normal level.

C. High-Low State

This section contains the xenon detector results (Becker et al. 1976b) and the results of the argon detector observations of intensity dips. The xenon detector observed the transition from the X-ray low state to the high state. Although this $\sim$ 35 day cycle is not exactly periodic, the time of a transition can be predicted to within a couple of days. The accuracy of this prediction in the OSO-8 spin axis plan is evident in Figure 4-1 where an X-ray turn-on is displayed. A beat frequency of the $\sim$ 35 day cycle and the 1.7 day binary period corresponds to a 1.62 day period. This is the period of the intensity dips. (They therefore march backward in binary phase.) Since these dips are at least in part a manifestation of the high-low cycle, they will be discussed in this section.

Her X-1 was observed by the xenon detector prior to the initiation of the high state. The 1.7 day binary period was observed through normal eclipse behavior during this time. Figure 4-18d shows the pre-turn-on spectrum. This spectrum is similar to the normal high state spectrum but at only 6.2 per cent the 2-20 keV intensity. There is indication

of an absorption edge near 8 keV. Energy independent Compton scattering could be the cause of the flux attenuation. Since the spectrum does not exhibit more low energy absorption than during the high state, the intervening region must be highly ionized. The pre-turn-on flux was folded modulo the pulse period to check for the presence of pulsations. None were detected and the 3 sigma upper limit to the pulsed fraction is 3.7 per cent, assuming the phase and duty cycle of the pulse is the same as the post turn-on pulse. If the pulsed fraction is the same as that during the high state, than this upper limit implies that less than 9.7% of the X-rays are unscattered. This indicates an optical depth for Compton scattering $\sim$ 5.1 and an electron column density $N_e \sim 7.5 \times 10^{24}$ cm$^{-2}$.

The high state began on day 240.20$\pm$0.01 which corresponds to a binary phase of 0.232$\pm$0.006 consistent with prior turn-ons. Normal high state intensity was reached after about two hours. During this time a mid-turn-on spectrum was obtained. Figure 4-18b shows this spectrum and Figure 4-18a shows the normal high state spectrum acquired afterwards. Since the xenon detector is efficient up to $\sim$ 60 keV, the high energy cut-off is evident in this last Figure. This cut-off could not be fit with the functional form in equation (1-17). In order to characterize it and fit the spectrum, an *ad hoc* function of the form $\exp [ - (E - P_3)/P_4]$ is multiplied by the power law model for $E > P_3$. The mid-turn-on spectrum (Figure 4-18b) is found to fit the same spectral form but with additional low energy absorption. Table 4-3 lists the parameters for the xenon spectra.

Spectra observed during intensity dips are highly absorbed in low energies. Absorption edges are also apparent. Figure 4-19 shows successive spectra as an intensity dip progresses. The absorption by cold

intervening matter reaches a maximum hydrogen column density of 6 x $10^{23}$ $cm^2$, a factor of $\sim 10^2$ larger than in the normal high state. All spectra show edges at $\sim$ 7 keV and highly absorbed spectra (Figure 4-19d) also show an edge near 4 keV.

An intensity dip which occurs in the xenon data does not fall into the 1.6 day period. This spectrum shown in Figure 4-18c (see Table 4-3 for its parameters) however is similar to the highly absorbed dip spectra which do exhibit this periodicity. Once again, an edge at $\sim$ 7 keV is apparent. There is a $\sim$ 30 per cent drop in the unabsorbed (high energy) intensity which again may be due to Compton scattering. A column density of electrons, $N_e \sim 5 \times 10^{23}$ $cm^{-2}$, is sufficient to explain this decrease and consistent with the column density of hydrogen in the dip spectra.

# CHAPTER V

# DISCUSSION

Several interesting and new results have arisen from the OSO-8 observation of Hercules X-1. The major ones are: line emission in the iron band, a spectral change midway through the major peak in the pulse, and the various spectra obtained during the transition from an X-ray low state to a high state. Some of these results fit nicely into the framework of the emerging model for the Her X-1/HZ Her systems. Others are more puzzling. The implications of the results will be considered in the course of a discussion of the nature of the binary system.

## A. HZ Herculis

X-rays from Her X-1 are the result of mass transfer from HZ Herculis to the compact object. Roche lobe overflow through the inner Lagrangian (L1) point is the most likely mechanism for this transfer. There is probably also an evaporative stellar wind (Basko et al. 1976). A recent observation studied 1.2 sec optical pulsations from HZ Herculis (Middleditch and Nelson 1976) as a function of binary phase. They found that the optical pulsations arise from a region near the theoretical estimate for the Roche surface. Also, from the binary phase correlation with these pulsations, they suggest that this surface is cusped rather than rounded. This is typical of the shape of a Roche lobe (see Figure 5-1). The Roche lobe radius calculated from equation (1-19) for $M_{HZ\ Her}/M_{Her\ X-1} = 2$ and $R_s = 7 \times 10^{11}$ cm, is $R_c = 3 \times 10^{11}$ cm. This value is identical to the observed occultation radius for the source going into eclipse. HZ Herculis probably fills its Roche lobe.

The abruptness of the eclipse demonstrates the opacity of material within the Roche lobe, and the scale height of the atmosphere above it.

The scale height is $\sim 3 \times 10^9$ cm. Just before entering eclipse the extra path length that emission from Her X-1 must travel is $\sim 10^{12}$ cm ($\sin i \sim 1$) compared to the geometry at phase 0.5. The average neutral hydrogen density in this region (see Figure 5-1) must be less than $10^9$ cm$^{-3}$ since no low energy absorption change is observed. The electron density must be less than $10^{12}$ cm$^{-3}$ because no attenuation by Compton scattering is observed. Since matter is ionized in this region of the stellar wind (cf. Hatchett and McCray 1976) the latter constraint is more relevant. Using a simple homogeneous slab model for this region, the mass density due to an evaporative wind is given by

$$\rho = \dot{M}/Av \qquad (5-1)$$

where $\dot{M}$ is the mass loss rate, v the wind velocity and A the slab area. Basko et al. (1976) estimate that $\dot{M} \simeq 5 \times 10^{16}$ g/sec for HZ Herculis and that $v \lesssim$ sound speed $\sim$ 20 Km/sec. The resulting average value for the electron density, $N_e \sim 10^{11}$ cm$^{-3}$, is consistent with the observed upper limit.

Reflection of X-rays from the surface of HZ Herculis was discussed by Basko et al. 1974. Although the reflected X-ray luminosity is too small relative to the high state intensity ($\lesssim$ 10%) to be observed during an X-ray high state, the K$\alpha$ fluorescence line of iron is sufficiently intense to show up over the continuum. However the intensity of this feature should be correlated with binary phase because different areas and orientations of the X-ray illuminated HZ Her surface are in the field of view. The absence of such correlation of the equivalent width of the observed line features with binary phase appears to rule out this mechanism as an important source. However, the observation that much

of the excess emission observed during eclipse is concentrated in the iron band suggests that this effect may exist at a low level. This last result suffers from the possibility of contamination from other sources, and poor statistics. An interesting future experiment could observe HZ Herculis in X-rays during an X-ray eclipse with a detector featuring a small collimated field of view ($\lesssim 1°$) to eliminate contaminating sources and a large collecting area to improve statistics. This detector would also be useful in observing rapid transitions into and out of eclipse, in order to model the atmospheric regions.

B. Accretion Disk

It is likely that the matter from HZ Her crossing the $L_1$ point forms a flat accretion disk around Her X-1. The precession of this disk may be responsible for $\sim$ 35 day high-low state. If the disk is tilted (Roberts 1974) and twisted (Petterson 1975) by a 35 day precessional period of HZ Her, then periodic occultations of Her X-1 will occur. The mid-low-state intensity maximum is explainable by the orientation of a titlted disk (Jones and Forman 1976). The rapid high-state onset ($\sim$ 2 hrs.) and gradual decline are more easily explained by the asymmetry of the twisted disk (see Figure 5-2). Long term optical (Deeter et al. 1976) and X-ray (Holt et al. 1976) observations of the system suggest that detailed intensity variations are reproduced each 35 day cycle. This may imply that stable substructure exists within the disk. That is, regions of the disk have varying opacity to X-rays. This would affect not only the X-ray intensity in the line of sight, but also the X-rays illuminating HZ Her and thus the optical emission.

In either model the disk may be surrounded by a layer of hot coronal gas. Just prior to the beginning of the high state, X-rays from Her X-1

will be scattered by this gas. The pre-turn-on spectrum (Fig. 4-19d) may be indicative of this scattered flux. The reduction in intensity (0.06 high state intensity) and absence of pulsations in this flux can be explained by the incoherence introduced by Compton scattering. The lack of low energy absorption in this spectrum indicates that this gas is highly ionized, with $T \gtrsim 10^7$ K so that oxygen ions are fully ionized. There is some indication of an absorption edge in this spectrum near $\sim$ 8 keV. If this is an iron absorption edge, the temperature can not be much above $10^8$ K for iron to retain its electrons. The edge energy $\sim$ 8 keV is consistent with $T \sim 10^7$ K; the neutral iron edge energy is 7.1 keV (Becker et al. 1976b). A maximum optical depth, $\tau_c < 3$, is deduced from the absence of spectral distortions (Comptonization) from the normal high state spectrum. The high state spectrum can be fit by a power law model which changes slope near $\sim$ 25 keV. Compton scattering through a plasma with $kT_e \ll h\nu$ (i.e. $kT_e \lesssim 10^7$K) will modify the source spectrum (Illarionov and Sunyaev 1972). Figure 5-3 shows the pre-turn-on data superimposed on a histogram of the model high state spectrum described above. With a Compton optical depth $\tau_c = 3$, the model is too deficient at high energies to fit the data. The minimum $\tau_c$ deduced from the lack of pulsations (see Chapter IV) is $\tau_c \gtrsim 5$ for direct emission. This demonstrates that the pre-turn-on emission is probably scattered emission and is not observed directly from the source.

The regularly occuring X-ray intensity dips have a period of 1.6 days. This represents a beat between the $\sim$ 35 day precessional period of the disk and the binary period of revolution. Gerend and Boynton (1976) suggest that the system reproduces a particular orientation with this period, which allows mass transfer that is inhibited at other times.

This matter is not fully ionized ($Z \geq 8$) and obscures the X-ray source. The spectra of dips observed by OSO-8 indicate low energy absorption and absorption edges of iron and perhaps other abundant elements such as Si, S, Ca, and Ni. This extra mass corresponds to an ambient density increase by a factor of at least 100. Precise identification of lines and edges in these spectra is statistics limited because the intensity dips last for short times ($\sim$ 0.1d) and, of course, have low count rates. The resolution of the gas proportional counters is another limiting factor. There is no evidence at this time that elemental abundances in this material differ substantially from solar system values.

The intensity dip which occurred on day 240 while spectrally similar to the regular dips, does not fall into the 1.6 day period. It occurs at phase 0.61 immediately following the high state turn-on at phase 0.23. Giacconi et al. (1973) also observed anomalous dips at similar binary phase, immediately after high state initiations near phase 0.25. After initiation at phase $\sim$ 0.68, a relatively similar dip would not be observable because it would take place during an eclipse. This obscuration may be due to a stable feature near the edge of the accretion disk which is cooler than the coronal gas--considerable low energy absorption is present in the spectrum. It is unclear whether the regularly occurring dips which start about half a day after this dip can be of the same origin. Perhaps there is some connection between the anomalous dip and the turn-ons which occur at similar late phase. The edge of the disk is also composed of cooler material. Considerable low energy absorption is seen during turn-on.

### C. Iron Band Emission

The discussion of this binary system began with HZ Her (Section A)

and will conclude with Her X-1. At this point it is appropriate to discuss in more detail the iron band emission, before proceeding. This is so because the absence of correlation between the intensity of this emission and binary phase, probably places the emitting region close to Her X-1 rather than close to HZ Her.

If this emission is iron line emission, possible mechanisms are thermal, charge exchange, or fluorescence. None of these seem to adequately fit the data because in the data line energies change with no apparent periodicity. The effective temperature of the hard Her X-1 spectrum appears to be too high for thermal lines to be formed. The spectrum integrated over binary phase exhibits a broad line (FWHM $= 2.4 \pm 0.7$ keV) which indicates either an intrinsic width or more probably, a variable energy in a narrower feature. Thermal motion can not explain this width since the temperature would exceed $kT \simeq 10^3$ MeV. Iron nuclei with streaming velocities, $B \simeq 0.2$, could produce a broad feature via charge exchange. However this X-ray production rate from accreting matter is too small by a factor of $10^4$ to explain the observed energy flux in the emission features (see Appendix B).

Line fluorescence will produce a narrow line (width $\lesssim$ 10 eV). The line energy varies with the ionization state of the fluorescing atoms. For example, the 2P-1S (K$\alpha$) transition energy of iron is 6.4 keV for the neutral atom and 6.9 keV for the hydrogenic ion. However, this range of energies is less than the observed range--5.5 to 8.2 keV. Using Table (1-2) the equivalent widths contributed by the fluorescence of other abundant elements can be estimated. The only significant iron band feature in addition to the K$\alpha$ iron line occurs at $\sim$ 8 keV, with about 1/4 the intensity. This feature combines the contribution of Fe K$\beta$ and Ni K$\alpha$ emission. While this helps to explain the high energy iron band emission,

it does not explain the basic observational problem. That is, that the line energy shifts from spectrum to spectrum (cf. Figures 4-3, 4-4). If the temperature or ionization equilibrium of the emitting region were to change, the line energies would change. However lines near $\sim$ 6 keV would not occur. Also spectra like the one shown in Figure 4-4 are not explained. Emission near 6.5 keV (the normal line energy) is suppressed, while lines appear at higher and lower energies.

There is some question whether these observations are due to systematic problems. For example, the line emission in the RL data (see Chapter IV) when the detector was set to a lower gain, is concentrated in a single line at an approximately constant energy. The other data often shows more than one line at varying energies. However this fact was recognized and great care was taken to calibrate both sets of data properly. Even with the small uncertainities in this procedure, it is not possible to reconcile the data. A further indication of the reality of these variable line energies comes from the analysis of data from the other fast X-ray pulsar, Cen X-3. Swank (1976) has observed a similar phenomonom in data taken with a detector which was not commanded into a different gain.

Line fluorescence is the least objectionable of the models discussed above. Basko et al. (1974) and Hatchett and McCray (1976b) both suggest that iron line fluorescence will be a significant process in this system. Despite the objections raised above, this emission will be discussed in the context of this model, to obtain at least an order of magnitude understanding of the effect.

## D. Alfven Radius

Her X-1 has a soft X-ray flux ( < 1 keV) which has comparable power to the hard X-ray flux. Schulman et al. (1975) fit their soft X-ray

spectral observation with a $T \simeq 10^6$ K thermal spectrum. Catura and Acton (1975) find a similar temperature blackbody fit. The minimum radius for a blackbody with the observed luminosity and temperature is $R \simeq 10^8$ cm. This value is similar to estimates of the Alfven radius $R_A$. Matter which is being transferred from the accretion disk into the magnetosphere of Her X-1 could accumulate and form an opaque shell at $R_A$ where a balance exists between magnetic and gravitational forces (McCray and Lamb 1976). Basko and Sunyaev (1976a) suggest that such a shell would be optically thick with respect to Thomson scattering, and would reradiate in soft X-rays about half of the primary X-ray flux. It could also have optical emission which could pulsate at the pulsar period.

Iron line fluorescence would occur in this shell. Also, since ionizational equilibrium here is more dependent on photoionizational rather than collisional processes, many more ionization states of iron can be present at the same temperature (cf. Hatchett et al. 1976). Since iron is the major source of absorptive opacity for photons of energy $\gtrsim$ 8 keV it is approximately correct to assume that all these photons ionize the iron (cf. Hatchett and McCray 1976b). The fluorescence energy flux from this shell can be approximated by

$$L_{Fe} = 4\pi D^2 \omega_K E_K \int_8 \frac{dN}{dE} \left[1 - \exp(\sigma(E) N_{Fe})\right] dE \qquad (5\text{-}2)$$

where D is the distance to Her X-1, $\omega_k$ is the K fluorescence yield, $E_K$ the line energy, $\frac{dN}{dE}$ the photon spectral density, $N_{Fe}$ the iron column density, and $\sigma(E)$ the iron absorption cross section (Figure 1-2). For shell number density $5 \times 10^{19}$, and thickness $10^5$ cm, similar to McCray and Lamb (1976) parameters, then $N_{Fe} = 1.3 \times 10^{20}$ cm$^{-2}$ for cosmic iron

abundance. From equation (5-1), $L_{Fe}$ is found to be $\sim 10^{35}$ erg/s which is approximately the observed luminosity.

Fluorescence from material in the stellar wind is another possible source for this emission. The model described in Hatchett and McCray (1976) also provides the correct order of magnitude estimate for $L_{Fe}$ if the wind density is $10^{11}$ cm$^{-3}$ and the emitting region radius is on the order of the system size. However, if the shell exists at $R_A$, then the reradiated K X-rays after fluorescence in the shell will not have sufficient energy to ionize atoms farther away from the neutron star. Another possible fluorescence target is the coronal gas around the accretion disk mentioned in Section A. This reflected flux however is at a low level and does not appear to contain significant line emission, at least in the pre-turn-on configuration.

## D. Her X-1

The existence of regular 1.2 sec pulsations from Her X-1 is the most convincing reason that it is a neutron star. The pulsar has continued to spin-up, at $\sim$ 0.1 the rate estimated in equation (1-22). This implies an error in the assumed Her X-1 parameters (the neutron star radius is the most sensitive) or an overestimate of the efficiency of the angular momentum transfer process.

Spectral analysis of this pulse has yielded new results. Iron band emission is strongest in pulse regions other than the peaks. The underlying continuum spectra however are similar. Perhaps the off-peak emission is Compton scattered X-rays from the source region which creates the peak emission. Iron is fluoresced in the scatterer. However if a significant amount of the continuum off-peak emission is scattered, then the optical depth of the scatterer must be small because of the

absence of spectral distortions. This could be made more quantitative if the observation of spectra with pulse phase is performed with a xenon-filled detector with larger spectral range. This is a possible future observation for the CXS.

The energy of lines emitted near Her X-1 will be altered for two reasons. First, the strong gravitational field near the surface of a neutron star will red shift the lines with $\frac{\Delta E}{E} \simeq 0.1$ for typical mass and radius. A 6.4 keV iron line emitted near the surface would be observed at $\sim$ 5.8 keV. Observed emission features do extend down to this energy. A range of energies is expected if emission is observed from various radii. Still this does not explain why the observed line energies change with no apparent periodicity. The second effect is due to the strong magnetic fields which may exist at the stellar surface. It has been shown (Rau et al. 1975) that the total atomic binding energy and shell structure are radically changed in fields, $B \simeq 10^{12}$g. While calculations of the line energies have not yet been done, they also may be altered. In the neutron star model for X-ray pulsars, strong magnetic fields are crucial because the pulses originate at the magnetic poles. Until line energies are calculated under these conditions it is not possible to determine if the features can come from material near a neutron star surface.

The stability of the pulse shape is a very important fact. A similar shape has been observed at least since 1973 (Doxsey et al. 1973). (The earlier UHURU result of changing pulse shapes on small time scales has been withdrawn). The mechanism of pulse formation must be very stable. Rotation of a neutron star seems to be the most likely means of achieving such a fast regular pulse. There are several detailed models for pulse

formation from an obliquely rotating neutron star. They all agree that the "hot spots" at the magnetic poles, upon which the accreting matter is deposited, create pulses as they rotate across the line of sight. However the hot spot radiates isotropically. It cannot form the deeply modulated pulses which are observed (cf. Basko and Sunyaev 1976b). There must be an additional beaming mechanism. Several have been proposed and they agree to varying extents with the observations, although no model explains all the features.

Leaving aside the iron band emission, the underlying continua are very similar across the entire pulse except for a region of spectral hardening which begins midway through the first peak within 0.02 phase and persists for 0.08 phase ($\sim 30°$). The rapidity of this spectral break implies a maximum source region size (light travel distance) of $\sim 6 \times 10^8$ cm. The photon intensity does not change when this break occurs. This appears to rule out scattering processes (Comptonization), if the pulsed emission is truly beamed. Any gross spectral change would be caused by substantial optical depth which would also cause considerable attenuation (i.e. scattering out of the beam). The "lack" of low energy absorption in the hardened spectrum is an artifact due to the increase in high energy photons. The low energy flux remains about constant. In general, intensity changes across the pulse can not be due to free-free absorption since the spectra never show low energy deficiencies.

All of the beaming mechanisms proposed thus far relate the beam directionality to magnetic field lines. In addition, a change in the viewing direction relative to the magnetic field lines alters the observed spectrum. This could be the cause of the observed spectral change. If the double-peaked structure is considered for the moment to be a single

broad feature, the spectral hardening is symmetrical with respect to it (see Figure 4-9). In other words, the pulse peak is narrower at higher energies (from 2 - 20 keV at least). This assumes that the viewing direction parallel to the magnetic axis (i.e. at zero angle) corresponds to the center of the double-peaked feature and to the hardest spectrum by pulse phase. A similar spectral hardening in the peak has been observed in the Cen X-3 pulse (Swank 1976).

The model of Basko and Sunyaev (1975) for a "pencil" beam does predict that the pulse spectrum will depend on the angle between the viewing direction and the magnetic field, but with a spectral softening at smaller angles. They assume that the surface magnetic field is $\sim 10^{12}$g so that outgoing photons are scattered anisotropically leading to a pencil beam. Tsuruta (1974) suggests that with a judicious choice of parameters (magnetic field strength, density) the pulse could narrow at higher energies. This model assumed that the pulse shape is variable and that the depth of the minimum between the two peaks is also variable and dependent on the accretion rate. X-rays are absorbed by the accreting mass to form the interpeak minimum. However this observation shows that this interpeak region exhibits no additional low energy absorption. Also the stability of the pulse shape in the present observation indicates either that the accretion rate does not change or that the pulse shape is not dependent on this rate.

If the radiation from a neutron star is cyclotron radiation it also can be beamed. Relativistic electrons emit beamed radiation in a pencil pattern if their velocities are parallel to the field. Non-relativistic electrons form a "fan" pattern perpendicular to the field. In both cases the beam narrows with increasing energy (Gnedin and Sunyaev

1973). For the relativistic case the photon energies increase with electron velocities, and the beam width decreases. Higher order harmonies of the cyclotron frequency have narrower beams in the non-relativistic case.

Polarization measurements could distinguish a fan beam from a pencil beam. The former should be almost completely linearly polarized while the later would be circularly polarized by tens of per cent. The Columbia X-ray polarimeter on OSO-8 will be able to set an upper limit of $\sim$ 5% on linear polarization from Her X-1 (Wolff 1976). Different portions of the pulse are likely to have different polarizations. If the peaks are due to a combined fan and pencil beam, then the type of polarization could change mid-peak. The off-peak emission would be unpolarized if it represents a diffuse reflected component.

The region of spectral hardening extends over only $\sim$ 1/3 of the double-peaked structure. This may indicate the intrinsic beam width. There is an intensity asymmetry relative to this intrinsic beam. It is interesting to note that the intensity deficiencies in the pulse--the inter-peak and the pulse minimum (PM) regions--both occur later than and within $\frac{\pi}{2}$ phase of the center of the hardened region. This could imply a stable region of scattering which reduces the intensities during these phases, and which lags behind the intrinsic beam. We assume that a Thomson scattering region exists which distorts the pulse shape but not the spectrum. The optical depth with respect to Thomson scattering must be $\lesssim 1$ to perform these functions. This is not atypical for the walls of accretion columns or the shell at the Alfven radius (Basko and Sunyaev 1976a, McCray and Lamb 1976). The optical depth with phase and the "de-scattered" pulse are shown in Figure 5-4.

The Thomson scattering region is relatively thick at both ends and thin in the middle (see Figure 5-4). This could correspond to a crosssection of the accretion column. The thick regions are the walls of the column and the thin region is the center. The leading edge (wall) is more prominent. The phase lag of the scatterer relative to the intrinsic beam could be due to a twist in the accretion column (Figure 5-5). Since the magnetic field strength decreases rapidly with distance ($\sim R^{-3}$) and the co-rotation velocity increases ($\sim R$) it is possible that the magnetic field lines and the accretion column bend in the direction opposite to the rotation, relative to the normal from the magnetic pole. Near the surface this bending would be minimal so that the beaming would remain in the radial direction. At larger radii the bending increases and this results in the phase lag of the scattering region.

Recently Basko and Sunyaev (1976b) have reported that many of the previously suggested beaming mechanisms (see above) fail when the X-ray luminosity, $L_x \gtrsim 10^{37}$ erg/s. This is close to the Her X-1 luminosity. They suggest alternatively that the pulse modulation is due to material at the Alfven surface which periodically shields part of the emitting region. Compton optical depths on the order of 1-3 in their model are sufficient to explain the modulation but not the detailed pulse structure. The present model explains the pulse structure by the shape of the scattering accretion column. Since the Her X-1 pulse shape does not change it is more reasonable to assume that the scattering region is rigidly tied to the pulse formation region (hot spot). The accretion column fulfills this last requirement better than material at the Alfven surface. McCray and Lamb (1976) speculate that the Alfven shell is most dense at the magnetic equator and transparent at high magnetic latitudes except at the accretion columns. If this is the case, the scattering opacity

near the magnetic pole is likely to vary in a similar manner to the model depicted in Figure 5-4.

Before dismissing entirely the pulsating white dwarf model for Her X-1 the following points should be noted. With the pulsation period inversely proportional to the mass, an accretion rate between $10^{-5}$ and $10^{-6}$ $M_o$/yr can explain both the luminosity and the spin-up. The double peaked structure might be explained by the shocks caused by expansion and contraction each period (cf. Gorenstein and Tucker 1974). The pulse minimum following the peaks is suggestive of a period of relaxation in an oscillator. Also the light travel distance corresponding to the spectral break is similar to a white dwarf radius. The model of Blumenthal et al. (1972) predicts some features which are observed. They predict a temperature change across the peak which however is more gradual than the observed change. Also the white dwarf surface should emit like a $\sim$ $5 \times 10^5$ K blackbody. The temperature and radius of the surface are similar to the parameters of the soft X-ray source. Finally they suggest that optical pulsations could arise from Her X-1, and these have been observed (Middleditch and Nelson 1976). However, the extreme stability of the pulse period and shape are difficult to explain with this model (but see DeGregoria 1974).

## F. The Spectrum

The Her X-1 spectrum when observed with the extended energy range of a xenon detector reveals a spectral steepening near $\sim$25 keV (see Figure 18a). The spectrum can be fit by a power law with number index $\sim$ 1 which changes at $\sim$ 25 keV to an index of $\sim$ 8. This is a very significant change. Energy-dependent Compton scattering in a strong magnetic field ($\sim 10^{12}$g)

can explain this high energy cutoff. In the model of Boldt et al. (1976) the ratio of cutoff energy to e-folding energy (for the $\sim$ exponential fall-off) depends on the optical depth for Thomson scattering which is fixed by the elemental abundances of the nuclear material responsible for stopping freely falling matter. This ratio ($P_3/P_4$ in Table 4-3) ranges from 2.4 to 2.7 in the extremes of normal elemental abundances to pure iron. The observed ratio is in this range.

A recent model of Tsygan (1976) explains the X-ray beaming by the accretion of a relativistic plasma onto the magnetic pole. The beam narrows with increasing energy below $E_o$, where $E_o = 3\ kT_s$ and $T_s$ is the effective plasma temperature on the stellar surface. Also, for $h\nu < E_o$ the overall spectrum is flat (number index $\sim 1$) while for $h\nu > E_o$ the spectrum falls exponentially. However, in this model $E_o \simeq 20$ keV for a magnetic field of $3 \times 10^{10}$g and $E_o \simeq 200$ keV for a field of $3 \times 10^{13}$g. The cyclotron models and the anisotropic Thomson scattering models discussed above both predict the existence of a powerful emission "gyroline" at the cyclotron energy. In these models the magnetic field is $\sim 10^{12}$g so that the cyclotron energy is $\gtrsim$ 10 keV. Boldt et al. (1976) conclude that the field strength is $\sim 10^{13}$g. If no "gyroline" is observed in the hard X-ray regime (and none has been thus far) this may indicate that the magnetic field is not as strong as these models indicate. The cyclotron energy in the Tsygan (1976) model is in the soft X-ray regime and not a strong resonance since the average photon energy is much greater.

## G. Summary

Hercules X-1 radiates $\sim 10^{37}$ erg in stable X-ray pulses second. It is clearly an interesting object. This thesis has presented

the results of long-term detailed X-ray spectroscopy of the Her X-1 system. The following model is supported: Her X-1 is a magnetized obliquely rotating neutron star. The energy source is the gravitational energy of accreting matter. This matter is transferred by Roche lobe overflow from the binary companion HZ Herculis. It forms an accretion disk which precesses with a $\sim$ 35 day period and periodically occults the X-ray source. A hot coronal gas surrounds the disk and reflects X-rays prior to the X-ray turn-on. At the inner disk radius an opaque shell of matter forms. It provides reflected X-ray emission and perhaps iron band fluorescence radiation. The X-ray beaming mechanism is energy dependent and probably is related to the neutron star magnetic field. The pulse shape can be understood by variable optical depths to Thomson scattering in a stable intervening region. This region could be the accretion column itself which is twisted by the effects of rotation.

The variable line energies in the iron band emission is the most puzzling result. It is possible that the details of these X-ray features are reproduced each 35 day cycle, just as details in the optical emission are. As the accretion disk precesses relative to Her X-1, density and temperature changes could occur in the matter distribution of the Alfven shell and upper accretion column. The changing physical conditions lead to variable line energies. A similar observation of Her X-1 at the $\sim$ 35 day phase would test this hypothesis.

The upcoming High Energy Astronomical Observatories (HEAO) could perform useful observations of Her X-1. HEAO B features a solid-state X-ray detector which has better resolution than the CXS gas proportional counters. Its energy range extends up to 4 keV. While HEAO B is unable to observe the features in the iron band emission, lower energy features

during intensity dips could be studied. This observation could identify the elements and their abundances (lower Z than iron) in the occulting material. HEAO A features proportional counters similar to the OSO-8 xenon-filled detectors but with much larger effective areas ($\sim$ 1000 $cm^2$). Although these detectors perform 360° scans (ie. small on-source duty cycles) their large areas would enable them to obtain spectra with good statistics during low states in the Her X-1 emission: eclipses, intensity dips, and the X-ray low state. Spectra should be examined at each phase of the $\sim$ 35 day cycle to yield new information concerning the accretion disk.

The Cosmic X-ray Spectroscopy experiment (CXS) on OSO-8 can perform useful observations of Her X-1 in the future. An observation similar to the present one, but with the extended energy range and larger effective area of the xenon-filled detector is called for. In particular the spectral shape of the high energy cutoff should be examined with respect to binary and especially pulse phase. Some models predict that the X-ray beam width should increase above the cutoff energy (Tsygan 1976). This could be studied with this observation. Also a search for the gyro-line at the cyclotron frequency would be continued at greater sensitivity in the energy range up to $\sim$60 keV.

# APPENDIX A

## CXS RESPONSE FUNCTION

A primary goal of the GSFC Cosmic X-ray Spectroscopy experiment (CXS) is to obtain accurate X-ray spectra of celestial sources. To do this, it is necessary to know the detector response (output) to an incident X-ray spectrum (input). Equation (3-6) in the text is the integral representation of the detector response function. In practice the integral is replaced by a sum over energy steps, viz:

$$O(E_o) = \sum_E I(E)\, R(E, E_o) \qquad (A\text{-}1)$$

where I(E) is the incident photon number spectrum, $O(E_o)$ is the observed number spectrum and $R(E,E_o)$ is the response function. The function $R(E,E_o)$ is calculated for each value of E, the incident photon energy, in a computer program using normalizations from calibration, semi-empirical, and theoretical results.

The calculation of $R(E,E_o)$ proceeds as follows. A set of six parameters are determined in calibration. A electron beam facility at GSFC is used to create bremsstrahlung X-ray spectra and X-ray fluorescence lines. Also, a solid state detector is often useful in comparisons with the response of the CXS proportional counters. The CXS energy resolution can be represented as a Gaussian function of energy with variance

$$\sigma_2 = A_1 E + A_2 E^2 \qquad (A\text{-}2)$$

where $A_1$ and $A_2$ are two of the six parameters. Figure A1 is a picture of the pulse height spectrum of a CXS detector in response to several calibration sources. Each white dot is one pulse height channel. The

line width of several channels indicates the resolution of the detector since the decay line has an intrinsic width of less than one channel.

The next two parameters, $A_3$ and $A_4$, are the gain and offset of the system. The energy of a photon (count) as a function of channel number can be written as

$$E(N) = A_3 N + A_4 \qquad (A\text{-}3)$$

where N is the channel number. $A_3$ and $A_4$ are obtained by fitting calibration data from known lines spaning the range of our response.

The parameter $A_5$, the fluorescence yield, is taken from Storm and Israel (1967). It is the probability that a resonance photon is created in the interaction (see text-Chapter II). The last parameter, $A_6$, is a measurement of anti-coincident losses from electrons. The losses occur when the electrons are detected in cells other than the interaction cell. This parameter is estimated semi-empirically and normalized by calibration.

The following is a short outline of how the six parameters are used to create the response function for the argon detector for a photon of energy E.

I. E > 3.2 keV (K edge of argon)

  A. Kα resonance escape

    1. Probability for Kα escape. Remaining energy is

       $E - E_{K_\alpha} = E'$

    2. Probability that electrons do not cause anticoincidence losses $\sim (1 - A_6) \quad (E'/11)^2$

       Normalized to 11 keV.

B. $K_B$ resonance escape - similar to K above.

C. No fluorescence $\sim (1 - A_5)$, Energy = E.

II. E < 3.2 keV

A. Electron anti-coincidence $(1 - A_6)\ (E/11)^2$

III. For all E

A. Percentage of photons transmitted through the window and absorbed by the gas.

B. For E < 25 keV a factor $\lesssim 1$ for those photons which intersect the wire anodes and are lost.

C. Distribution of energies E or E' as per the resolution, gain, and offset parameters.

1. Energy width of channel is $A_3$

2. Energy of channel is $A_4 + A_3N$

3. Resolution effect is $R(E,E_o) \propto (2\pi\sigma^2)^{-1/2} \exp [E-E_o)^2/2\sigma^2]$ with $\sigma$ defined in equation A2.

Using the above prescription an incident photon of energy is distributed over the detector pulse height channels. The sum of the probabilities of detection over all the channels is the total probability that the photon will be detected.

For the xenon detectors three more parameters are introduced corresponding to a small non-linearity in the gain, a discontinuity near the L edge of xenon, and anticoincidence losses due to K resonance photons. Small non-linearities and discontinuities were discovered by examining the spectrum of the Crab nebula which is believed to have a flat featureless power law spectrum in the CXS range, and is a very strong source (good statistics). There are for this gas three photon energy ranges: E < 4.8 keV, 4.8 < E < 34.6 keV, and E > 34.6 keV with the boundary

energies corresponding to the L and K edges of xenon. An incident photon in each range is treated in a manner analogous to that described above. The general procedure for calculating the response function is the same.

## APPENDIX B

## CHARGE EXCHANGE FROM ACCRETING MATTER

Matter accreting onto the surface of a neutron star with radius, $R = 10^6$ cm, and mass, $M = M_o$, will attain a free-fall velocity

$$V_{ff} = \left(\frac{2GM}{R}\right)^{\frac{1}{2}} \simeq 0.5c \qquad (B\text{-}1)$$

Collisions may slow infalling matter somewhat but detailed calculations (cf. Lamb 1974) show that this velocity is approximately reached. At a distance of $\sim$ 10R and while stopping in the surface the ions have a velocity corresponding to $\sim$ 13 MeV/ nucleon, at which (cf. Serlemitsos et al. 1973; Watson 1976) the charge exchange cross section leading to K X-ray emission peaks. The number or "multiplicity" of K X-rays created per accreting iron nucleus taken together with the accretion rate yields the energy flux in this process.

The multiplicity of K X-rays from non-relativistic cosmic ray nuclei has been calculated by Pravdo and Boldt (1975) for oxygen, and Watson (1976) for iron and other nuclei. Although the propagation processes differ, since the multiplicity has been shown to be approximately density-independent, it is reasonable to assume similar values. The two preceeding references agree approximately on determination of the oxygen multiplicity, $M_o = 90$ and 77 respectively. The latter reference also gives $M_{Fe} = 11$. An upper limit $M_{Fe} = 100$ is chosen for this calculation.

The distance to Her X-1 is estimated by Forman et al. (1972) to be 5.8 Kpc. Using this value, the Her X-1 luminosity is $L_x = 1.6 \times 10^{37}$ erg/s as measured by OSO-8. The mass accretion rate from

$$L_x = \epsilon GM\dot{M}/R \qquad (B\text{-}2)$$

REPRODUCIBILITY OF THE
ORIGINAL PAGE IS POOR



with efficiency $\varepsilon = 0.1$, is $1.2 \times 10^{18}$ g/s or $1.9 \times 10^{-8}$ $M_\odot$/yr. This corresponds to an infall rate of $2 \times 10^{37}$ Fe atoms/s if normal cosmic iron abundance is present in the plasma (see Table 1-2). The resultant energy flux in this process in the steady state is

$$L_{Fe} = 2 \times 10^{37} M_{Fe} E_K \text{ erg/s} \qquad (B\text{-}3)$$

where $E_K$ is the line energy. This flux, $L_{Fe} = 2 \times 10^{31}$ erg/s, is a factor of $10^4$ below the observed value $L_{Fe}^{obs} = 2.7 \times 10^{35}$ erg/s.

It is possible that the charge exchange cross section and thus the multiplicity is affected by the intense magnetic fields near the neutron star surface. A modification to the other atomic cross sections under these conditions has already been discussed (cf. Lodenquai et al. 1974).

In the white dwarf model, $V_{ff} \sim 0.05$ (equation B1 with $R = 10^8$ cm). However there may be anomalous ionization (in general ions retain fewer electrons at higher velocities) in the extreme conditions present in an accretion column, so that K X-ray charge exchange could exist. A white dwarf must have a larger accretion rate than a neutron star with the same given luminosity and efficiency since the rate is proportional to $R^{-1}$. Even under these circumstances, and assuming that iron nuclei have the same multiplicity in the white dwarf model, the calculated $L_{Fe}$ is still only $10^{-2}$ of the observed flux.

REFERENCES


Alme, M. L. and Wilson, J. R. 1974, Ap. J., 194, 147.

Bahcall, J. and Bahcall, N. 1972, Ap. J. (Letters), 184, L1.

Basko, M. M. and Sunyaev, R. A. 1973, Astr. and Space Sci., 23, 117.

Basko, M. M. and Sunyaev, R. A. 1975, Astron. and Astr., 42, 311.

Basko, M. M., Sunyaev, R. A., and Titarchuk, L. G. 1974, Astron. and Astr., 31, 249.

Basko, M. M., Hatchett, S., McCray, R., and Sunyaev, R. A. 1976, preprint.

Basko, M. M. and Sunyaev, R. A. 1976a, Mon. Not. R.A.S., 175, 395.

Basko, M. M. and Sunyaev, R. A. 1976b, preprint.

Becker, R. H., Boldt, E. A., Holt, S. S., Pravdo, S. H., Rothschild, R. E., Serlemitsos, P. J., and Swank, J. H. 1976a, Ap. J. (Letters), 209, in press.

Becker, R. H., Boldt, E. A., Holt, S. S., Pravdo, S. H., Rothschild, R. E., Serlemitsos, P. J., Smith, B. H., and Swank, J. H. 1976b, submitted to Ap. J.

Blumenthal, G. R. and Tucker, W. H. 1974 in R. Giacconi and H. Gursky (eds.) X-ray Astronomy, D. Reidel Publishing Co., Dordrecht-Holland, Chapter 3.

Blumenthal, G. R., Cavaliere, A., Rose, W. K., and Tucker, W. H. 1972, Ap. J., 173, 213.

Boldt, E. A. 1969 in H. Ogelman and J. Wayland (eds.) Lectures in High-Energy Astrophysics, NASA SP-199, 49.

Boldt, E. A., Holt, S. S., and Serlemitsos, P. J. 1971, Ap. J. (Letters), 164, L9.

Boldt, E. A. 1974 in F. B. McDonald and C. E. Fichtel (eds.) High Energy Particles and Quanta in Astrophysics, M.I.T. Press, Cambridge, Mass., 368.

Boldt, E. A., Holt, S. S., Rothschild, R. E., and Serlemitsos, P. J. 1976, Astron. & Astr., 50, 161.

Bowyer, C. S., Byron, E. T., Chubb, T. A., and Friedman, H. 1964, Science, 146, 912.

Boynton, P. E. 1975 in H. Gursky and R. Ruffini (eds.) Neutron Stars, Black Holes, and Binary X-ray Sources, D. Reidel Publ. Co., Dordrecht-Holland, pp. 221-234.

Brecher, K. 1972, Nature, 239, 325.

Brecher, K. and Wasserman, I. 1974, Ap. J. (Letters), 193, L125.

Brown, R. D. and Gould, R. J. 1970, Phys. Rev. D, D1, 2252.

Cameron, A.G.W. 1973, Space Sci. Rev., 15, 121.

Catura, R. C. and Acton, L. W. 1975, Ap. J. (Letters), 202, L5.

Clark, G. W., Bradt, H. V., Lewin, W.H.G., Markert, T. H., Schnopper, H. W., and Sprott, G. F. 1972, Ap. J. (Letters), 177, L109.

Clark, G. W., Buff, J., Canizares, C., Hayakawa, S., Jernigan, J. G., and Li, F. 1976, Bull. of Am. Phys. Soc., 21, 544.

Cooke, B. A. and Page, C. G. 1975, Nature, 256, 712.

Cooley, J. W., Lewis, P.A.W., and Welch, P. D. 1967, IBM Watson Research Center, (Yorktown Heights, N.Y.) Preprint TC-1743.

Crampton, D. and Hutchings, J. B. 1972, Ap. J. (Letters), 178, L65.

Davidson, K. 1973, Nat. of Phys. Sci., 246, 1.

Davidson, K. and Ostriker, J. P. 1973, Ap. J., 179, 585.

Deeter, J., Crosa, L., Gerend, D., and Boynton, P. E. 1976, Ap. J., 206, 861.

DeGregoria, A. J. 1974, Ap. J., 189, 555.

DeGregoria, A. and Woltjer, L. 1973, Nat. Phys. Sci., 246, 108.

Doxsey, R., Bradt, H. V., Levine, A., Murthy, G. T., Rappaport, S., and Spada, G. 1973, Ap. J. (Letters), 182, L25.

Fabian, A. C., Pringle, J. E., and Rees, M. J. 1973, Nature, 244, 212.

Felten, J. E. and Rees, M. J. 1972, Astron. and Astr., 17, 226.

Fireman, E. L. 1974, Ap. J., 187, 57.

Forman, W., Jones, C., and Liller, W. 1972, Ap. J. (Letters), 177, L103.

Fritz, G., Henry, R., Meekins, J., Chubb, T. A., and Friedman, H. 1969, Science, 164, 709.

Fritz, G., Naranan, S. Schulman, S., Yentis, D., Friedman, H., Davidsen, A., Henry, R., and Snyder, W. 1976, submitted to Ap. J. (Letters).

Gerend, D. and Boyton P. 1976, preprint.

Giacconi, R., Gursky, H., Paolini, F. R., and Rossi, B. B. 1962, Phys. Rev. Letters, 9, 439.

Giacconi, R., Gursky, H., Kellogg, E., Levinson, R., Schreier, E., and Tananbaum, H. 1973, Ap. J., 184, 227.

Giacconi, R. 1974 in Astrophysics and Gravitation, Proc. 6th International Solray Conference (L'Universite de Bruxelles), p. 27.

Ginzburg, V. L. and Syrovatskii, S. I. 1964, The Origin of Cosmic Rays, Pergamon Press, Elmsford, N.Y.

Gnedin, Yu. N. and Sunyaev, R. A. 1973, Astron. and Astr., 25, 233.

Gnedin, Yu. N. and Sunyaev, R. A. 1974, Astron. and Astr., 36, 379.

Gorenstein, P. and Tucker, W. H. 1974 in R. Giacconi and H. Gursky (eds.) X-Ray Astronomy, D. Reidel Publ. Co., Dordrecht-Holland, p. 284.

Grindlay, J., Gursky, H., Schopper, H., Parsignault, D. R., Heise, J., Brinkman, A. C., and Schrijver, J. 1976, Ap. J. (Letters), 205, L127.

Handbook of Chemistry and Physics 1963, 44th ed., C. D. Hodgeman ed. (The Chemical Rubber Publ. Co., Cleveland).

Hatchett, S., Buff, J., and McCray, R. 1976, Ap. J., 206, 847.

Hatchett, S. and McCray 1976a, Bull. of A.A.S., 8, 315.

Hatchett, S. and McCray 1976b, preprint.

Hayakowa, S. and Matsuoka, M. 1964, Progr. Theoret. Phys. Supple., No. 30, P. 204.

Holt, S. S. 1974 in F. B. McDonald and C. E. Fichtel (eds.) High Energy Particles and Quanta in Astrophysics, M.I.T. Press, Cambridge, Mass., pp. 308-367.

Holt, S. S., Boldt, E. A., Rothschild, R. E., Saba, J.L.R., and Serlemitsos, P. J. 1974, Ap. J., 190, L109.

Holt, S. S., Boldt, E. A., Kaluzienski, L. J., Serlemitsos, P. J., and Swank, J. H. 1976, submitted to Nature.

Hubble, J. H. 1971, Atomic Data, 3, 241.

Illarionov, A. and Sunyaev, R. 1972, Soviet Astronomy - AJ, 16, 45.

Iyengar, V. W., Manchanda, R. K., Durgaprasad, N., Gokhale, G. S., Kunte, P. K. and Sreekantan, B. V. 1974, Nature, 251, 292.

Jackson, J. D. 1962, Classical Electrodynamics, John Wiley and Sons, Inc., New York.

Jones, C. and Forman, W. 1976, preprint.

Karzas, W. J. and Latter, R. 1961, Ap. J. Suppl., 6, 167.

Katz, J. I. 1973, Nat. Phys. Sci., 246, 87.

Kraft, R. P. 1975 in H. Gursky and R. Ruffini (eds.) Neutron Stars, Black Holes, and Binary X-ray Sources, D. Reidel Publ. Co., Dordrecht-Holland, pp. 235-253.

Krzeminsky, W. 1973, IAU Circ. No. 2537.

Kurfess, J. D. and Crosa, L. 1973, Nat. Phys. Sci., 245, 116.

Lamb, F. K. 1974 International Conference on X-rays in Space, U. of Calgary, Alberta, Canada.

Lamb, F. K., Pethick, C. J., and Pines, D. 1973, Ap. J., 184, 271.

Lamb, F. K., Pines, D. and Shaham, J. 1976, X-ray Binaries, NASA SP-389, p. 141.

Lampton, M., Margon, B., and Bowyer, S. 1976, Ap. J., 208, 177.

Lewin, W.H.G., Doty, J., Clark, G. W., Rappaport, S. A., Bradt, H.V.D., Doxsey, R., Hearn, D., Hoffman, J. A., Jernigan, J. G., Li, F. K., Mayer, W., McClintock, J., Primini, F., and Richardson, J. 1976, submitted to Ap. J. (Letters).

Liller, W. 1972, IAU Circ., No. 2427.

Lodenguai, S., Canuto, V., Ruderman, M., and Tsuruta, S. 1974, Ap. J., 190, 141.

Manchanda, R. K., Iyengar, V. S., Durgaprasad, N., Gokhale, G. S., Kunte, P. K., and Sreekantan, B. V. 1973, Nat. Phys. Sci., 244, 59.

Maraschi, L., Reina, C., and Treves, A. 1974, Astron. and Astr., 35, 389.

McClintock, J. E., Rappaport, S., Joss, P. C., Bradt, H., Buff, J., Clark, G. W., Hearn, ., Lewin, W.H.G., Matilsky, T., Mayer, W., and Primini, F. 1976, Ap. J. (Letters), 206, L99.

McCray, R. and Hatchett, S. 1975, Ap. J., 199, 196.

McCray, R. and Lamb, F. K. 1976, Ap. J. (Letters), 204, L115.

McKee, C., Lecar, M., and Wheeler, J. 1976, Bull. of AAS, 8, 421.

Mewe, R. 1972, Astron. and Astr., 20, 215.

Middleditch, J. and Nelson, J. 1976, Ap. J., 208, 567.

Novikov, I. D. and Thorne, K. S. 1973, in C. DeWitt and B. DeWitt (eds.) Black Holes, Gordon and Breach, N.Y., p. 362.

Omidvar, K., Golden, J. E., McGuire, J. H., and Weaver, L. 1976, Phys. Rev. A., A13, 500.

Oppenheimer, J. R. and Volkoff, G. 1939, Phys. Rev., 55, 374.

Ostriker, J. 1971, Ann. Rev. Astron., 9, 353.

Petterson, J. A. 1975, Ap. J. (Letters), 201, L61.

Pravdo, S. H. and Boldt, E. A. 1975, Ap. J., 200, 727.

Pravdo, S. H., Becker, R. H., Boldt, E. A., Holt, S. S., Rothschild, R. E., Serlemitsos, P. J., and Swank, J. H. 1976a, Bull. of APS, 21, 543.

Pravdo, S. H., Becker, R. H., Boldt, E. A., Holt, S. S., Rothschild, R. E., Serlemitsos, P. J., and Swank, J. H. 1976b, Ap. J. (Letters), 206, L41.

Pravdo, S. H., Becker, R. H., Boldt, E. A., Holt, S. S., Rothschild, R. E., Serlemitsos, P. J., and Swank, J. H. 1976c, Ap. J. (Letters), 208, L67.

Prendergast, K. H. and Burbidge, G. R. 1968, Ap. J. (Letters), 151, L83.

Pringle, J. E. and Rees, M. J. 1972, Astron. and Astr., 21, 1.

Rau, A.R.P., Mueller, R. O., and Spruch, L. 1975, Phys. Rev. A., A11, 1865.

Raymond, J., Smith, B., and Cox, D. 1975, preprint.

Roberts, W. J. 1974, Ap. J., 187, 575.

Rothschild, R. E., Boldt, E. A., Holt, S. S., and Serlemitsos, P. J. 1974, Ap. J. (Letters), 188, L13.

Rothschild, R. E., Becker, R. E., Boldt, E. A., Holt, S. S., Pravdo, S. H., Serlemitsos, P. J., and Swank, J. H. 1976, preprint.

Ruffini, R. and Wilson, J. 1976, Phys. Rev. Letters, 32, 324.

Ryter, C. 1976, X-ray Binaries, NASA SP-389, p. 189.

Salpeter, E. 1973 in H. Bradt and R. Giacconi (eds.) "X- and Gamma-Ray Astronomy", IAU Symp., 55, 135.

Sandage, A. 1961, The Hubble Atlas of Galaxies, Carnegie Institute of Washington, Wash., E.C., p. 50.

Schiff, H. 1954, Canadian J. Phys., 32, 393.

Schulman, S., Friedman, H., Fritz, G., Henry, R. C., and Yentis, D. J. 1975, Ap. J. (Letters), 199, L101.

Schreier, E., Levinson, R., Gursky, H., Kellogg, E., Tananbaum, H., and Giacconi, R. 1972, Ap. J. (Letters), 172, L79.

Schreier, E. 1975, private communication.

Serlemitsos, P. J., Boldt, E. A., Holt, S. S., Ramaty, R., and Briskan, A. F. 1973, Ap. J. (Letters), 184, L1.

Serlemitsos, P. J., Boldt, E. A., Holt, S. S., Rothschild, R. E. 1975, Ap. J. (Letters), 201, L9.

Serlemitsos, P. J., Becker, R. H., Holt, S. S., Pravdo, S. H., Rothschild, R. E., and Swank, J. H. 1976a, X-ray Binaries, NASA SP-389, p. 77.

Serlemitsos, P. J., Boldt, E. A., Holt, S. S., Smith, B. H., and Swank, J. H. 1976b, preprint.

Sharma, D. P., Jain, A. K., Kasturiransan, K., Jayanthi, V. B., and Rao, V. R. 1973, Nat. Phys. Sci., 246, 107.

Silk, J. and Steigman, G. 1969, Phys. Rev. Letters, 23, 597.

Sofia, S. 1967, Ap. J. (Letters), 149, L59.

Storm, E. and Israel, H. I. 1967, Photon Cross Sections from .001 to 100 MeV, for Elements 1 through 100, LASL Document LA-3753.

Swank, J. H., Becker, R. H., Boldt, E. A., Holt, S. S., Pravdo, S. H., Rothschild, R. E., and Serlemitsos, P. J. 1976a, X-ray Binaries, NASA SP-389, p. 207.

Swank, J. H., Becker, R. H., Boldt, E. A., Holt, S. S., Pravdo, S. H., Rothschild, R. E., and Serlemitsos, P. J. 1976b, Ap. J. (Letters), 209, in press.

Swank, J. H. 1976c, private communication.

Tananbaum, H., Gursky, H., Kellogg, E. M., Levinson, R., Scheier, E. and Giacconi, R. 1972, Ap. J. (Letters), 174, L143.

Tananbaum, H. and Tucker, W. H. 1974 in R. Giacconi and H. Gursky (eds.) X-ray Astronomy, D. Reidel Publ. Co., Dordrecht-Holland, Chapter 6.

Tsruta, S. 1974, Culham Conference on Cosmic Plasma Physics.

Tsygan, A. I. 1976, preprint.

Tucker, W. H. and Koren, M. 1971, Ap. J., 168, 283.

Tuohy, I. R. 1976, X-ray Binaries, NASA SP-389.

Ulmer, M. P., Baity, W. A., Wheaton, W. A., and Peterson, L. E. 1973, Ap. J. (Letters), 181, L33.

Watson, W. D. 1976, Ap. J., 206, 842.

Wolff, R. 1976, private communication.

Zel'dovich, Ya. B. and Novikov, I. D. 1971, Relativistic Astrophysics, Vol. 1, (Chicago: University of Chicago Press), Chapter 13.

Zel'dovich, Ya. B. and Shakura, N. I. 1969, Soviet Astronomy - AJ, 13, 175.

TABLE 1-1

| ION | LINE | LINE ENERGY (keV) | EFFECTIVE COLLISION STRENGTH |
|---|---|---|---|
| SiXIV | | 2.567 | 0.00056 |
| | | 2.500 | 0.00043 |
| | Kβ | 2.460 | 0.0012 |
| | Kα | 2.000 | 0.0077 |
| SiXIII | | 2.344 | 0.002 |
| | | 2.290 | 0.001 |
| | Kβ | 2.180 | 0.0025 |
| SXVI | | 3.340 | 0.00043 |
| | | 3.270 | 0.00033 |
| | Kβ | 3.100 | 0.00094 |
| | Kα | 2.620 | 0.0059 |
| SXIV | | 3.080 | 0.001 |
| | Kβ | 2.870 | 0.0019 |
| | Kα | 2.460 | 0.012 |
| | Kα | 2.450 | 0.005 |
| | Kα | 2.430 | 0.008 |
| CaXX | | 5.250 | 0.00028 |
| | | 5.150 | 0.00021 |
| | Kβ | 4.860 | 0.00060 |
| | Kα | 4.100 | 0.0037 |
| CaXIX | | 4.850 | 0.0007 |
| | | 4.750 | 0.0006 |
| | Kβ | 4.570 | 0.0012 |
| CaXIX | Kα | 3.900 | 0.008 |
| | Kα | 3.880 | 0.004 |
| | Kα | 3.850 | 0.005 |
| FeXXVI | | 8.840 | 0.00016 |
| | | 8.650 | 0.00012 |
| | Kβ | 8.190 | 0.00036 |
| | Kα | 6.900 | 0.0022 |
| FeXXV | | 8.400 | 0.0004 |
| | | 8.200 | 0.0003 |
| | Kβ | 7.760 | 0.0008 |
| | Kα | 6.630 | 0.0045 |
| | Kα | 6.600 | 0.0026 |
| | Kα | 6.561 | 0.0022 |
| NiXXVIII | | 10.300 | 0.00016 |
| | | 10.000 | 0.00012 |
| | Kβ | 9.450 | 0.00031 |
| | Kα | 8.000 | 0.0019 |
| NiXXVII | | 9.600 | 0.0004 |
| | | 9.550 | 0.0003 |
| | Kβ | 9.050 | 0.0007 |
| | Kα | 7.750 | 0.0038 |
| | Kα | 7.700 | 0.0023 |
| | Kα | 7.650 | 0.0018 |
| NiXXVI | | 2.010 | 0.0061 |

FLUORESCENCE YIELDS AND ABUNDANCES

TABLE 1-2

| ION | K FLUORESCENCE YIELD | ABUNDANCE/H |
|---|---|---|
| Si | 0.041 | $3.15 \times 10^{-4}$ |
| S | 0.069 | $1.57 \times 10^{-5}$ |
| Ca | 0.151 | $2.27 \times 10^{-6}$ |
| Fe | 0.312 | $2.61 \times 10^{-5}$ |
| Ni | 0.371 | $1.51 \times 10^{-6}$ |

TABLE 2-1

## DETECTOR COMPLEMENT

| DET. | TYPE | OUTER VOLUME | INNER VOLUME | COLL. | WINDOW | AREA ($CM^2$) | ENERGY RANGE | VETO |
|---|---|---|---|---|---|---|---|---|
| A | SINGLE VOLUME | – | XENON-METHANE | 5° | .002 Be | 271 | 2-60 keV | 3 SIDES |
| B | SINGLE VOLUME | – | ARGON-METHANE | 3° | .002 Be | 76 | 2-20 keV | 3 SIDES |
| C | DOUBLE VOLUME | PROPANE-NEON | XENON-METHANE | 5° | .002 MYLAR | 244 | 2-60 keV | 4 SIDES |

THE 3 EXPERIMENT DETECTORS ARE MULTI-WIRE PROPORTIONAL COUNTERS EACH WITH 4 LAYERS OF ANODES

TABLE 3-2

CONFIDENCE LIMITS ON DEVIATIONS

FROM

MINIMUM ACCEPTABLE $\chi^2$

| Number of Sigma | Number of Parameters | | | | | | | | | |
|---|---|---|---|---|---|---|---|---|---|---|
| | 2 | 3 | 4 | 5 | 6 | 7 | 8 | 9 | 10 | 11 |
| 1 | 2.4 | 3.7 | 4.9 | 6.1 | 7.2 | 8.4 | 9.5 | 10.7 | 11.8 | 12.9 |
| 2 | 4.6 | 6.3 | 7.8 | 9.2 | 10.6 | 12.0 | 13.4 | 14.7 | 16.0 | 17.3 |
| 3 | 9.2 | 11.3 | 13.3 | 15.1 | 16.8 | 18.5 | 20.1 | 21.7 | 23.2 | 24.7 |

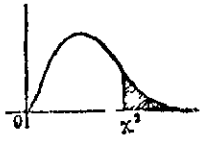


| Degrees of freedom | $P = 0.99$ | 0.98 | 0.95 | 0.90 | 0.80 | 0.70 |
|---|---|---|---|---|---|---|
| 1 | 0.000157 | 0.000628 | 0.00393 | 0.0158 | 0.0642 | 0.148 |
| 2 | 0.0201 | 0.0404 | 0.103 | 0.211 | 0.446 | 0.713 |
| 3 | 0.115 | 0.185 | 0.352 | 0.584 | 1.005 | 1.424 |
| 4 | 0.297 | 0.429 | 0.711 | 1.064 | 1.649 | 2.195 |
| 5 | 0.554 | 0.752 | 1.145 | 1.610 | 2.343 | 3.000 |
| 6 | 0.872 | 1.134 | 1.635 | 2.204 | 3.070 | 3.828 |
| 7 | 1.239 | 1.564 | 2.167 | 2.833 | 3.822 | 4.671 |
| 8 | 1.646 | 2.032 | 2.733 | 3.490 | 4.594 | 5.527 |
| 9 | 2.088 | 2.532 | 3.325 | 4.168 | 5.380 | 6.393 |
| 10 | 2.558 | 3.059 | 3.940 | 4.865 | 6.179 | 7.267 |
| 11 | 3.053 | 3.609 | 4.575 | 5.578 | 6.989 | 8.148 |
| 12 | 3.571 | 4.178 | 5.226 | 6.304 | 7.807 | 9.034 |
| 13 | 4.107 | 4.765 | 5.892 | 7.042 | 8.634 | 9.926 |
| 14 | 4.660 | 5.368 | 6.571 | 7.790 | 9.467 | 10.821 |
| 15 | 5.229 | 5.985 | 7.261 | 8.547 | 10.307 | 11.721 |
| 16 | 5.812 | 6.614 | 7.962 | 9.312 | 11.152 | 12.624 |
| 17 | 6.408 | 7.255 | 8.672 | 10.085 | 12.002 | 13.531 |
| 18 | 7.015 | 7.906 | 9.390 | 10.865 | 12.857 | 14.440 |
| 19 | 7.633 | 8.567 | 10.117 | 11.651 | 13.716 | 15.352 |
| 20 | 8.260 | 9.237 | 10.851 | 12.443 | 14.578 | 16.266 |
| 21 | 8.897 | 9.915 | 11.591 | 13.240 | 15.445 | 17.182 |
| 22 | 9.542 | 10.600 | 12.338 | 14.041 | 16.314 | 18.101 |
| 23 | 10.196 | 11.293 | 13.091 | 14.848 | 17.187 | 19.021 |
| 24 | 10.856 | 11.992 | 13.848 | 15.659 | 18.062 | 19.943 |
| 25 | 11.524 | 12.697 | 14.611 | 16.473 | 18.940 | 20.867 |
| 26 | 12.198 | 13.409 | 15.379 | 17.292 | 19.820 | 21.792 |
| 27 | 12.879 | 14.125 | 16.151 | 18.114 | 20.703 | 22.719 |
| 28 | 13.565 | 14.847 | 16.928 | 18.939 | 21.588 | 23.647 |
| 29 | 14.256 | 15.574 | 17.708 | 19.768 | 22.475 | 24.577 |
| 30 | 14.953 | 16.306 | 18.493 | 20.599 | 23.364 | 25.508 |

For degrees of freedom greater than 30, the expression $\sqrt{2\chi^2} - \sqrt{2n'-1}$ may be used as a normal deviate with unit variance, where $n'$ is the number of degrees of freedom.

Reproduced from *Statistical Methods for Research Workers*, 6th ed., with the permission of the author, R. A. Fisher, and his publishers, Oliver and Boyd (Edinburgh).

| Degrees of freedom | 0.50 | 0.30 | 0.20 | 0.10 | 0.05 | 0.02 | 0.01 |
|---|---|---|---|---|---|---|---|
| 1 | 0.455 | 1.074 | 1.642 | 2.706 | 3.841 | 5.412 | 6.635 |
| 2 | 1.386 | 2.408 | 3.219 | 4.605 | 5.991 | 7.824 | 9.210 |
| 3 | 2.366 | 3.665 | 4.642 | 6.251 | 7.815 | 9.837 | 11.341 |
| 4 | 3.357 | 4.878 | 5.989 | 7.779 | 9.488 | 11.668 | 13.277 |
| 5 | 4.351 | 6.064 | 7.289 | 9.236 | 11.070 | 13.388 | 15.086 |
| 6 | 5.348 | 7.231 | 8.558 | 10.645 | 12.592 | 15.033 | 16.812 |
| 7 | 6.346 | 8.383 | 9.803 | 12.017 | 14.067 | 16.622 | 18.475 |
| 8 | 7.344 | 9.524 | 11.030 | 13.362 | 15.507 | 18.168 | 20.090 |
| 9 | 8.343 | 10.656 | 12.242 | 14.684 | 16.919 | 19.679 | 21.666 |
| 10 | 9.342 | 11.781 | 13.442 | 15.987 | 18.307 | 21.161 | 23.209 |
| 11 | 10.341 | 12.899 | 14.631 | 17.275 | 19.675 | 22.618 | 24.725 |
| 12 | 11.340 | 14.011 | 15.812 | 18.549 | 21.026 | 24.054 | 26.217 |
| 13 | 12.340 | 15.119 | 16.985 | 19.812 | 22.362 | 25.472 | 27.688 |
| 14 | 13.339 | 16.222 | 18.151 | 21.064 | 23.685 | 26.873 | 29.141 |
| 15 | 14.339 | 17.322 | 19.311 | 22.307 | 24.996 | 28.259 | 30.578 |
| 16 | 15.338 | 18.418 | 20.465 | 23.542 | 26.296 | 29.633 | 32.000 |
| 17 | 16.338 | 19.511 | 21.615 | 24.769 | 27.587 | 30.995 | 33.409 |
| 18 | 17.338 | 20.601 | 22.760 | 25.989 | 28.869 | 32.346 | 34.805 |
| 19 | 18.338 | 21.689 | 23.900 | 27.204 | 30.144 | 33.687 | 36.191 |
| 20 | 19.337 | 22.775 | 25.038 | 28.412 | 31.410 | 35.020 | 37.566 |
| 21 | 20.337 | 23.858 | 26.171 | 29.615 | 32.671 | 36.343 | 38.932 |
| 22 | 21.337 | 24.939 | 27.301 | 30.813 | 33.924 | 37.[illegible] | 40.[illegible] |
| 23 | 22.337 | 26.018 | 28.429 | 32.007 | 35.172 | 38.[illegible] | 41.[illegible] |
| 24 | 23.337 | 27.096 | 29.553 | 33.196 | 36.415 | 40.271 | 42.[illegible] |
| 25 | 24.337 | 28.172 | 30.675 | 34.382 | 37.652 | 41.[illegible] | 44.314 |
| 26 | 25.336 | 29.246 | 31.795 | 35.563 | 38.885 | 42.[illegible] | 45.642 |
| 27 | 26.336 | 30.319 | 32.912 | 36.741 | 40.113 | 44.140 | 46.963 |
| 28 | 27.336 | 31.391 | 34.027 | 37.916 | 41.337 | 45.[illegible] | 48.278 |
| 29 | 28.336 | 32.461 | 35.139 | 39.087 | 42.557 | 46.693 | 49.588 |
| 30 | 29.336 | 33.530 | 36.250 | 40.256 | 43.773 | 47.962 | 50.892 |

TABLE 4-1. SPECTRUM BY BINARY PHASE

| SPECTRUM | PHASE | TIME(DAY) | SPECTRUM | PHASE | TIME(DAY) |
|---|---|---|---|---|---|
| S7a | 0.7 | 241.0265* | RL4 | 0.4 | 243.8860 |
| | 0.8 | .1658 | RL5 | 0.5 | 244.0560 |
| | 0.9 | .3358 | RL6 | 0.6 | .2261 |
| | 0.0 | .5058 | | 0.7 | .3961 |
| S1 | 0.1 | .6758 | | 0.8 | .5661 |
| S2 | 0.2 | .8458 | | 0.9 | .7361 |
| S3 | 0.3 | 242.0158 | | 0.0 | .9061 |
| S4 | 0.4 | .1859 | RN1 | 0.1 | 245.0761 |
| S5 | 0.5 | .3559 | RN2 | 0.2 | .2462 |
| S6 | 0.6 | .5259 | RN3 | 0.3 | .4162 |
| S7 | 0.7 | .6959 | RN4 | 0.4 | .5862 |
| | 0.8 | .7639* | RN5 | 0.5 | .7562 |
| | 0.9 | 243.0359 | RN6 | 0.6 | .9262 |
| | 0.0 | .2060 | | 0.7 | 246.0962 |
| RL1 | 0.1 | .3760 | | 0.8 | .2663 |
| RL2 | 0.2 | .5460 | | 0.9 | .4363 |
| RL3 | 0.3 | .7160 | | | |

TABLE 4-2. PROPERTIES OF SPECTRA BY BINARY PHASE

| SPECTRA | BINARY PHASE | | | | | | |
|---|---|---|---|---|---|---|---|
| | 1 | 2 | 3 | 4 | 5 | 6 | 7 |
| S | | | | | | | |
| Line Energy (keV) | 6.2 | 6.4 | 5.8 | 6.8 | 6.3 | 6.5 | 6.5 |
| Eq. W. (keV) | .170 | .320 | .104 | .301 | .335 | .379 | .379 |
| Line Energy | | | 7.8 | | | 8.2 | 6.1 |
| Eq. W. | | | .193 | | | .153 | .274 |
| RL | | | | | | | |
| Line Energy | 6.3 | 6.2 | 6.3 | 6.2 | 6.2 | 6.2 | |
| Eq. W. | .289 | .289 | .312 | .254 | .254 | .194 | |
| RN | | | | | | | |
| Line Energy | 5.5 | 6.2 | 6.4 | 6.0 | 6.0 | 5.6 | |
| Eq. W. | .149 | .156 | .306 | .104 | .252 | .119 | |
| Line Energy | 7.4 | 7.4 | 8.2 | 7.2 | | 7.0 | |
| Eq. W. | .338 | .184 | .171 | .153 | | .230 | |

Table 4-3

SPECTRAL PARAMETERS FOR HER X-1

| SPECTRUM | NUMBER INDEX $\alpha$ | COLUMN DENSITY $N_H$ (cold matter) atoms/cm$^2$ | P{3}(keV) | P{4}(keV) | $\chi^2$/Deg. of Freedom |
|---|---|---|---|---|---|
| post-turn-on | $0.91 \pm 0.05$ | $1. \pm 0.4 \times 10^{22}$ | $19.7^{+1.4}_{-1.7}$ | $7.3^{+3.6}_{-2.4}$ | 22.6/18 |
| mid-turn-on | 0.91* | $6.2^{+2.8}_{-1.7} \times 10^{22}$ | 19.7* | 7.3* | 23.5/21 |
| pre-turn-on | $0.85 \pm .25$ | $0 + 1.26 \times 10^{22}$ | 19.7* | 7.3* | 9.9/20 |
| dip | 0.91* | $2.9^{+.8}_{-.4} \times 10^{23}$ | 19.7* | 7.3* | 23.4/21 |

*not used as a free parameter

REPRODUCIBILITY OF THE
ORIGINAL PAGE IS POOR



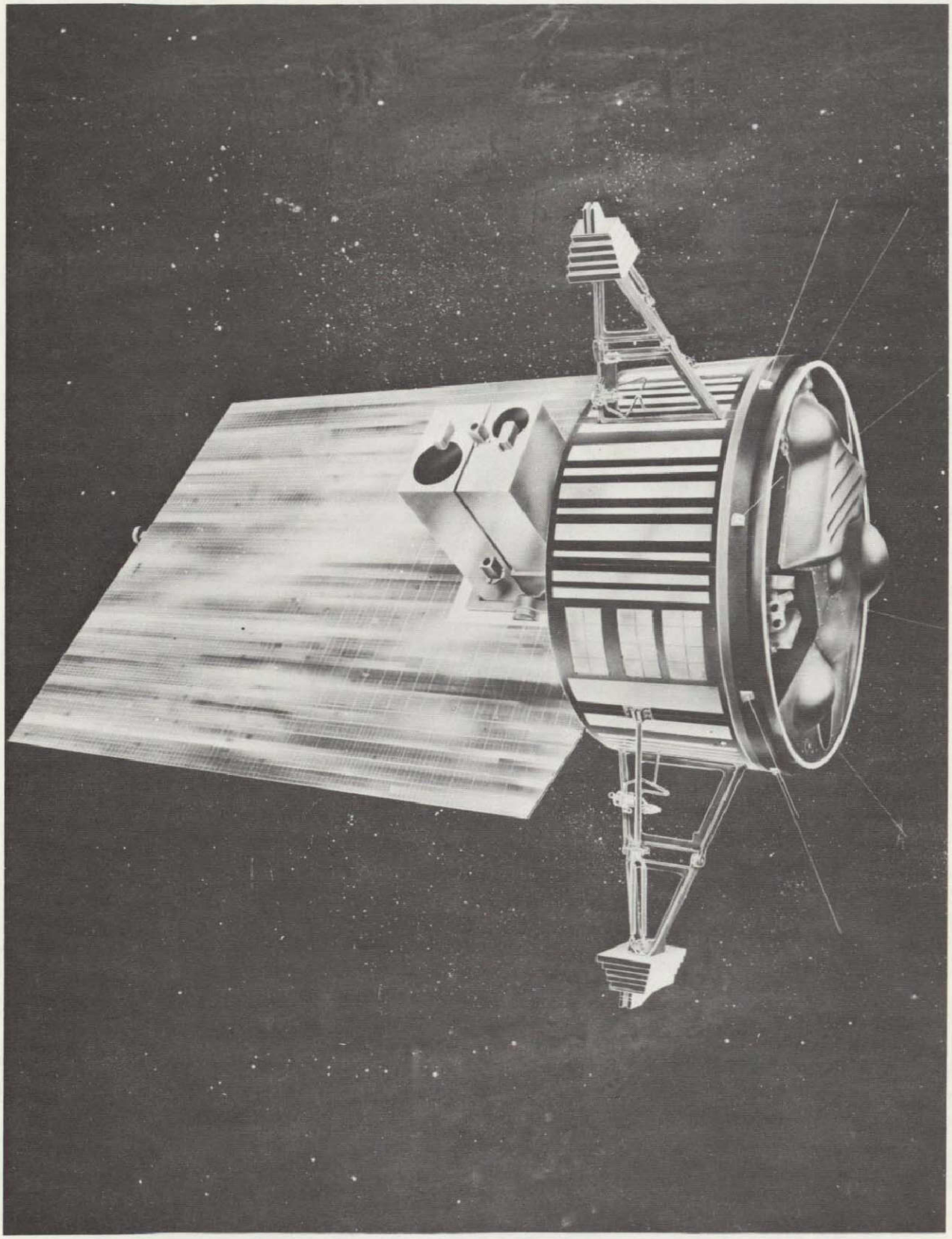

Figure 1-1

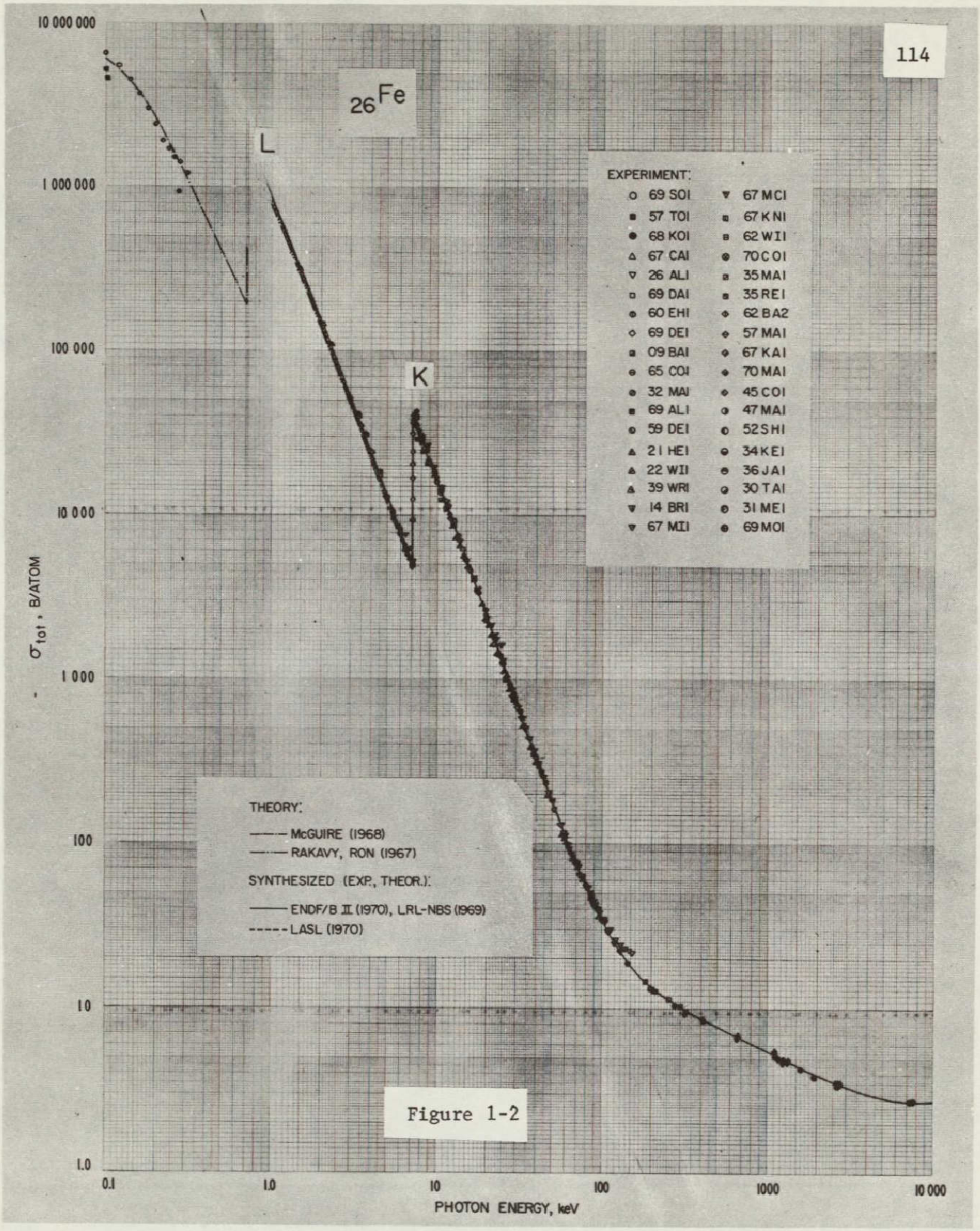
114
$_{26}$Fe
L
K
EXPERIMENT:
69 SOI
57 TOI
68 KOI
67 CAI
26 ALI
69 DAI
60 EHI
69 DEI
09 BAI
65 COI
32 MAI
69 ALI
59 DEI
21 HEI
22 WII
39 WRI
14 BRI
67 MII
67 MCI
67 KNI
62 WII
70 COI
35 MAI
35 REI
62 BA2
57 MAI
67 KAI
70 MAI
45 COI
47 MAI
52 SHI
34 KEI
36 JAI
30 TAI
31 MEI
69 MOI
THEORY:
McGUIRE (1968)
RAKAVY, RON (1967)
SYNTHESIZED (EXP., THEOR.):
ENDF/B II (1970), LRL-NBS (1969)
LASL (1970)
10 000 000
1 000 000
100 000
10 000
1 000
100
10
1.0
$\sigma_{tot}$, B/ATOM
0.1
1.0
10
100
1000
10 000
PHOTON ENERGY, keV

Figure 1-2

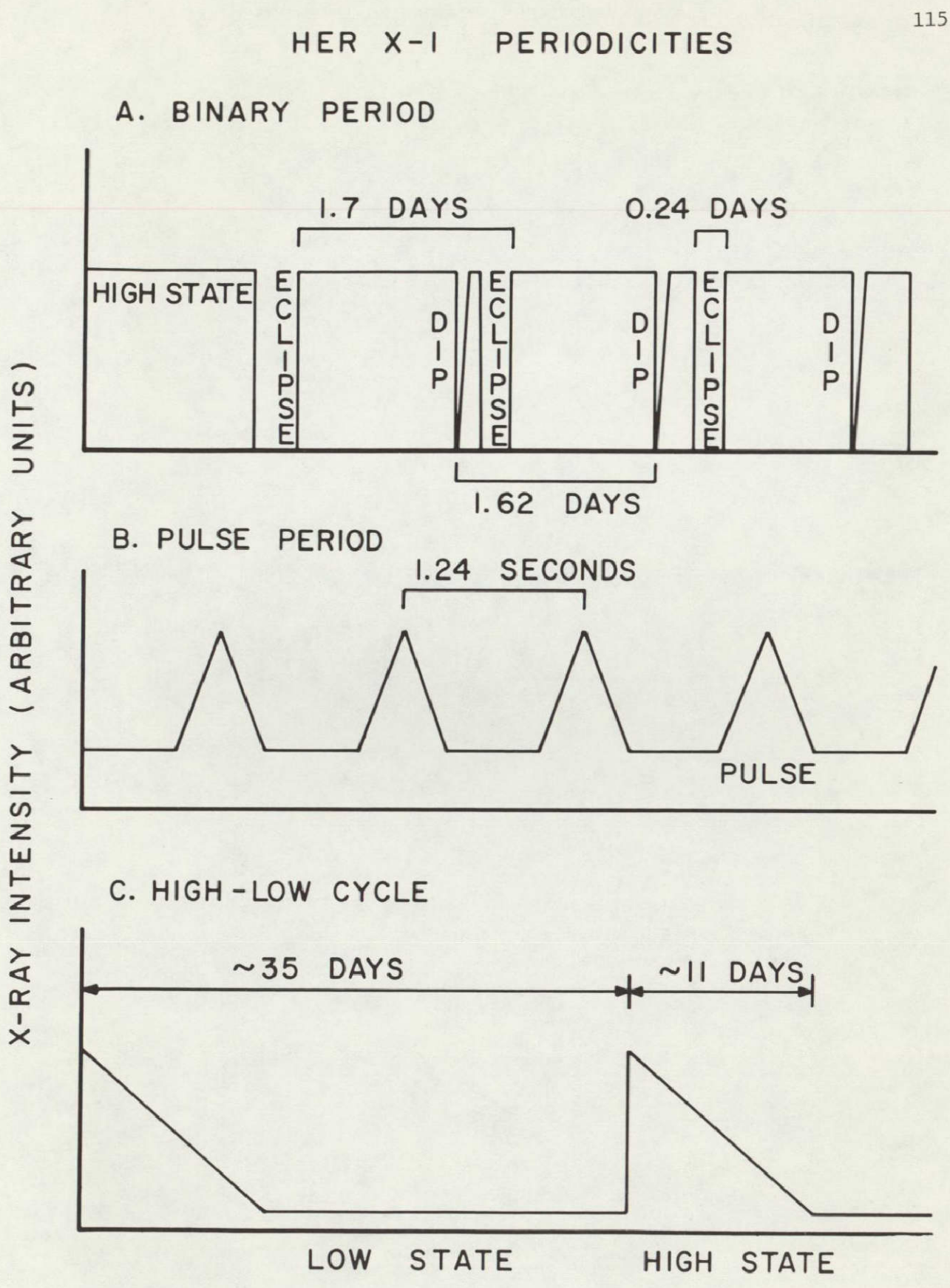
HER X-1 PERIODICITIES
A. BINARY PERIOD
1.7 DAYS
0.24 DAYS
HIGH STATE
ECLIPSE
DIP
ECLIPSE
DIP
ECLIPSE
DIP
1.62 DAYS
B. PULSE PERIOD
1.24 SECONDS
PULSE
C. HIGH-LOW CYCLE
~35 DAYS
~11 DAYS
LOW STATE
HIGH STATE
TIME
X-RAY INTENSITY (ARBITRARY UNITS)

Figure 1-3

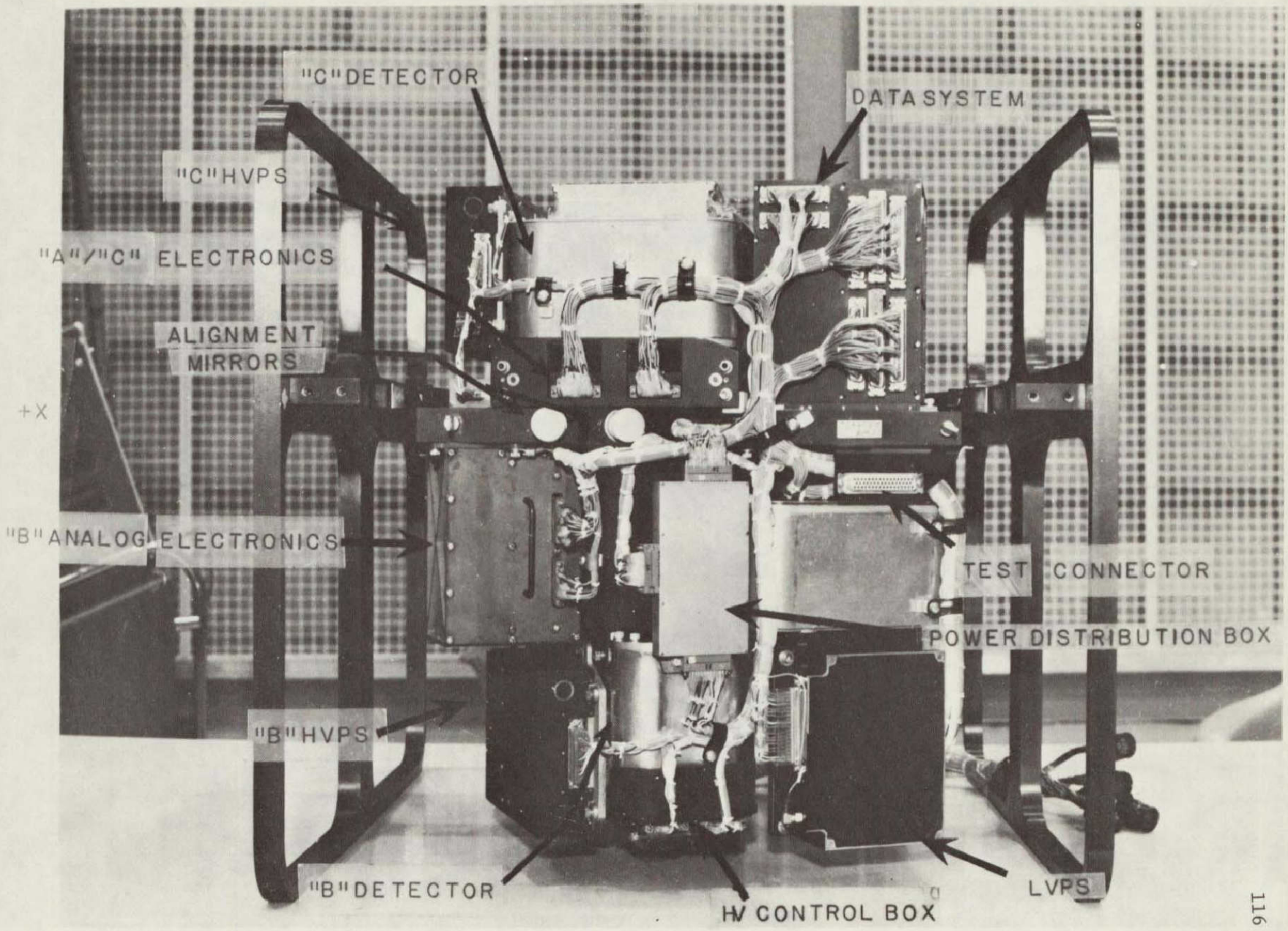


Figure 2-1 VIEW LOOKING INBOARD

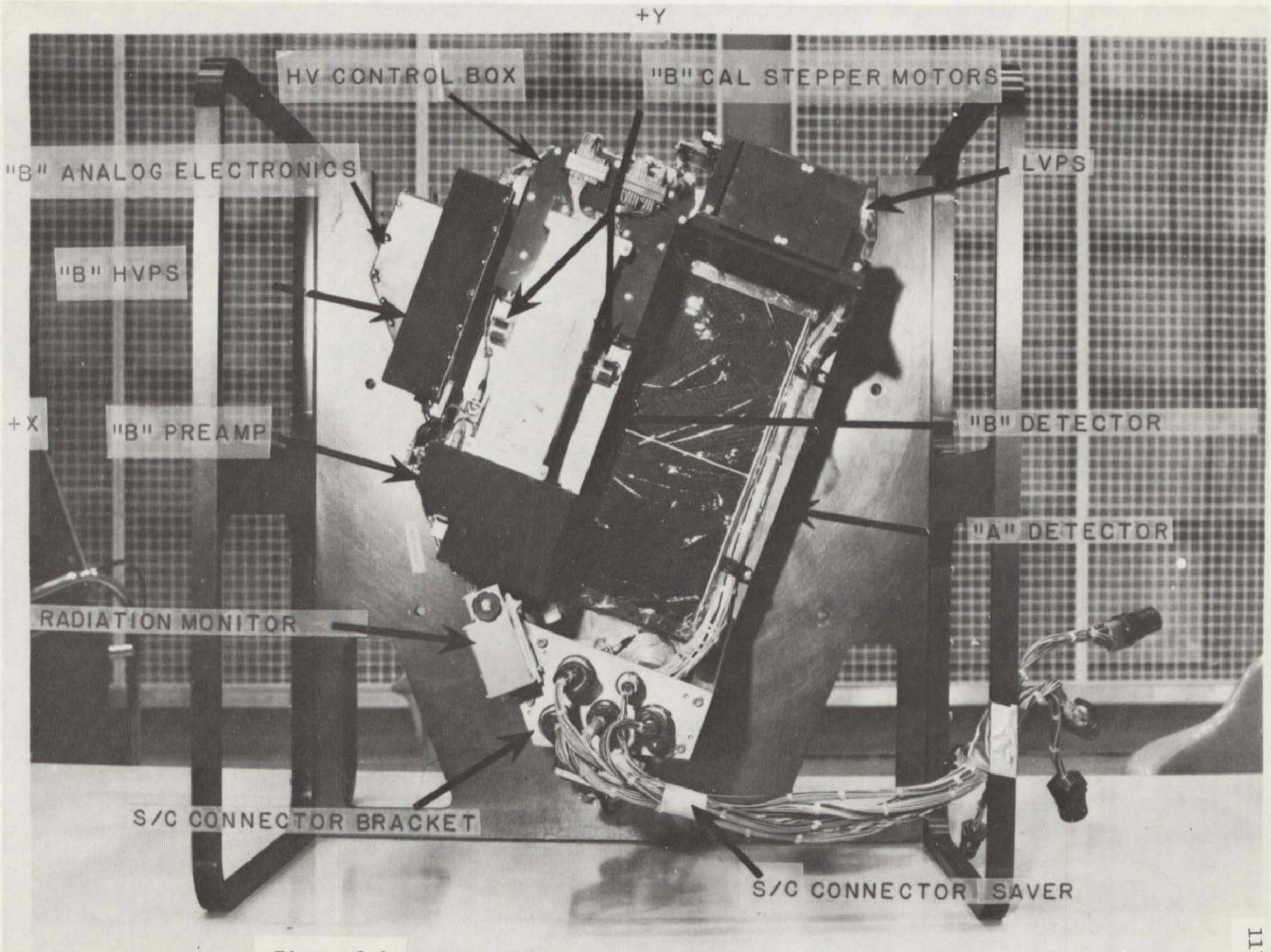


Figure 2-2 VIEW LOOKING FORWARD AT AFT SIDE OF SHELF

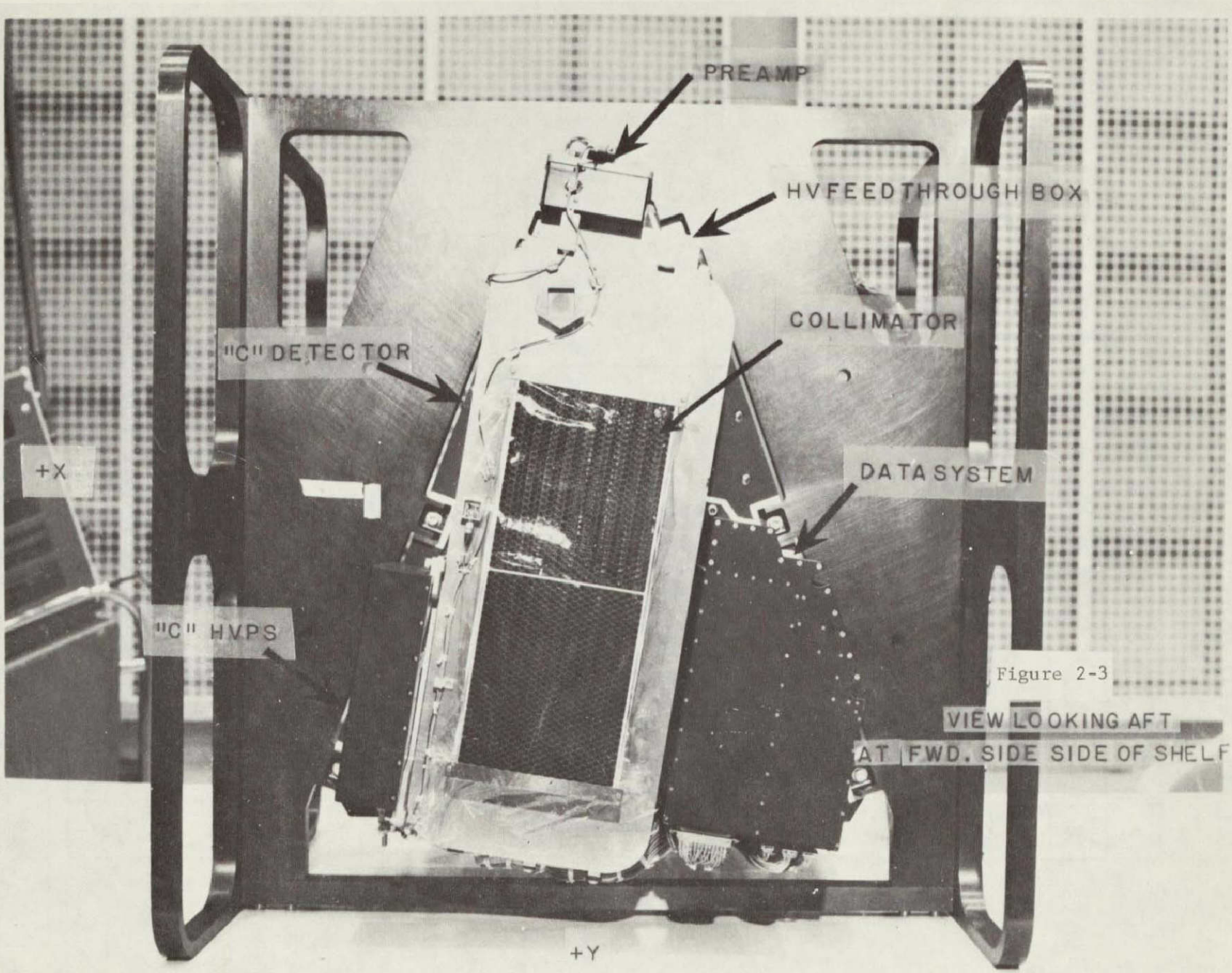


Figure 2-3

VIEW LOOKING AFT AT FWD. SIDE SIDE OF SHELF

# SIGNAL HANDLING OF OSO-I DETECTORS

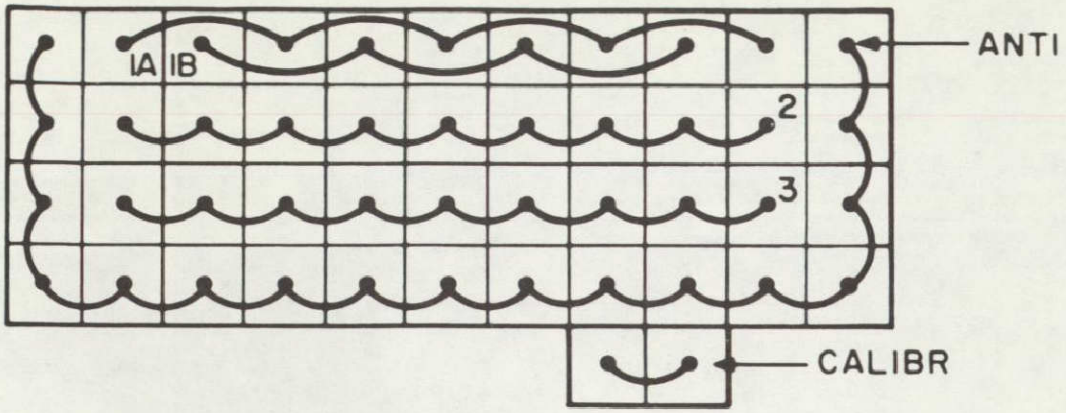


DET A

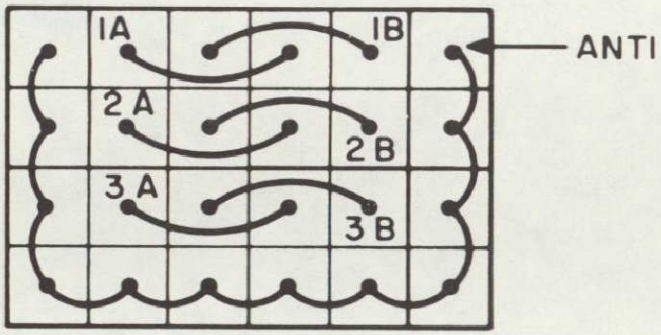


DET B

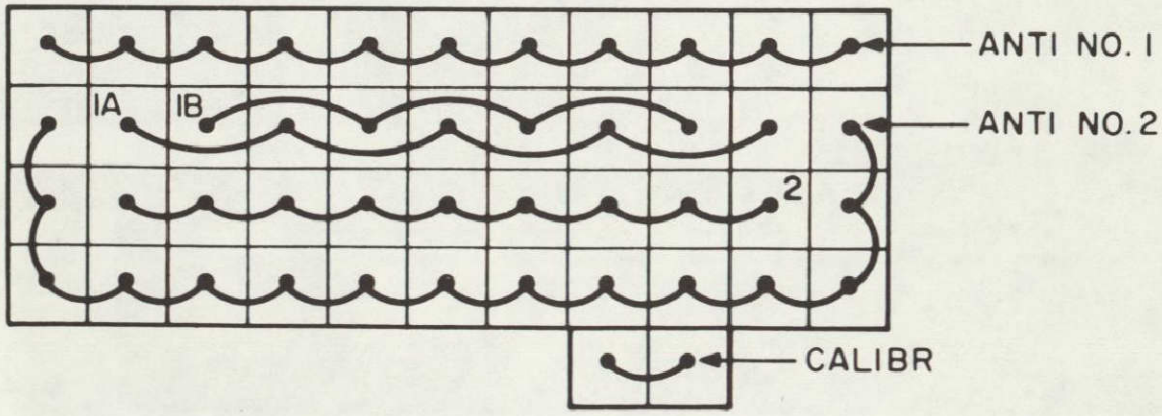


DET C

Figure 2-4

REPRODUCIBILITY OF THE
ORIGINAL PAGE IS POOR

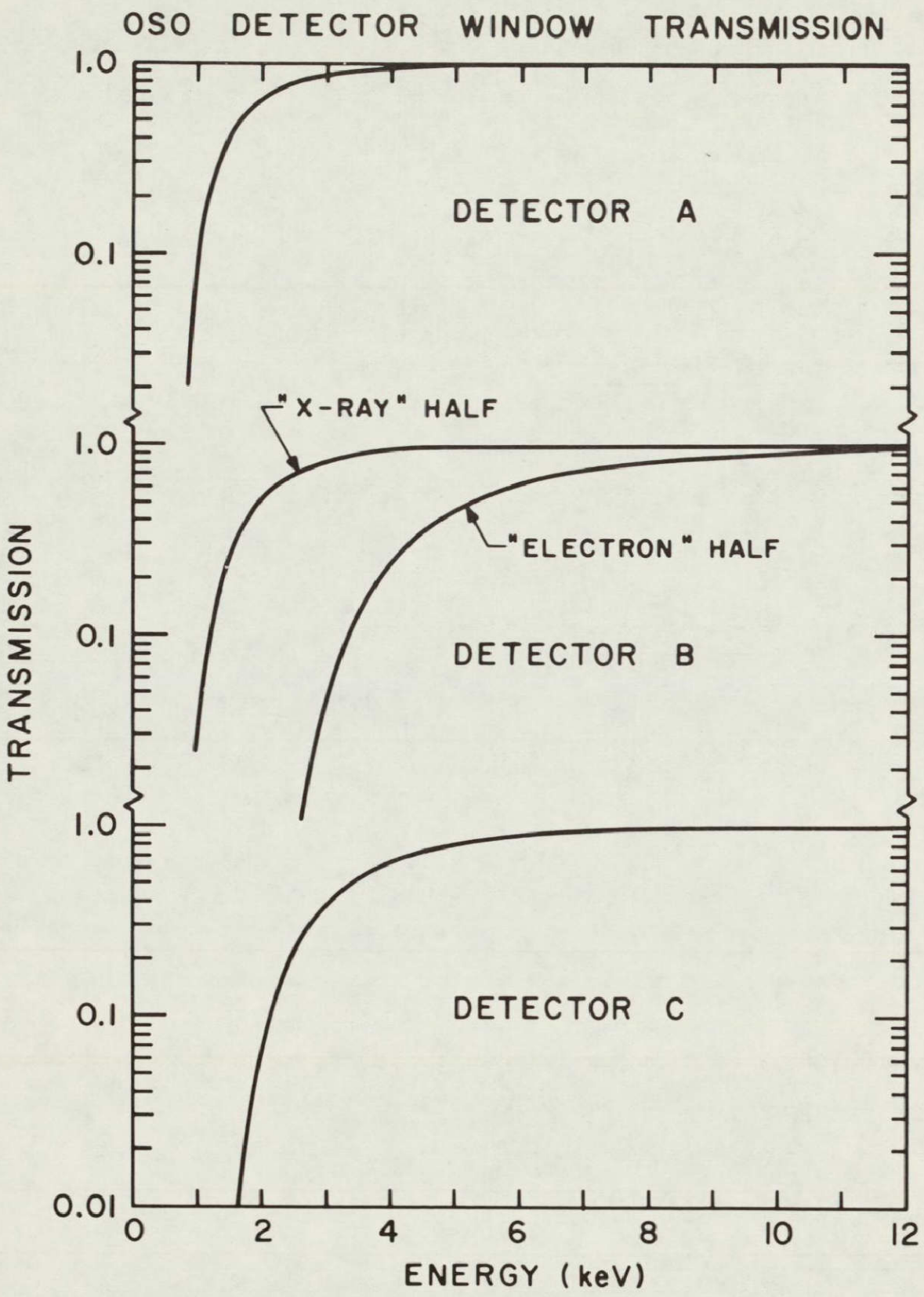
OSO DETECTOR WINDOW TRANSMISSION
1.0
0.1
DETECTOR A
"X-RAY" HALF
1.0
"ELECTRON" HALF
0.1
DETECTOR B
TRANSMISSION
1.0
0.1
DETECTOR C
0.01
0
2
4
6
8
10
12
ENERGY (keV)

Figure 2-5

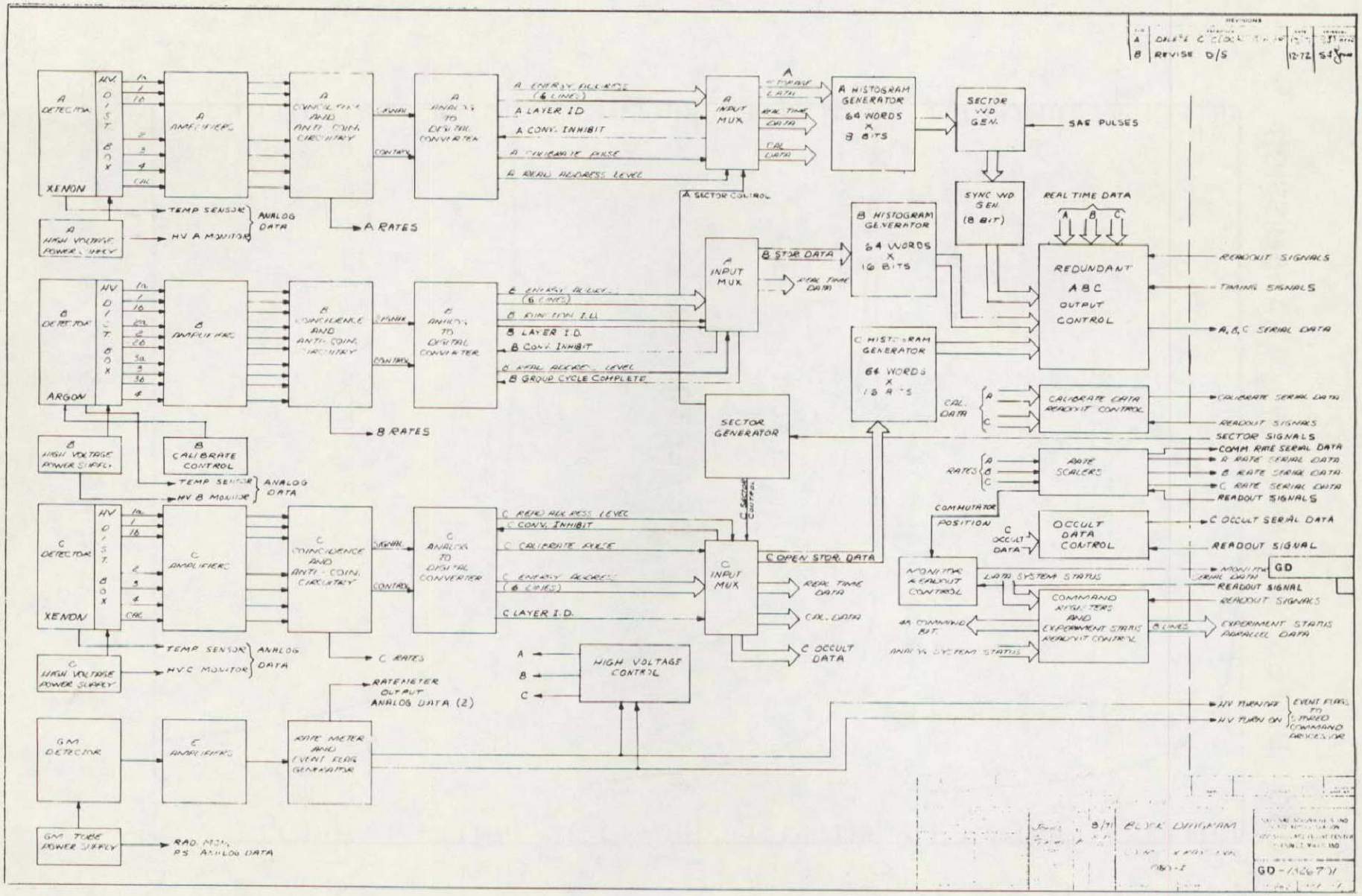


Figure 2-6 BLOCK DIAGRAM OF EXPERIMENT

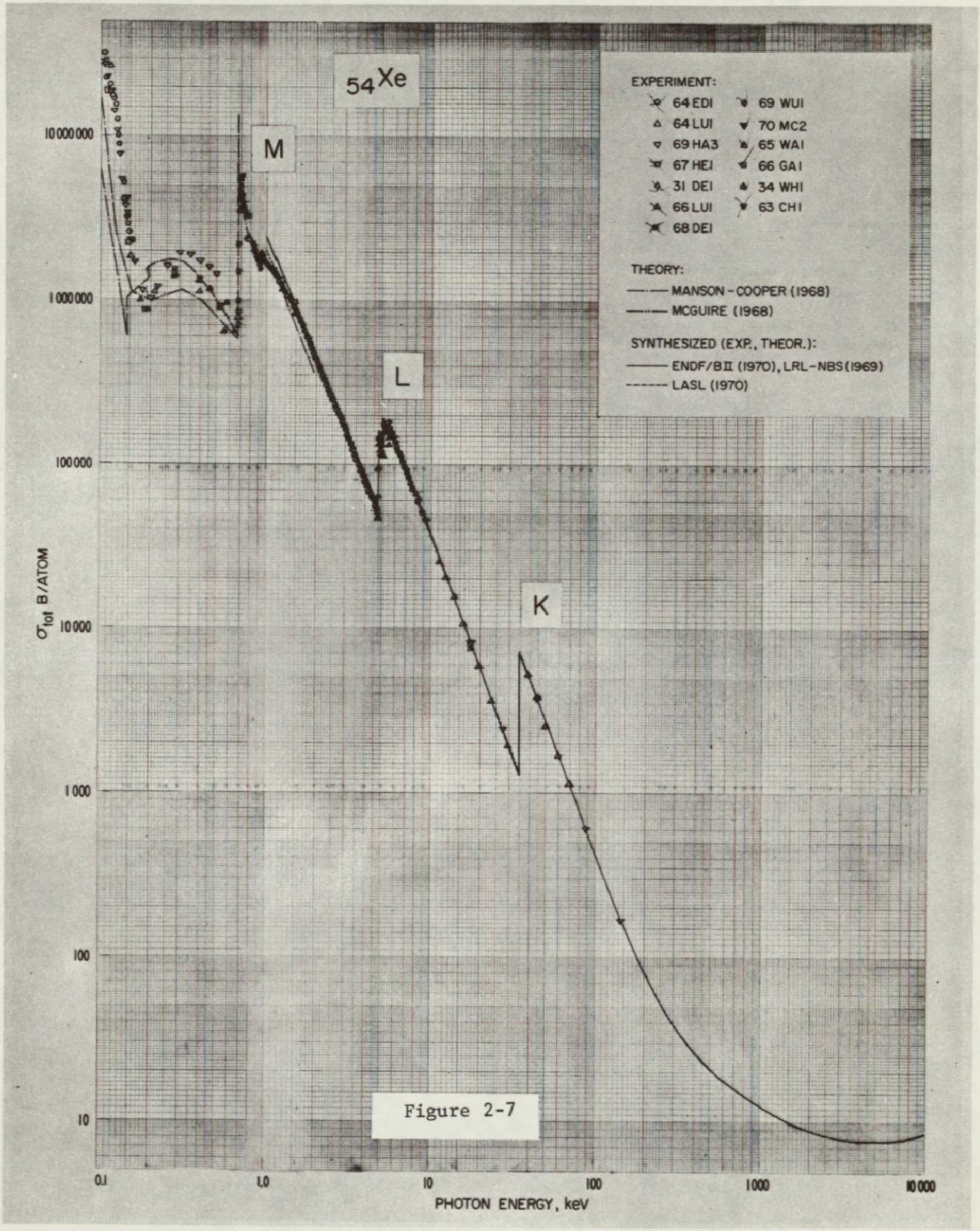
54Xe
M
L
K
EXPERIMENT:
64 EDI
64 LUI
69 HA3
67 HEI
31 DEI
66 LUI
68 DEI
69 WUI
70 MC2
65 WAI
66 GAI
34 WHI
63 CHI
THEORY:
MANSON - COOPER (1968)
MCGUIRE (1968)
SYNTHESIZED (EXP., THEOR.):
ENDF/BII (1970), LRL-NBS(1969)
LASL (1970)
10000000
1000000
100000
10000
1000
100
10
σtot B/ATOM
0.1
1.0
10
100
1000
10000
PHOTON ENERGY, keV

Figure 2-7

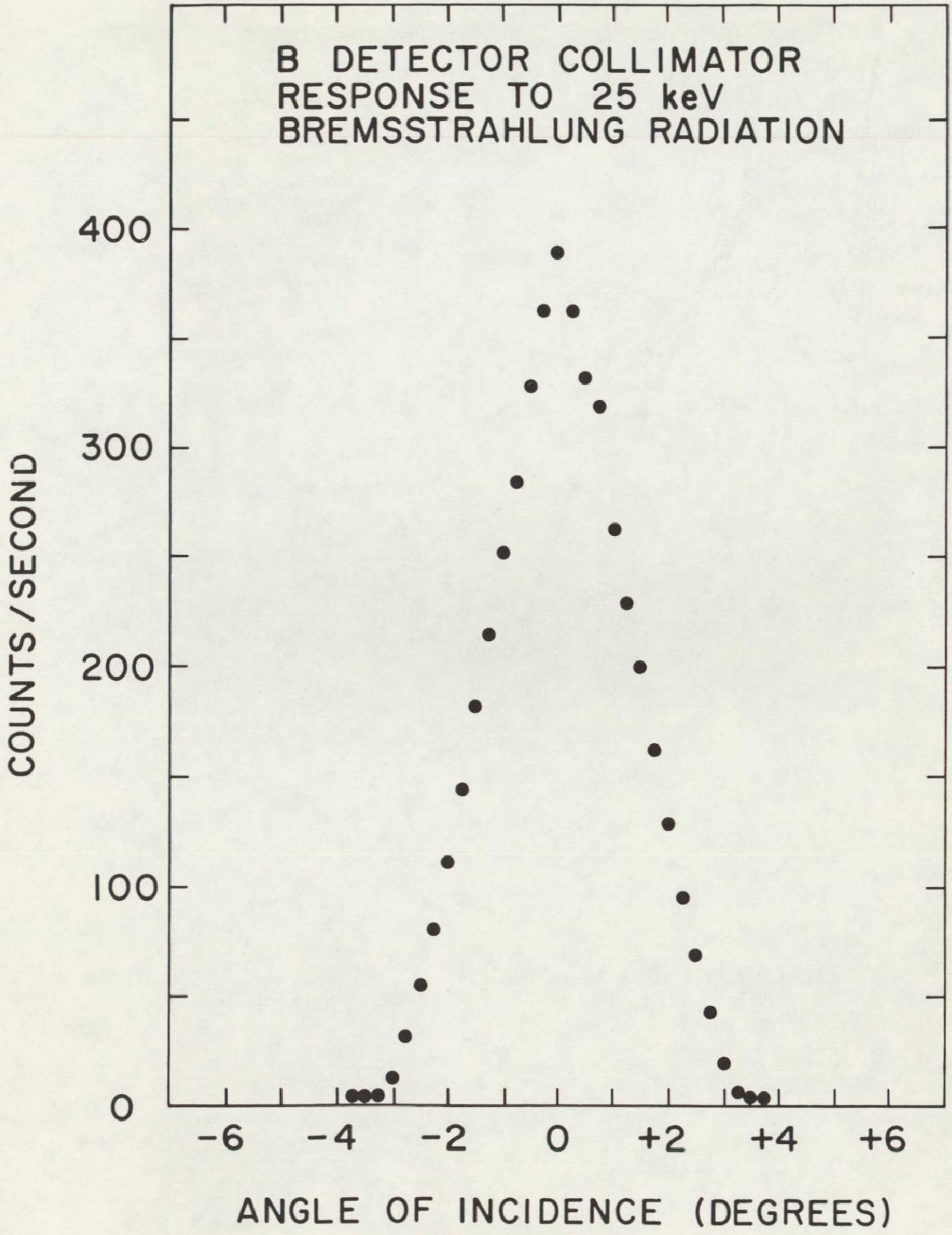
B DETECTOR COLLIMATOR
RESPONSE TO 25 keV
BREMSSTRAHLUNG RADIATION
COUNTS/SECOND
400
300
200
100
0
-6
-4
-2
0
+2
+4
+6
ANGLE OF INCIDENCE (DEGREES)

Figure 2-8

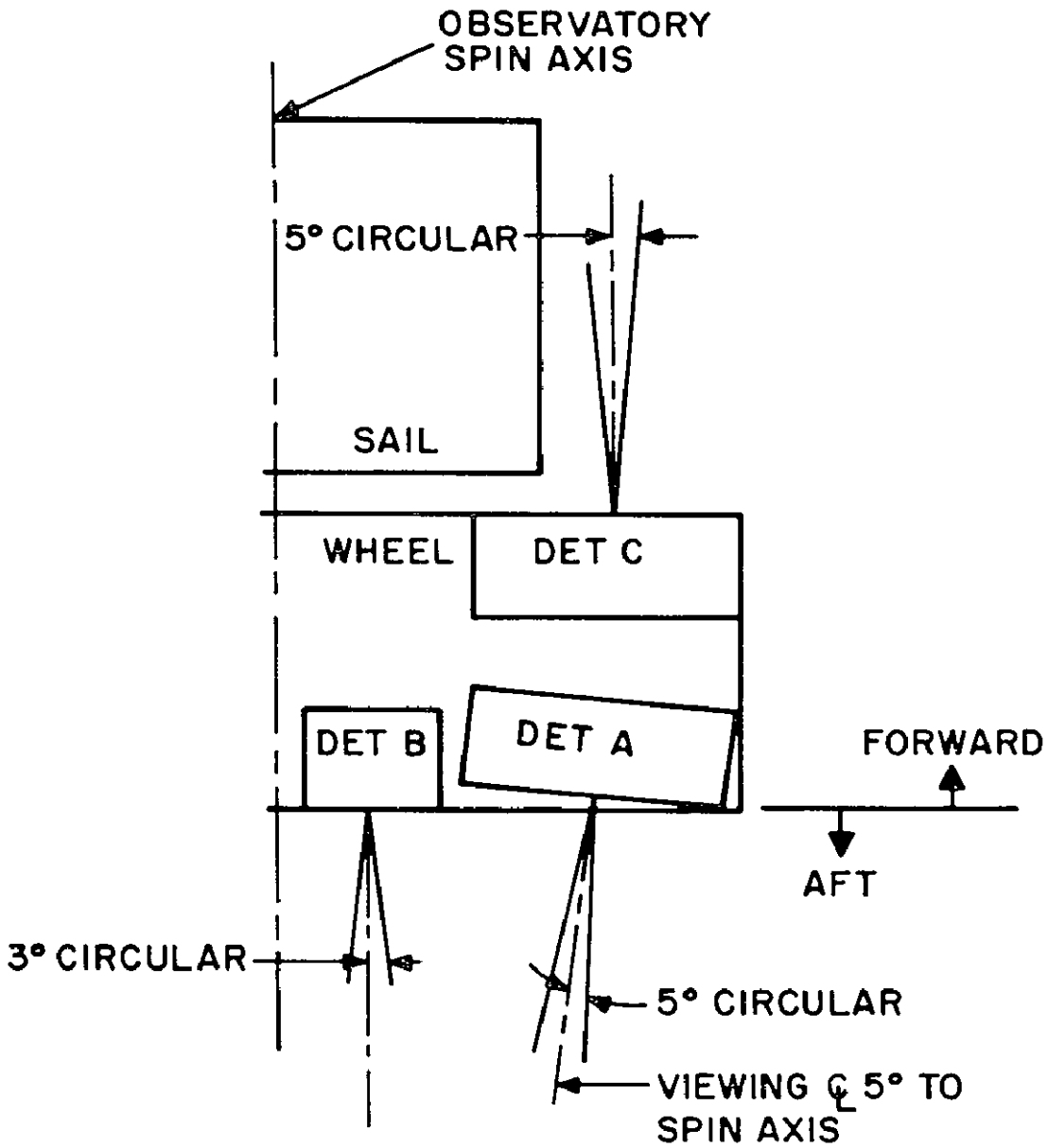


ARRANGEMENT OF COSMIC X-RAY EXPERIMENT

Figure 2-9

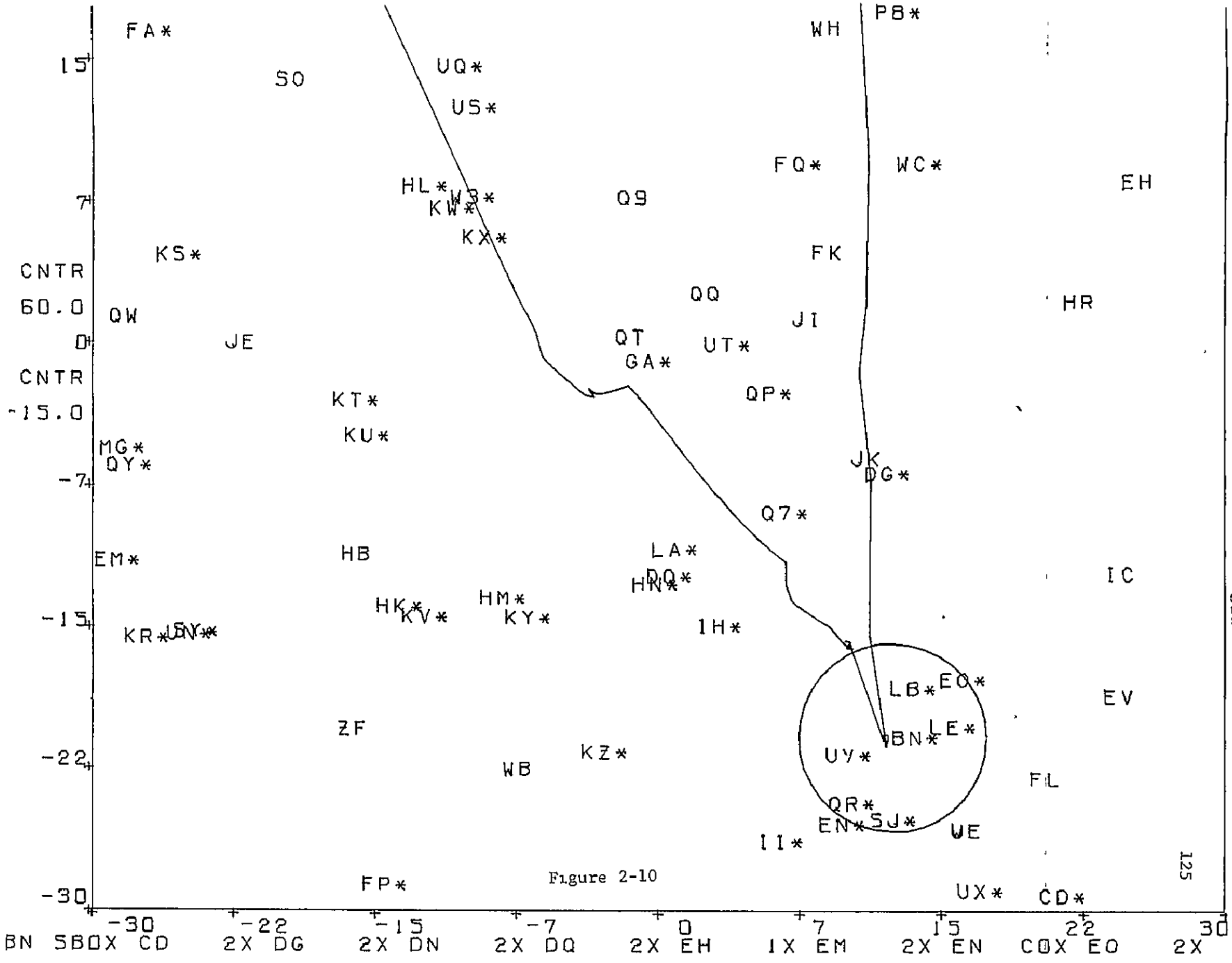


Figure 2-10

REPRODUCIBILITY OF THE ORIGINAL PAGE IS POOR

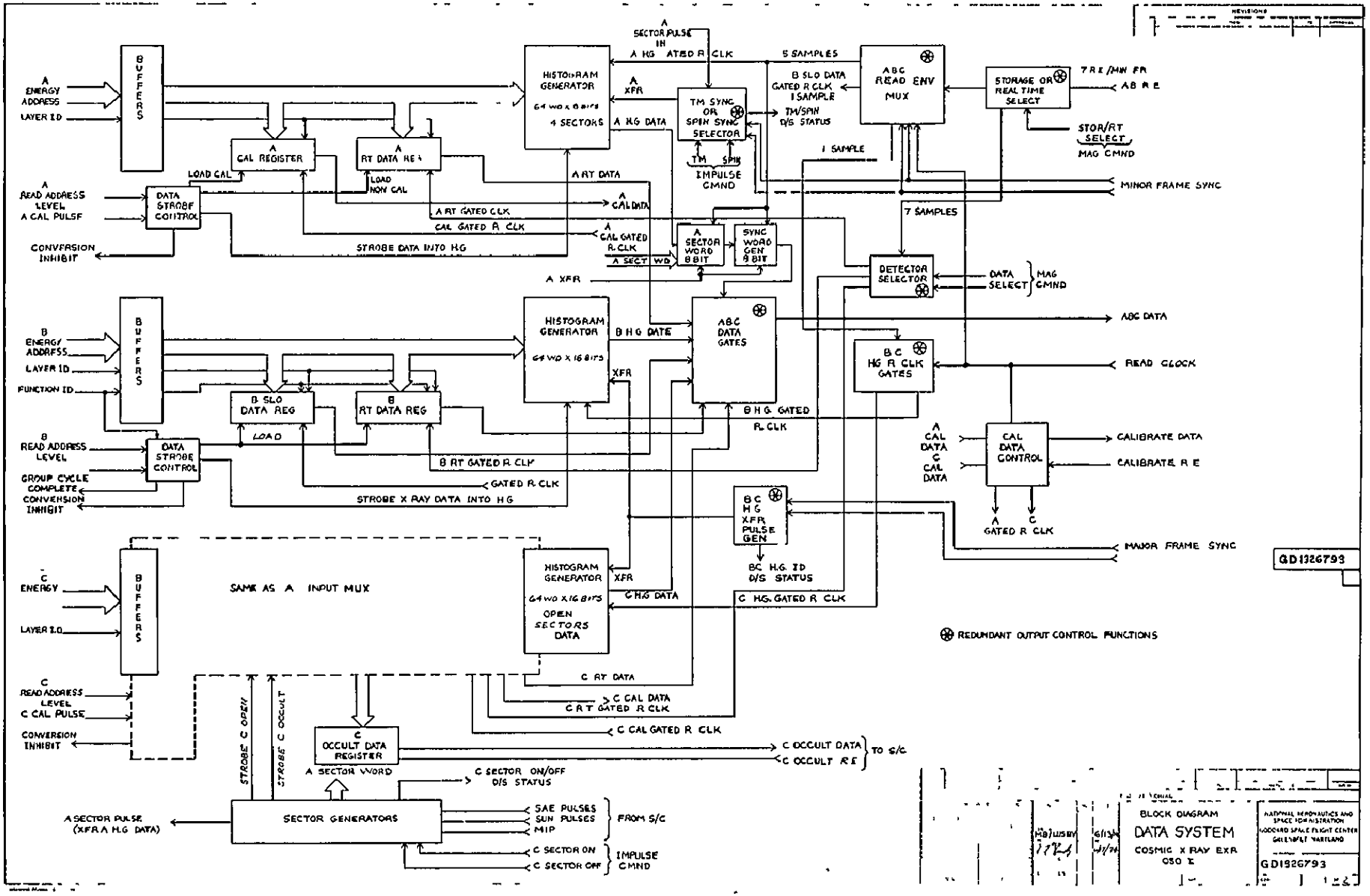


Figure 2-11 DATA SYSTEM, PART 1

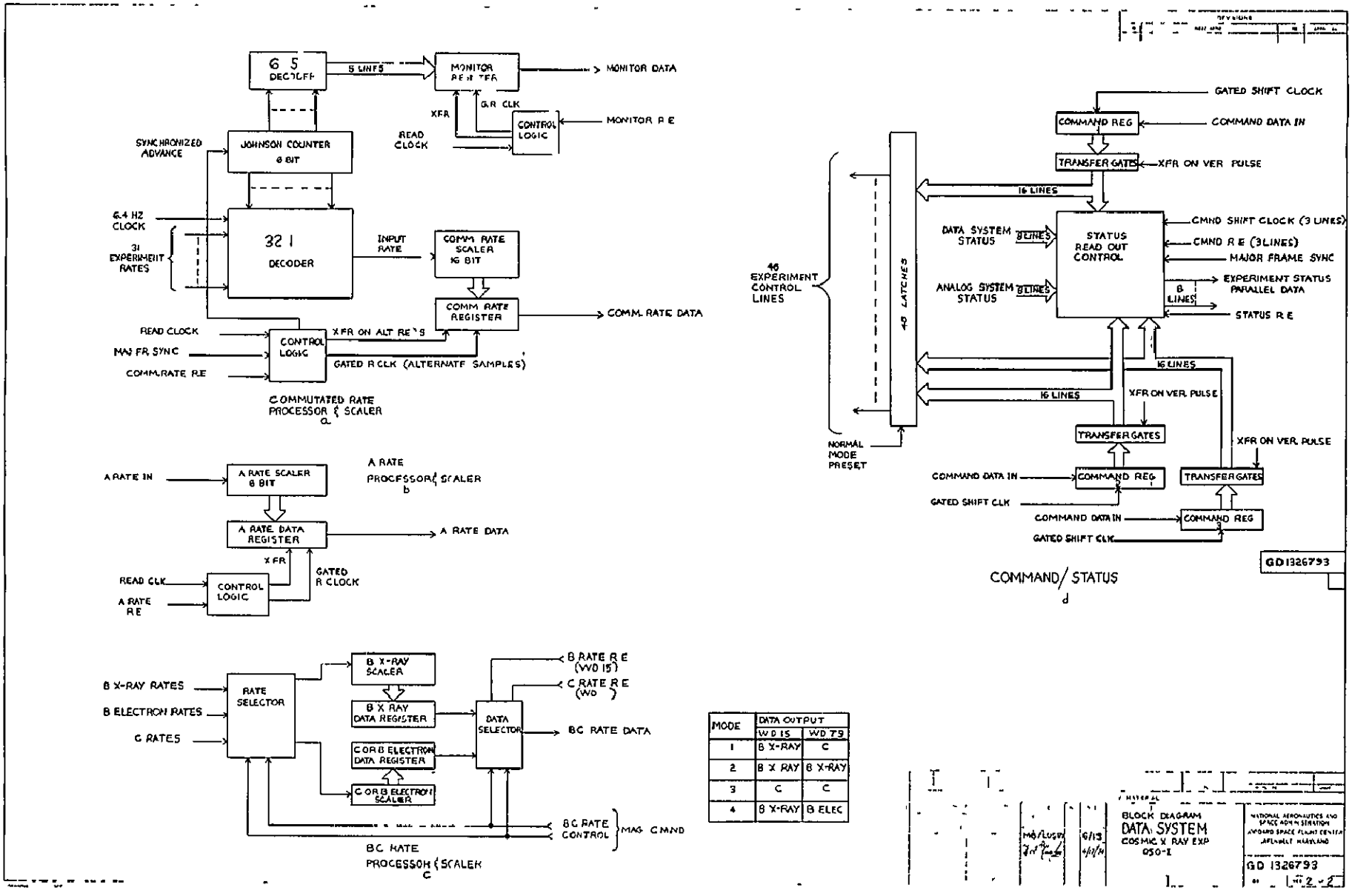


| MODE | DATA OUTPUT | |
|---|---|---|
| | WD 15 | WD 79 |
| 1 | B X-RAY | C |
| 2 | B X RAY | B X-RAY |
| 3 | C | C |
| 4 | B X-RAY | B ELEC |

Figure 2-12 DATA SYSTEM, PART 2

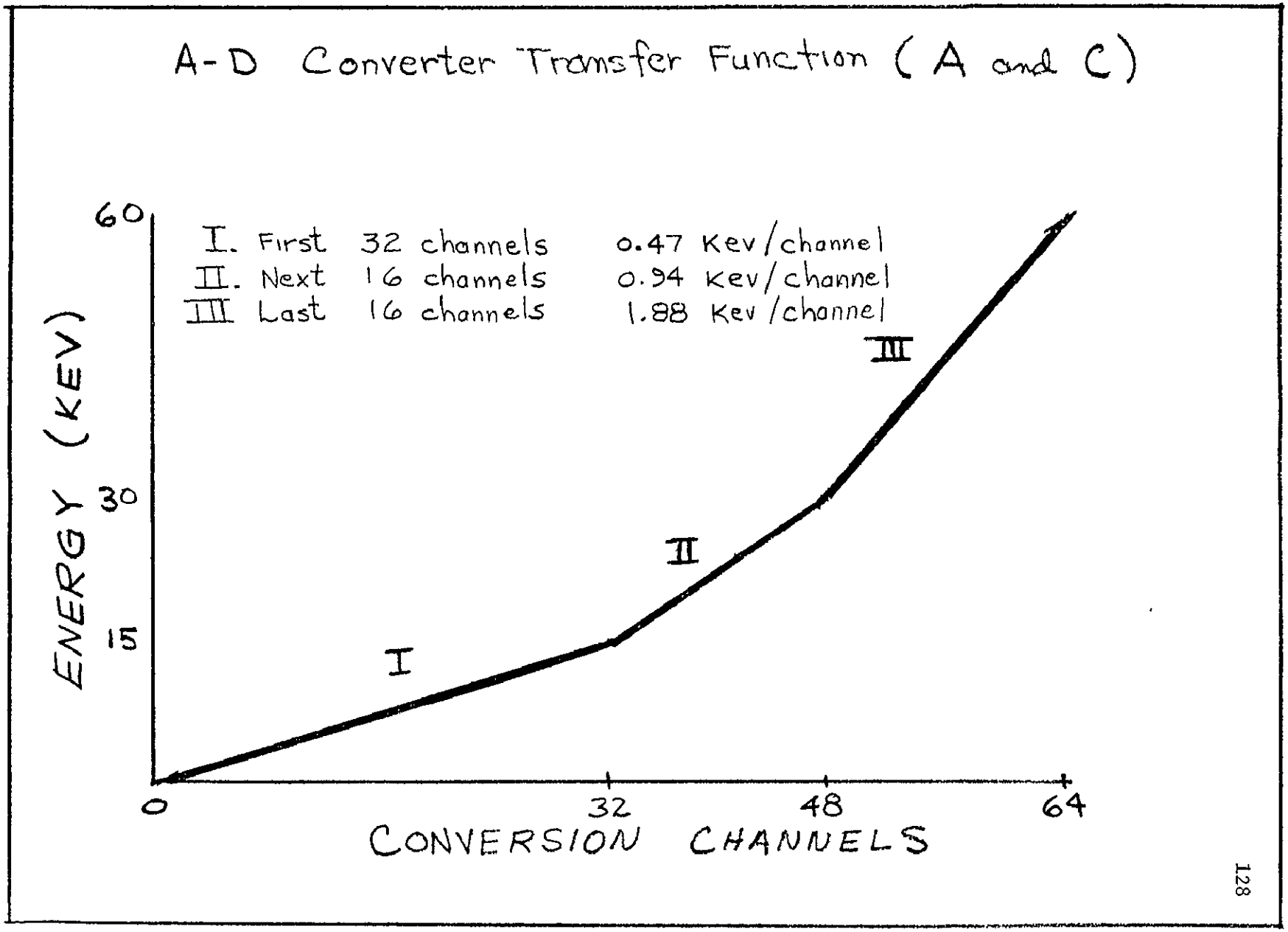
A-D Converter Transfer Function (A and C)
I. First 32 channels 0.47 Kev/channel
II. Next 16 channels 0.94 Kev/channel
III Last 16 channels 1.88 Kev/channel
60
30
15
ENERGY (KEV)
I
II
III
0
32
48
64
CONVERSION CHANNELS
128

Figure 2-13

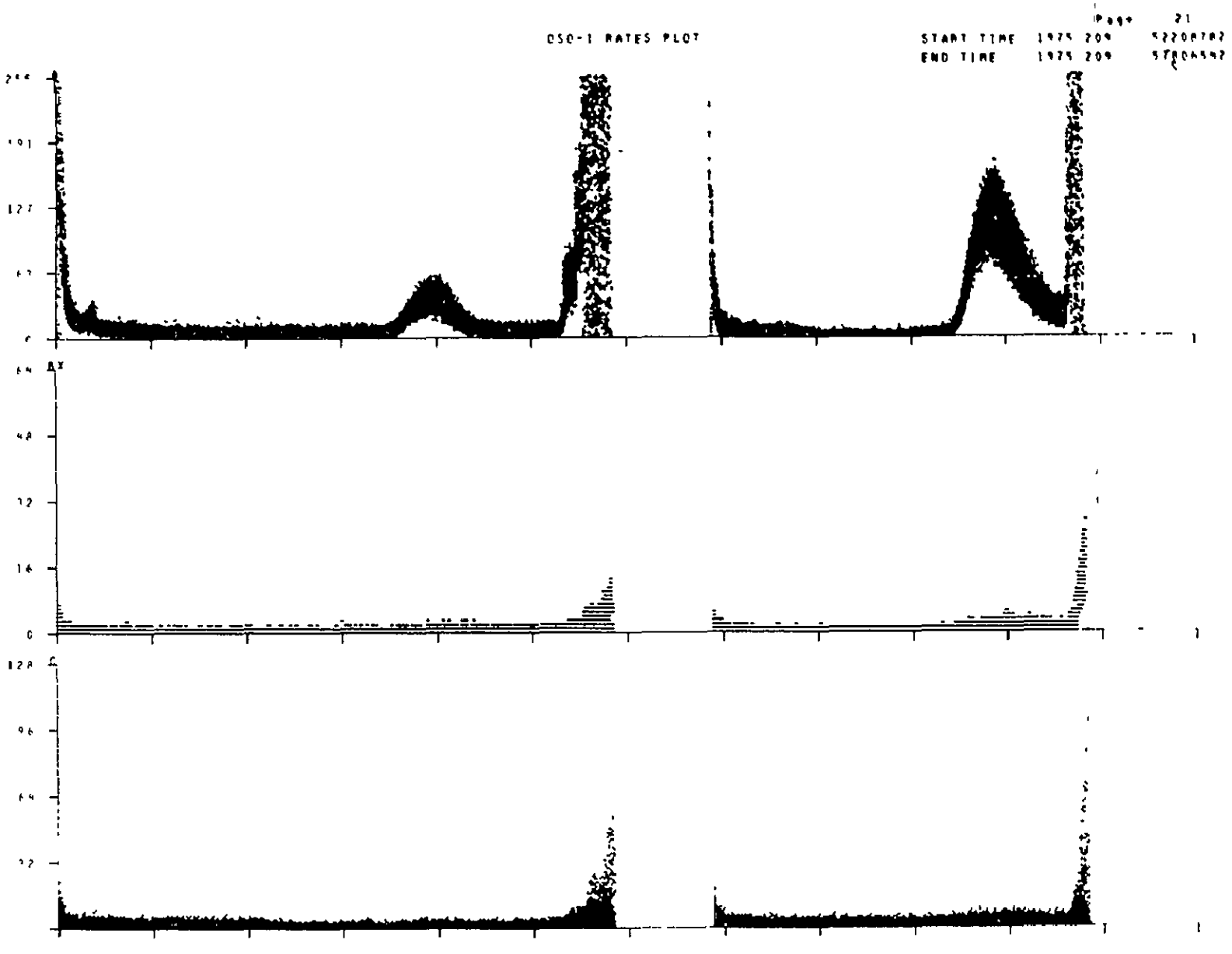


Figure 3-1

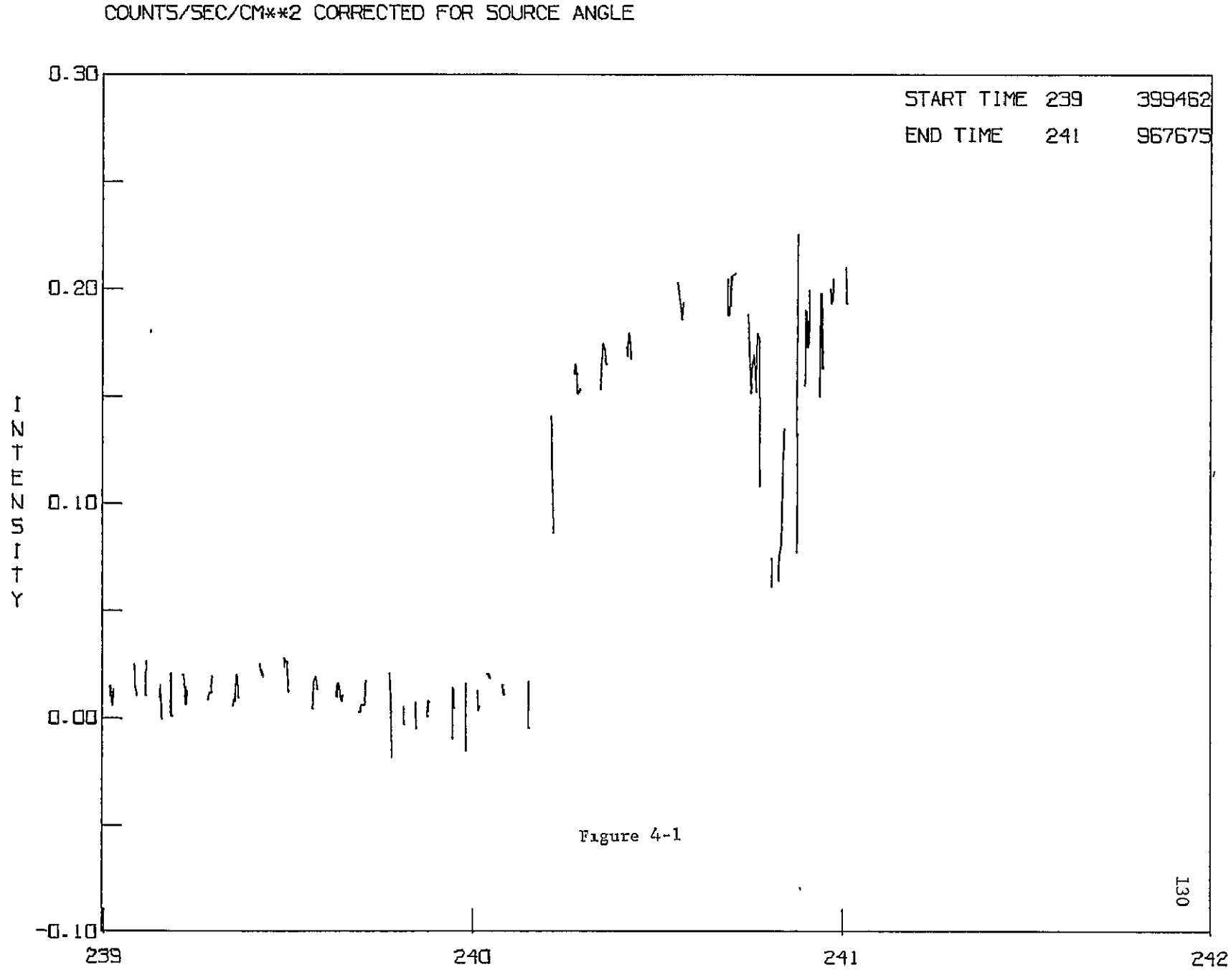
COUNTS/SEC/CM**2 CORRECTED FOR SOURCE ANGLE
START TIME 239 399462
END TIME 241 967675
0.30
0.20
0.10
0.00
-0.10
INTENSITY
239
240
241
242
130

Figure 4-1

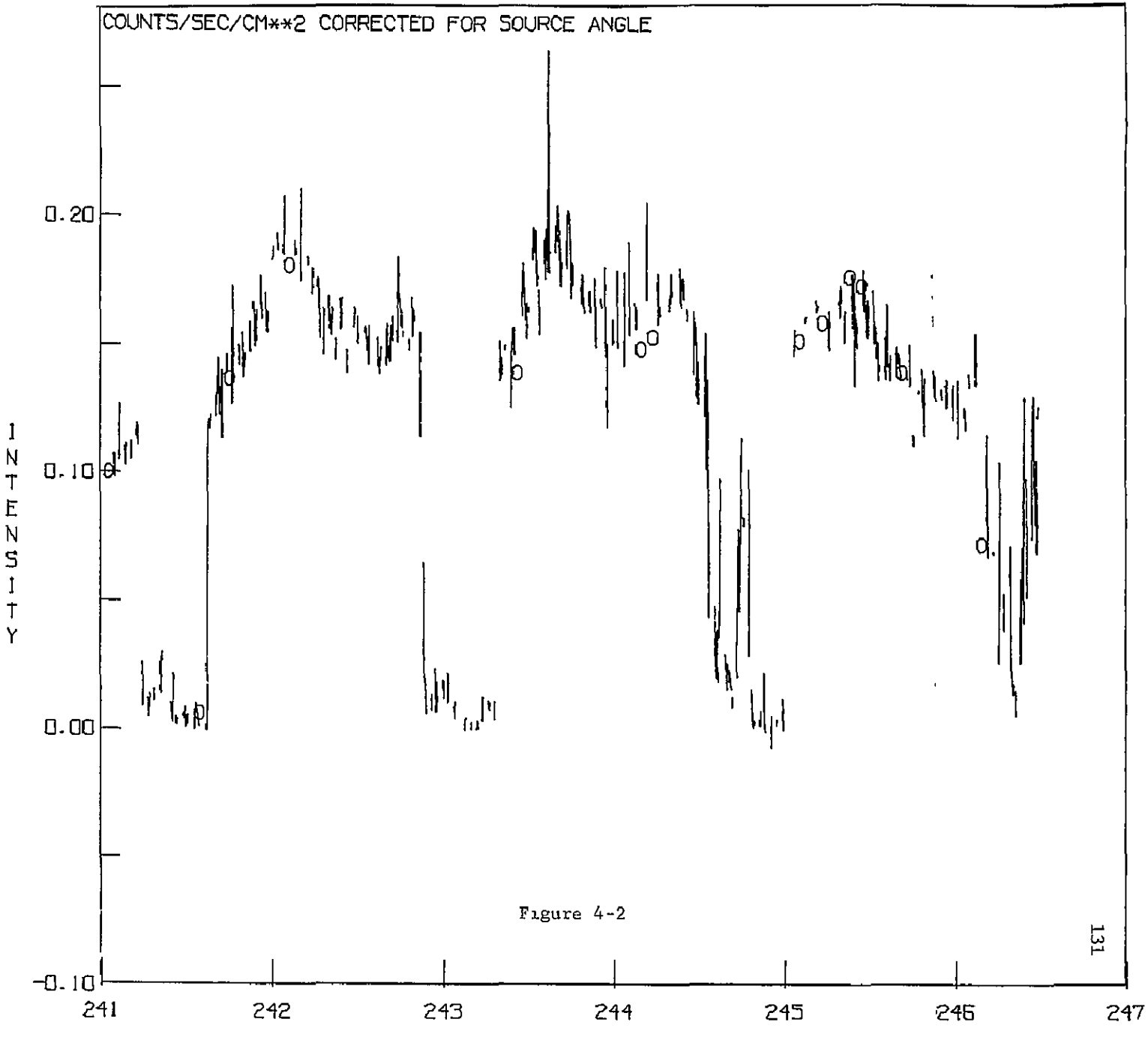
COUNTS/SEC/CM**2 CORRECTED FOR SOURCE ANGLE
INTENSITY
0.20
0.10
0.00
-0.10
241
242
243
244
245
246
247

Figure 4-2

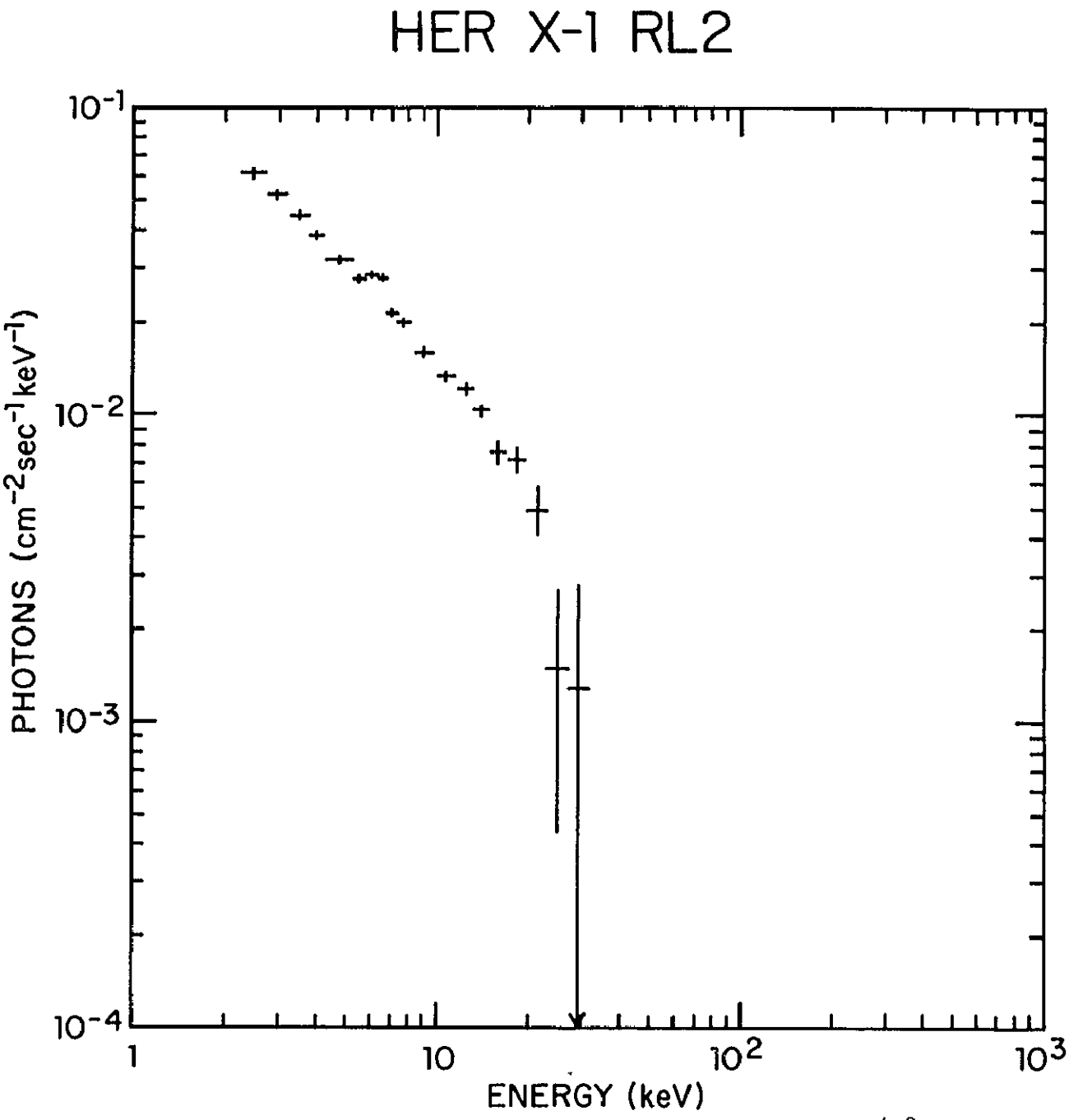
HER X-1 RL2
PHOTONS (cm$^{-2}$sec$^{-1}$keV$^{-1}$)
$10^{-1}$
$10^{-2}$
$10^{-3}$
$10^{-4}$
1
10
$10^2$
$10^3$
ENERGY (keV)

Figure 4-3

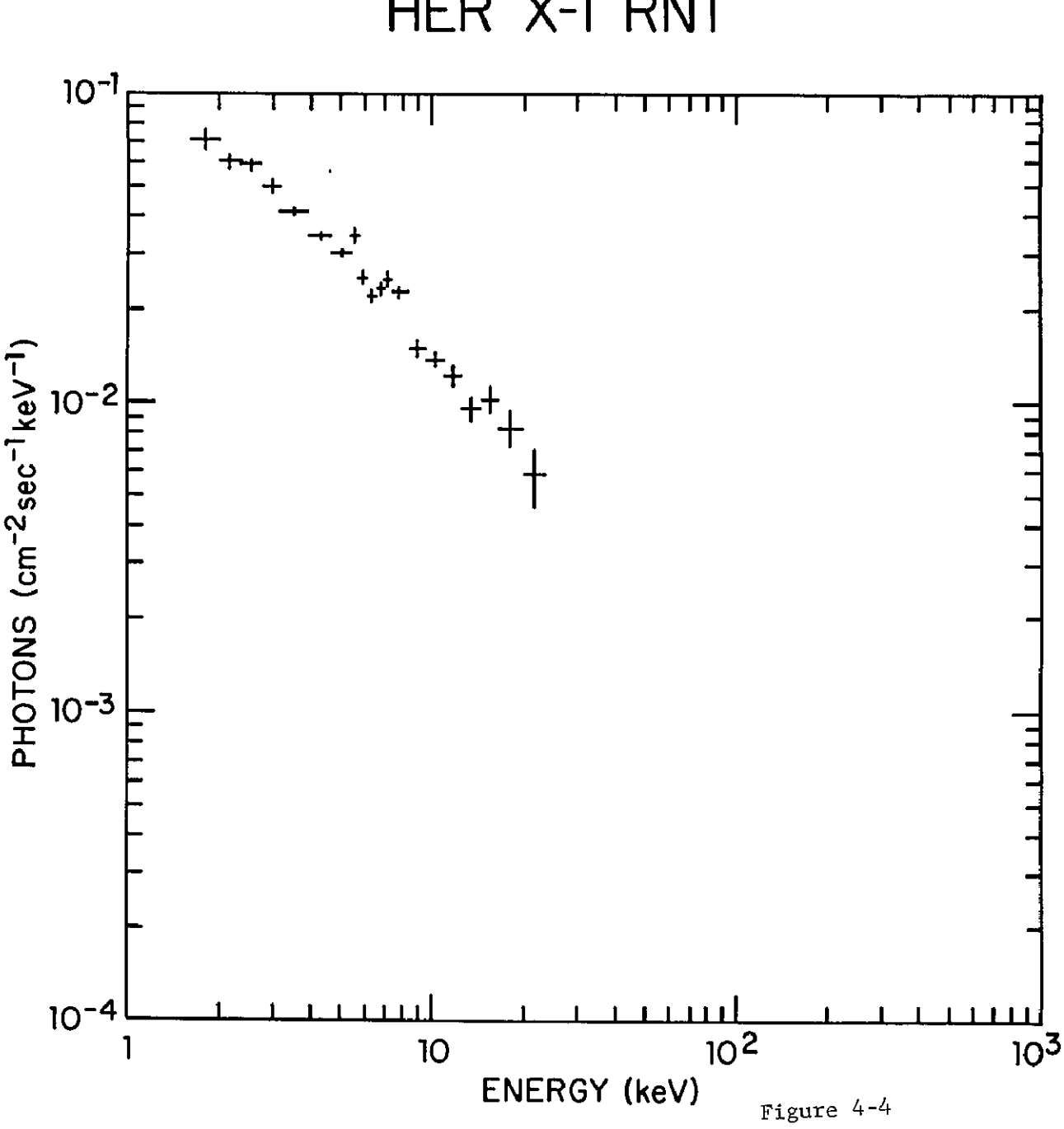
HER X-1 RN1
PHOTONS (cm$^{-2}$sec$^{-1}$keV$^{-1}$)
$10^{-1}$
$10^{-2}$
$10^{-3}$
$10^{-4}$
1
10
$10^2$
$10^3$
ENERGY (keV)

Figure 4-4

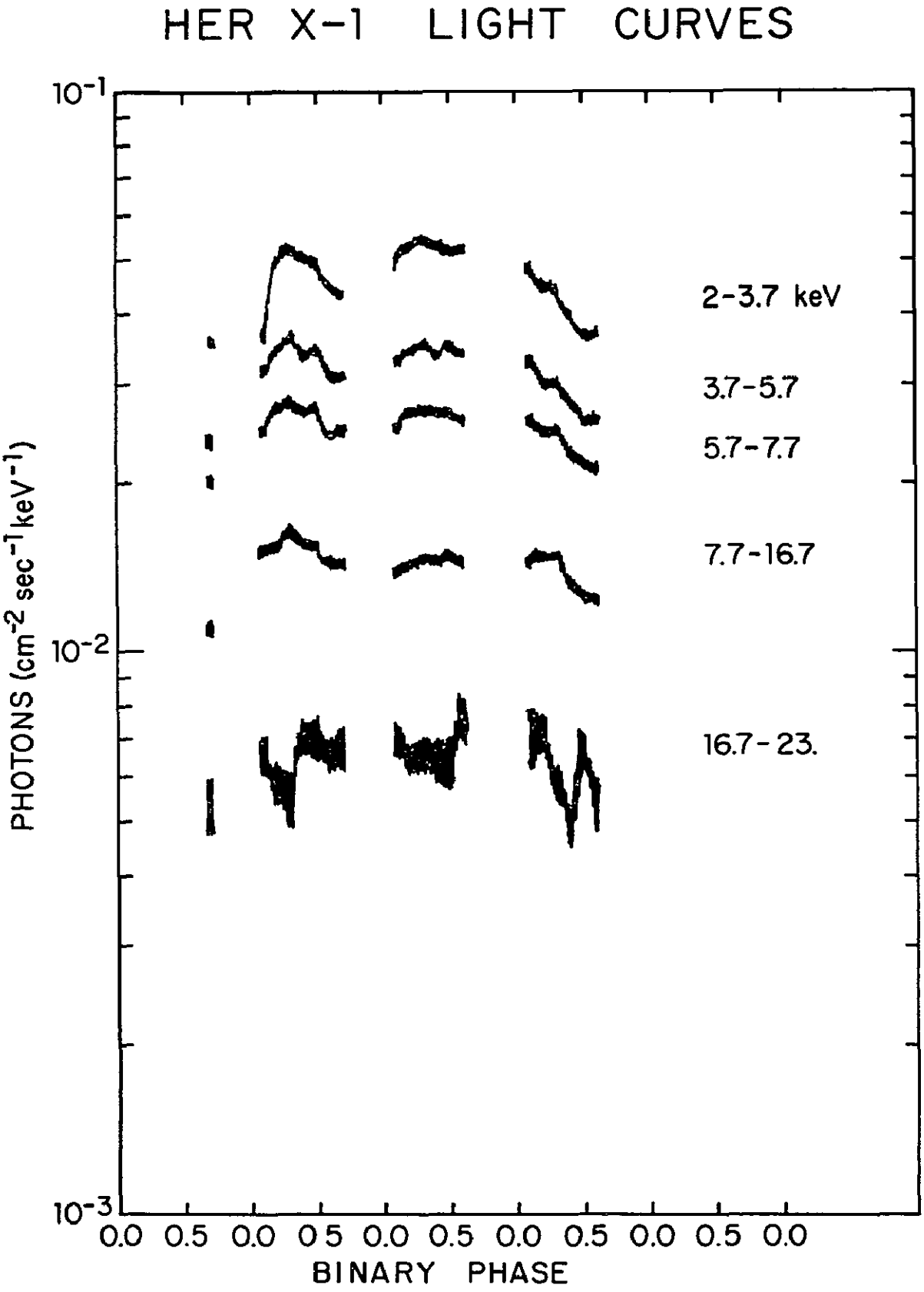
HER X-1 LIGHT CURVES
$10^{-1}$
$10^{-2}$
$10^{-3}$
PHOTONS ($cm^{-2}$ $sec^{-1}$ $keV^{-1}$)
2-3.7 keV
3.7-5.7
5.7-7.7
7.7-16.7
16.7-23.
0.0 0.5 0.0 0.5 0.0 0.5 0.0 0.5 0.0 0.5 0.0
BINARY PHASE

Figure 4-5

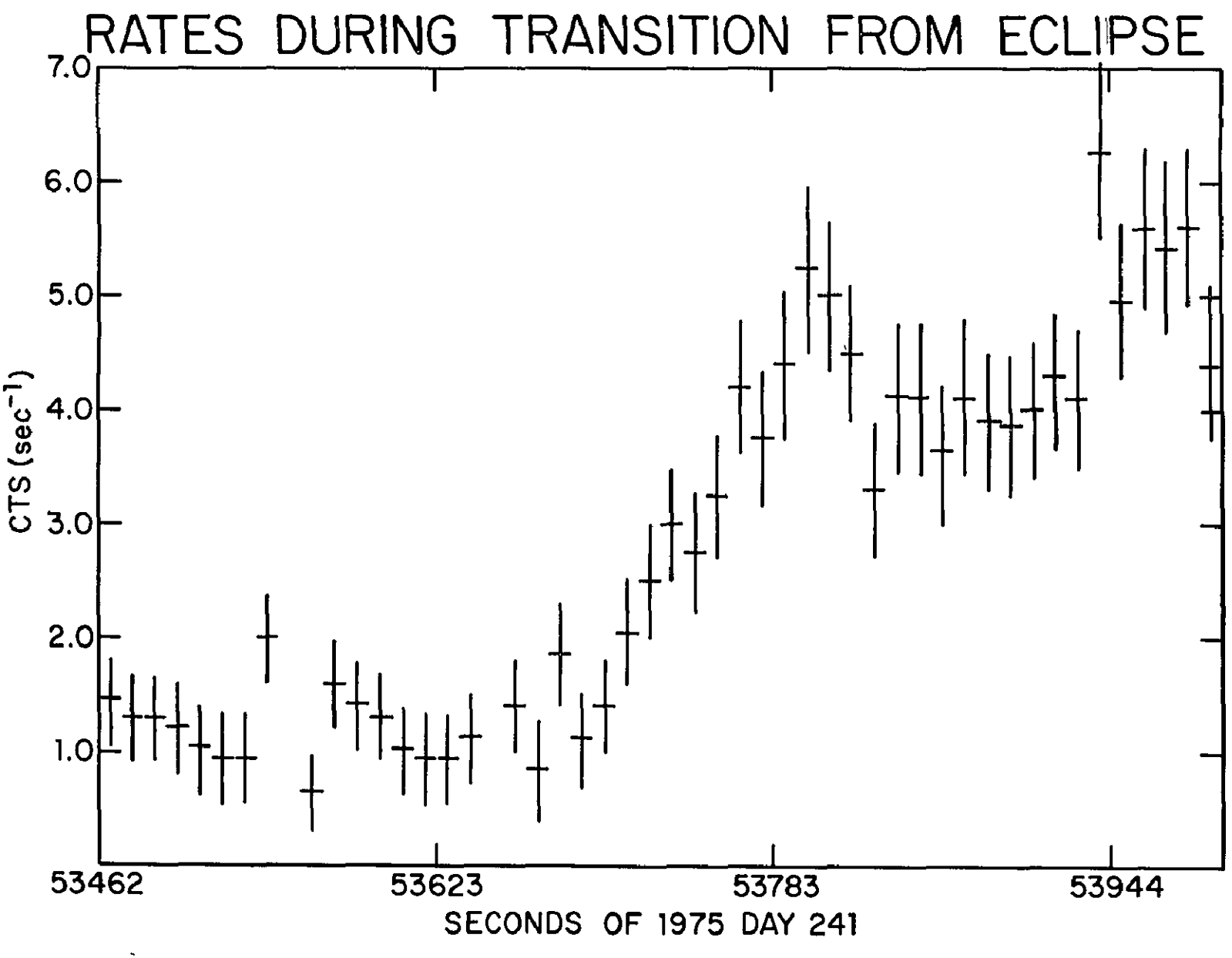
RATES DURING TRANSITION FROM ECLIPSE
7.0
6.0
5.0
4.0
3.0
2.0
1.0
CTS (sec$^{-1}$)
53462
53623
53783
53944
SECONDS OF 1975 DAY 241

Figure 4-6

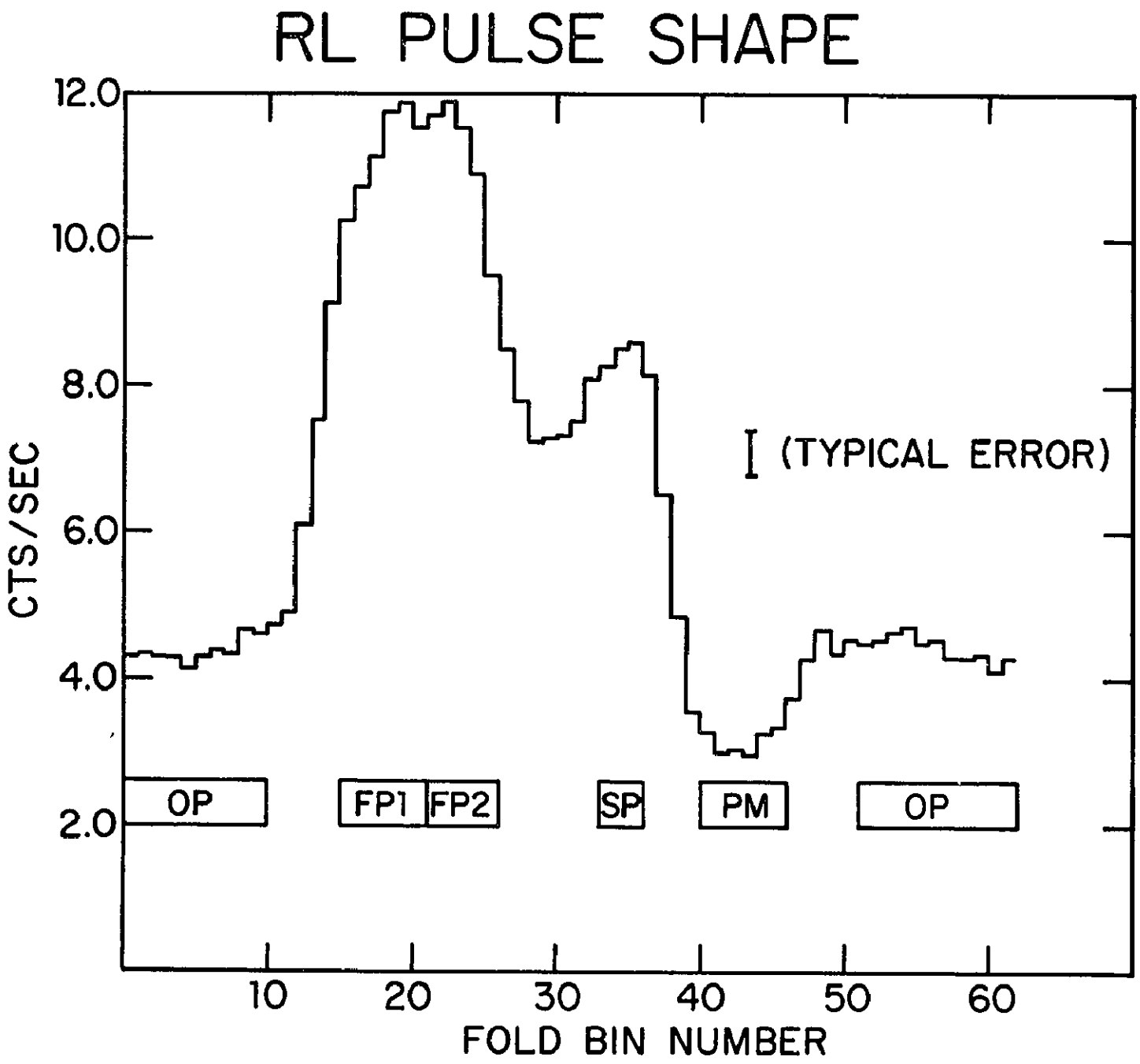
RL PULSE SHAPE
12.0
10.0
8.0
6.0
4.0
2.0
CTS/SEC
I (TYPICAL ERROR)
OP
FP1
FP2
SP
PM
OP
10
20
30
40
50
60
FOLD BIN NUMBER

Figure 4-7

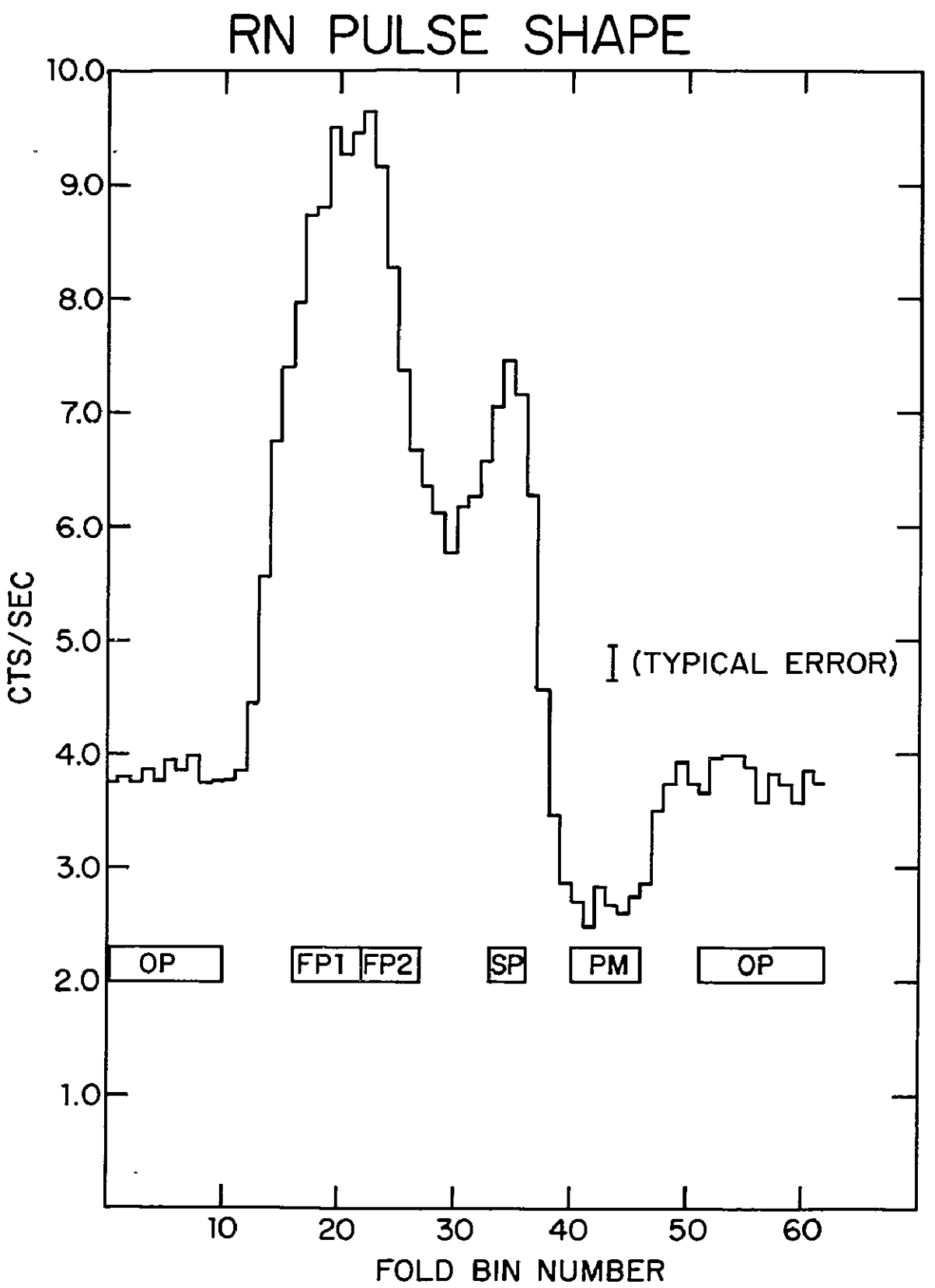
RN PULSE SHAPE
10.0
9.0
8.0
7.0
6.0
5.0
4.0
3.0
2.0
1.0
CTS/SEC
I (TYPICAL ERROR)
OP
FP1
FP2
SP
PM
OP
10
20
30
40
50
60
FOLD BIN NUMBER

Figure 4-8

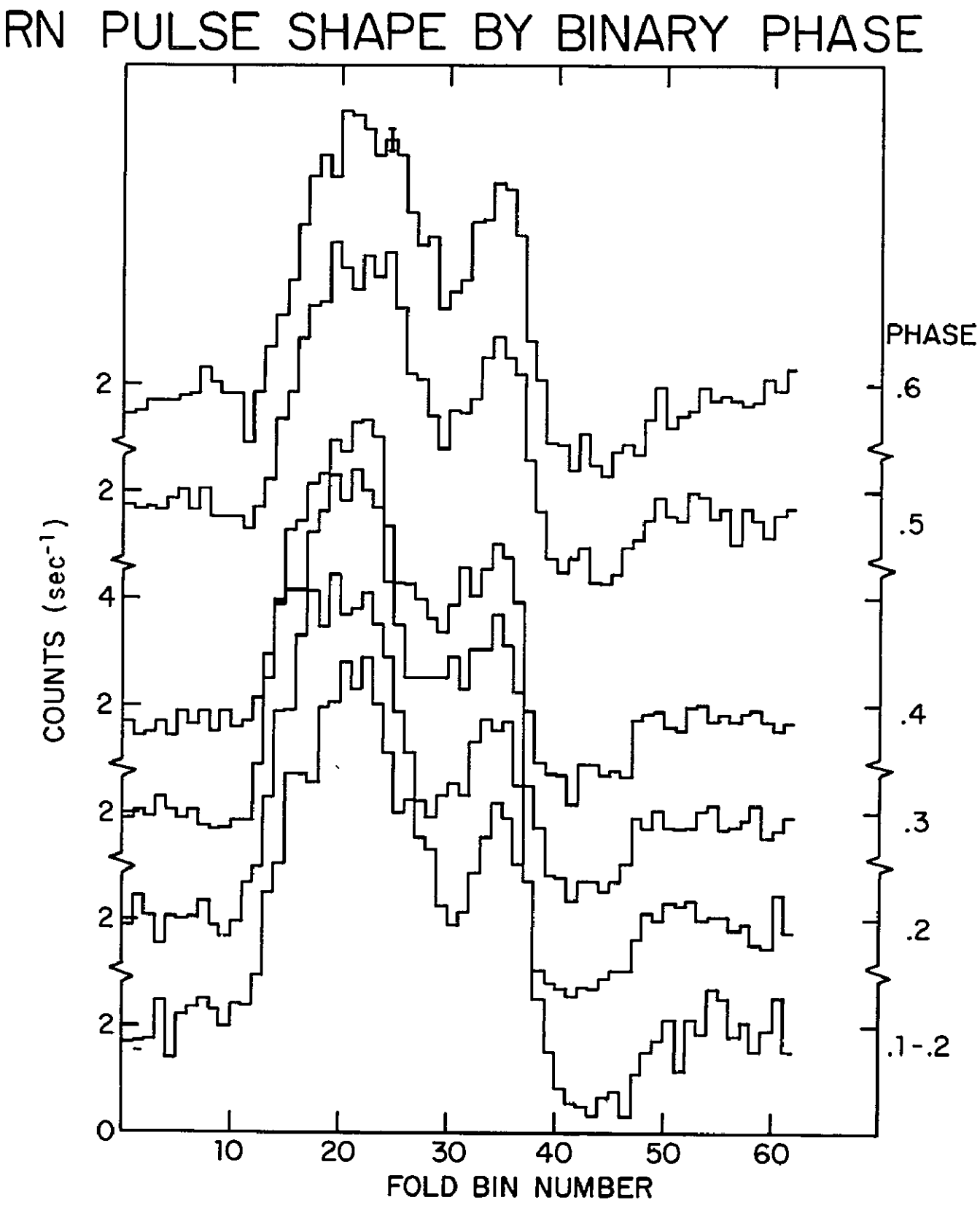
RN PULSE SHAPE BY BINARY PHASE
COUNTS (sec⁻¹)
FOLD BIN NUMBER
PHASE
.6
.5
.4
.3
.2
.1-.2
0
2
4
10
20
30
40
50
60

Figure 4-9

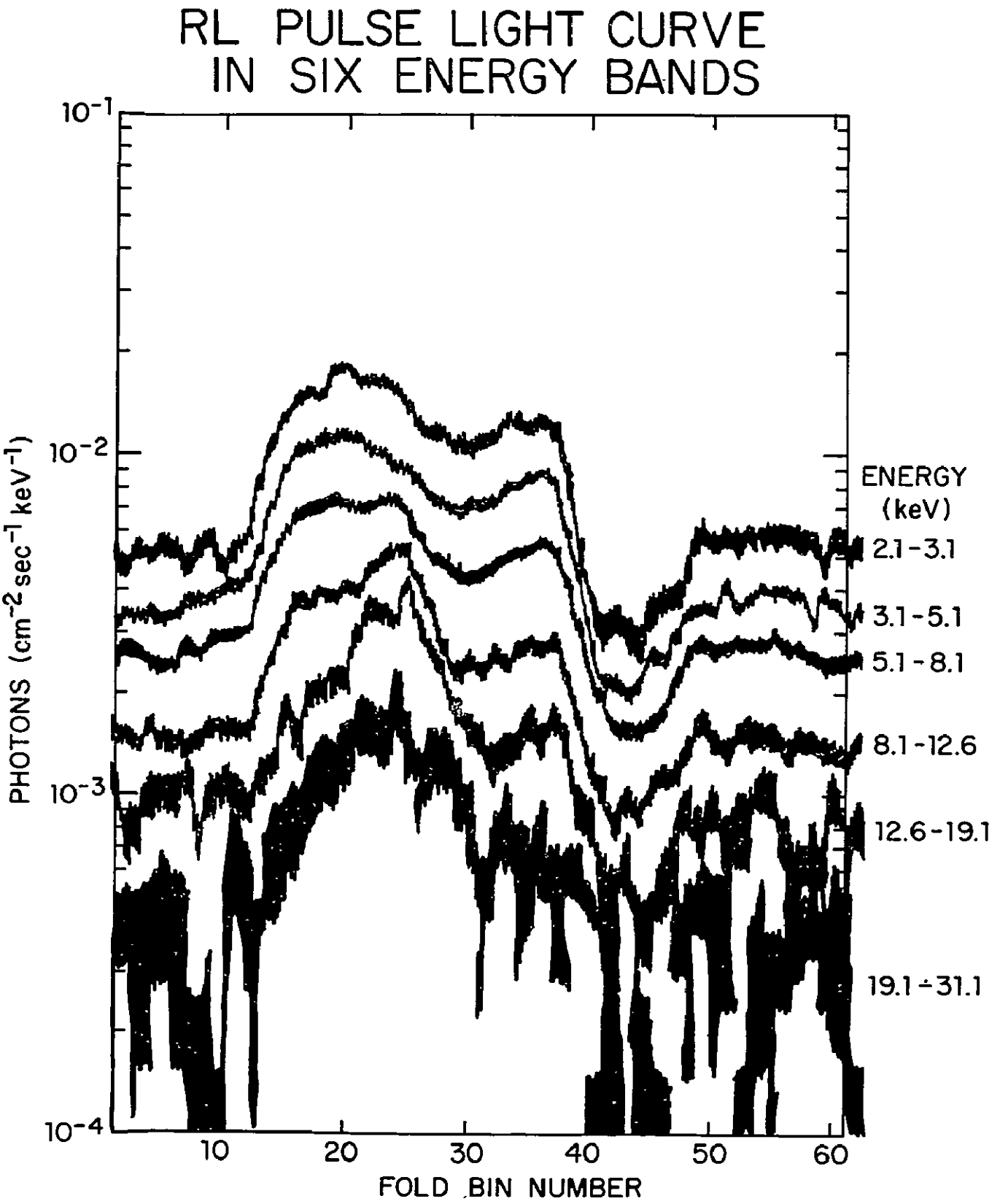


Figure 4-10

REPRODUCIBILITY OF THE
ORIGINAL PAGE IS POOR

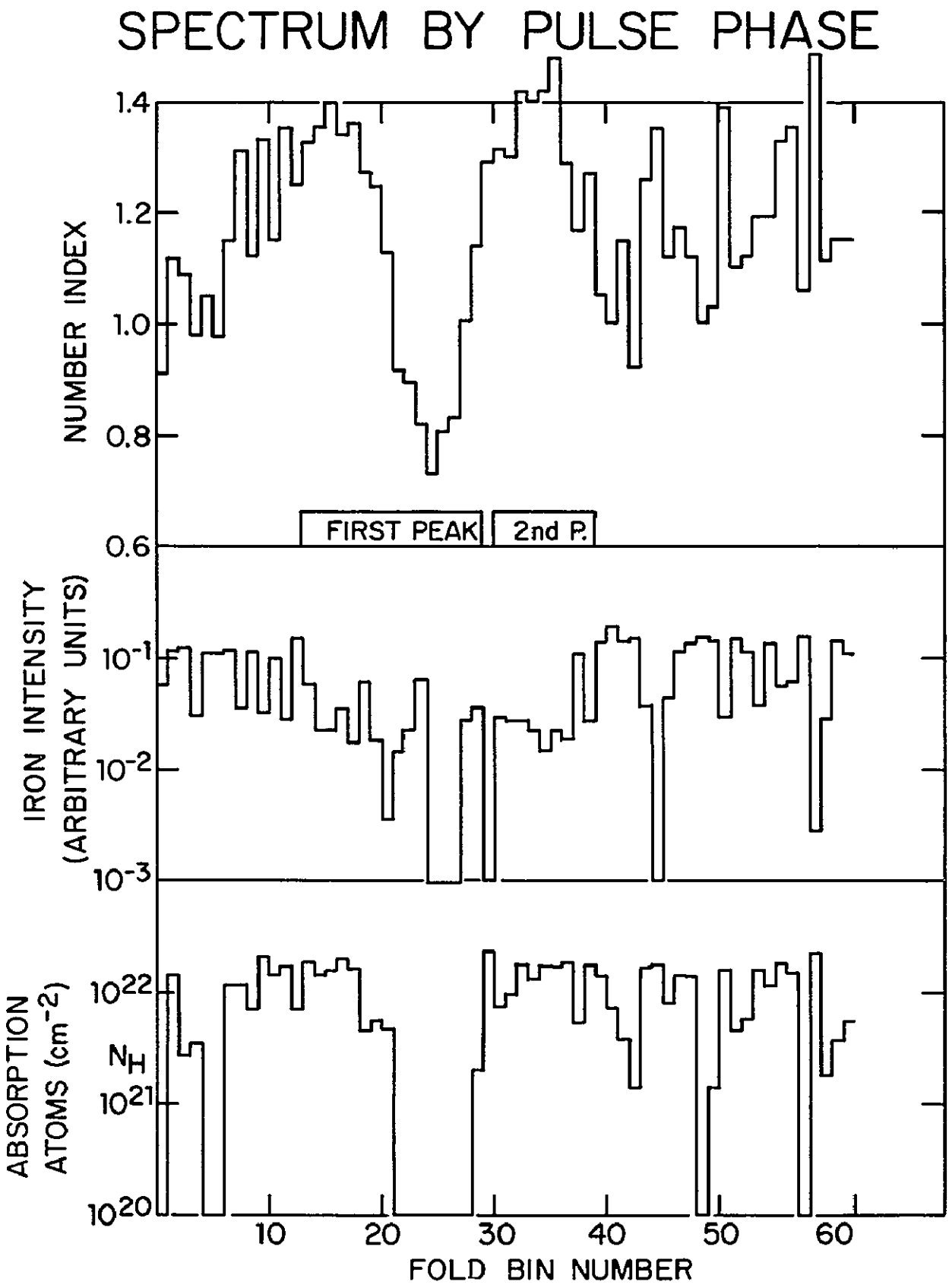
SPECTRUM BY PULSE PHASE
NUMBER INDEX
1.4
1.2
1.0
0.8
0.6
FIRST PEAK
2nd P.
IRON INTENSITY (ARBITRARY UNITS)
$10^{-1}$
$10^{-2}$
$10^{-3}$
ABSORPTION ATOMS ($cm^{-2}$)
$10^{22}$
$N_H$
$10^{21}$
$10^{20}$
10
20
30
40
50
60
FOLD BIN NUMBER

Figure 4-11

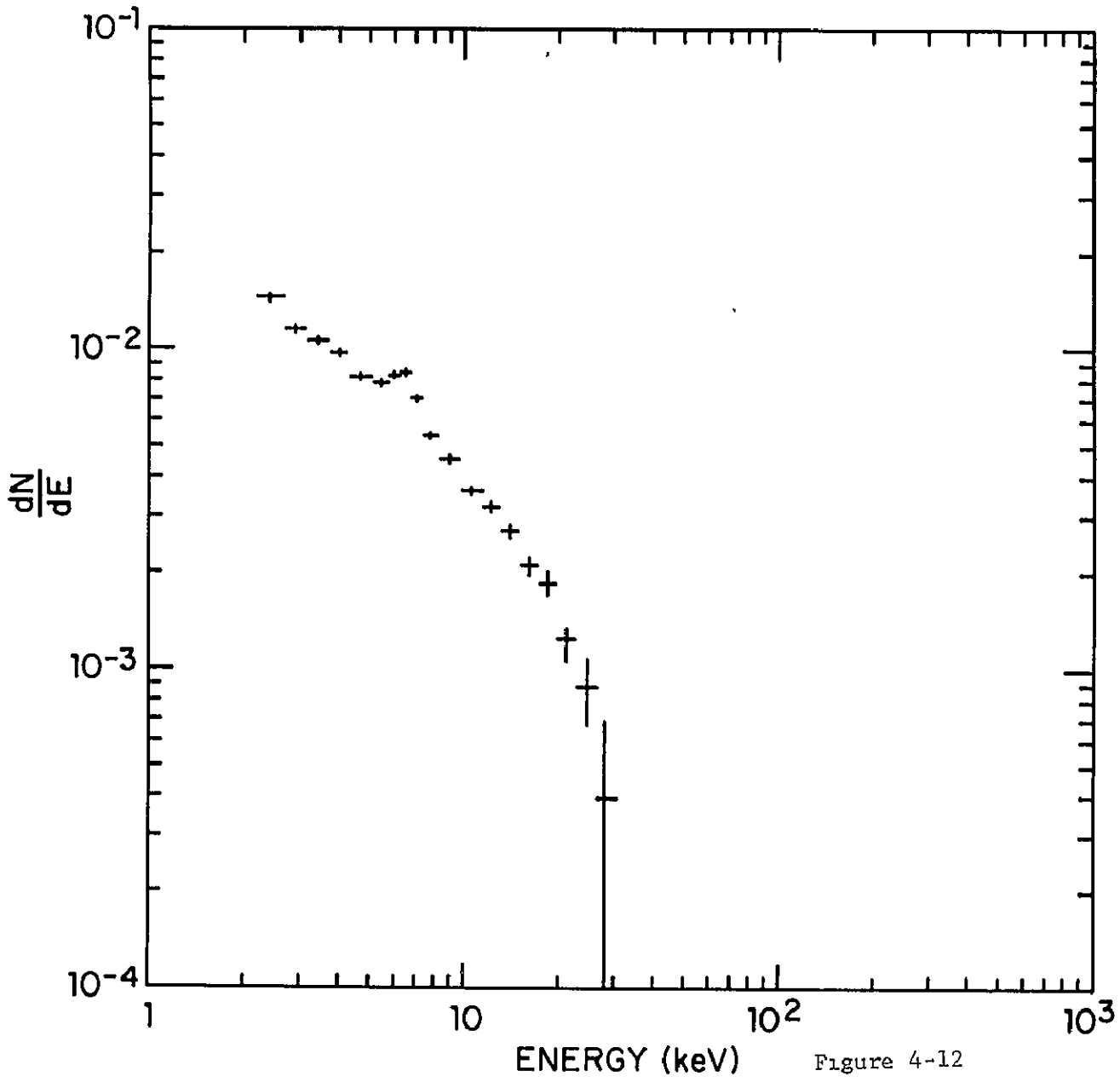
HER X-1 RL:OP SPECTRUM
$10^{-1}$
$10^{-2}$
$10^{-3}$
$10^{-4}$
$\frac{dN}{dE}$
1
10
$10^2$
$10^3$
ENERGY (keV)

Figure 4-12

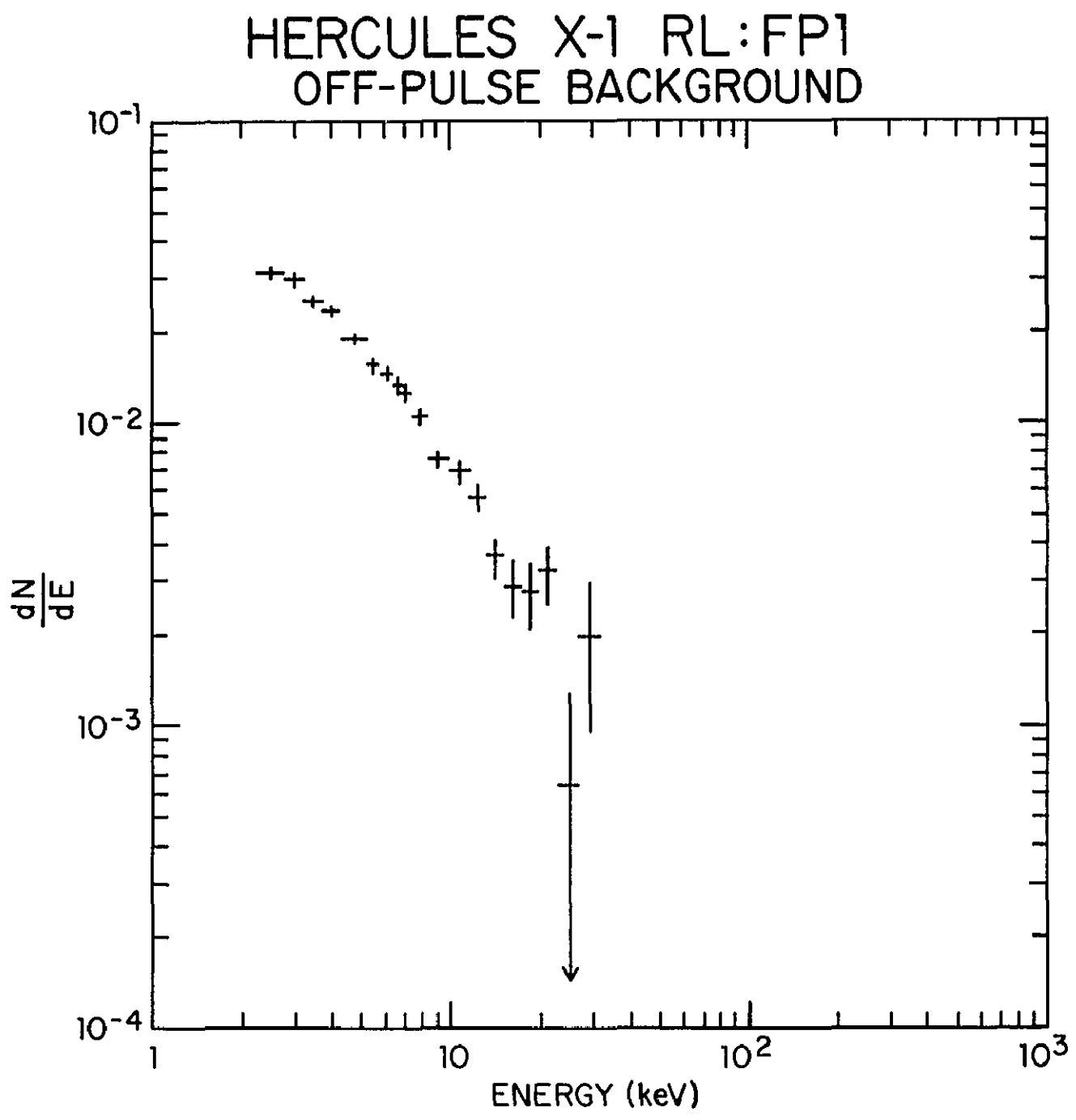
HERCULES X-1 RL:FP1
OFF-PULSE BACKGROUND
$10^{-1}$
$10^{-2}$
$10^{-3}$
$10^{-4}$
$\frac{dN}{dE}$
1
10
$10^2$
$10^3$
ENERGY (keV)

Figure 4-13

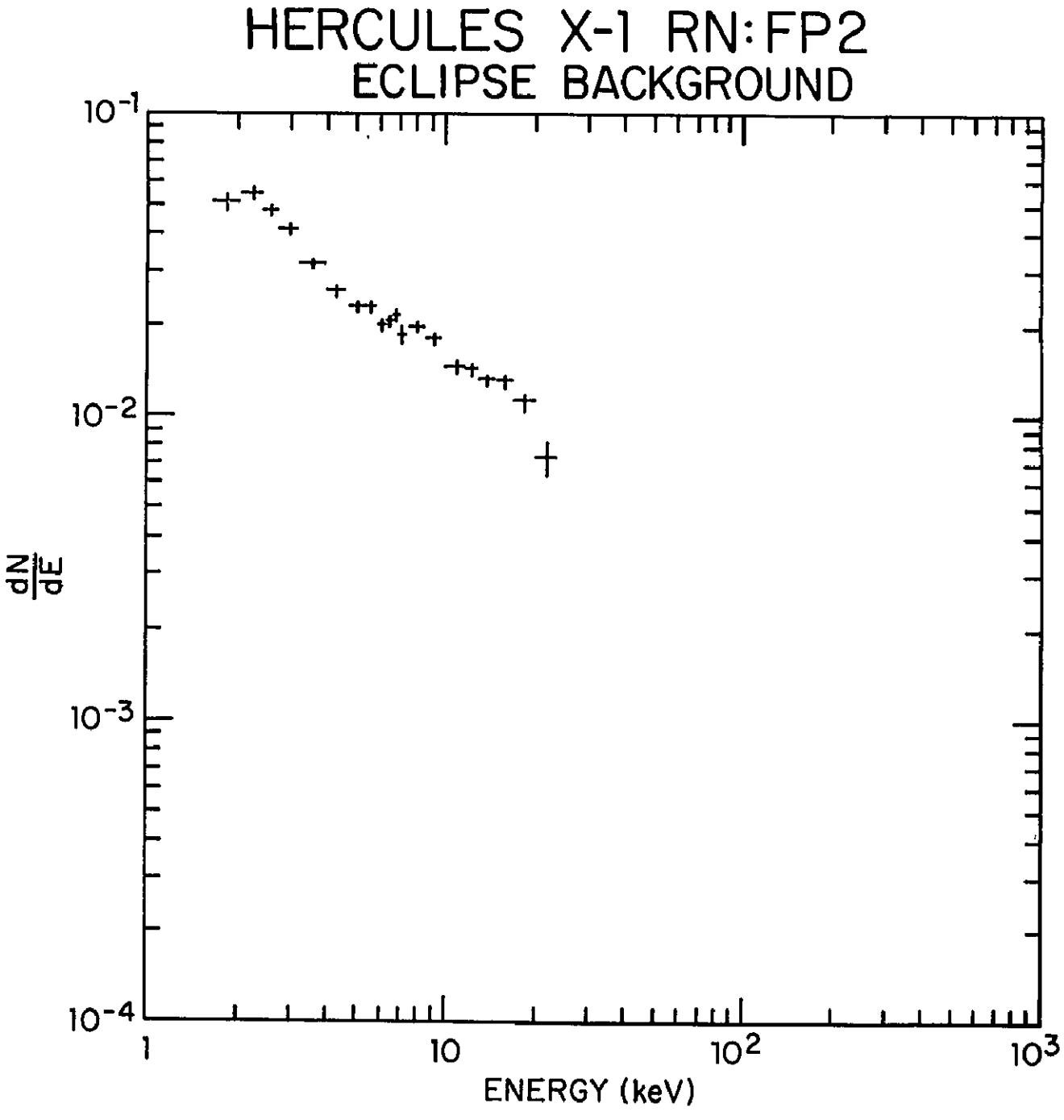
HERCULES X-1 RN:FP2
ECLIPSE BACKGROUND
$10^{-1}$
$10^{-2}$
$10^{-3}$
$10^{-4}$
$\frac{dN}{dE}$
1
10
$10^2$
$10^3$
ENERGY (keV)

Figure 4-14

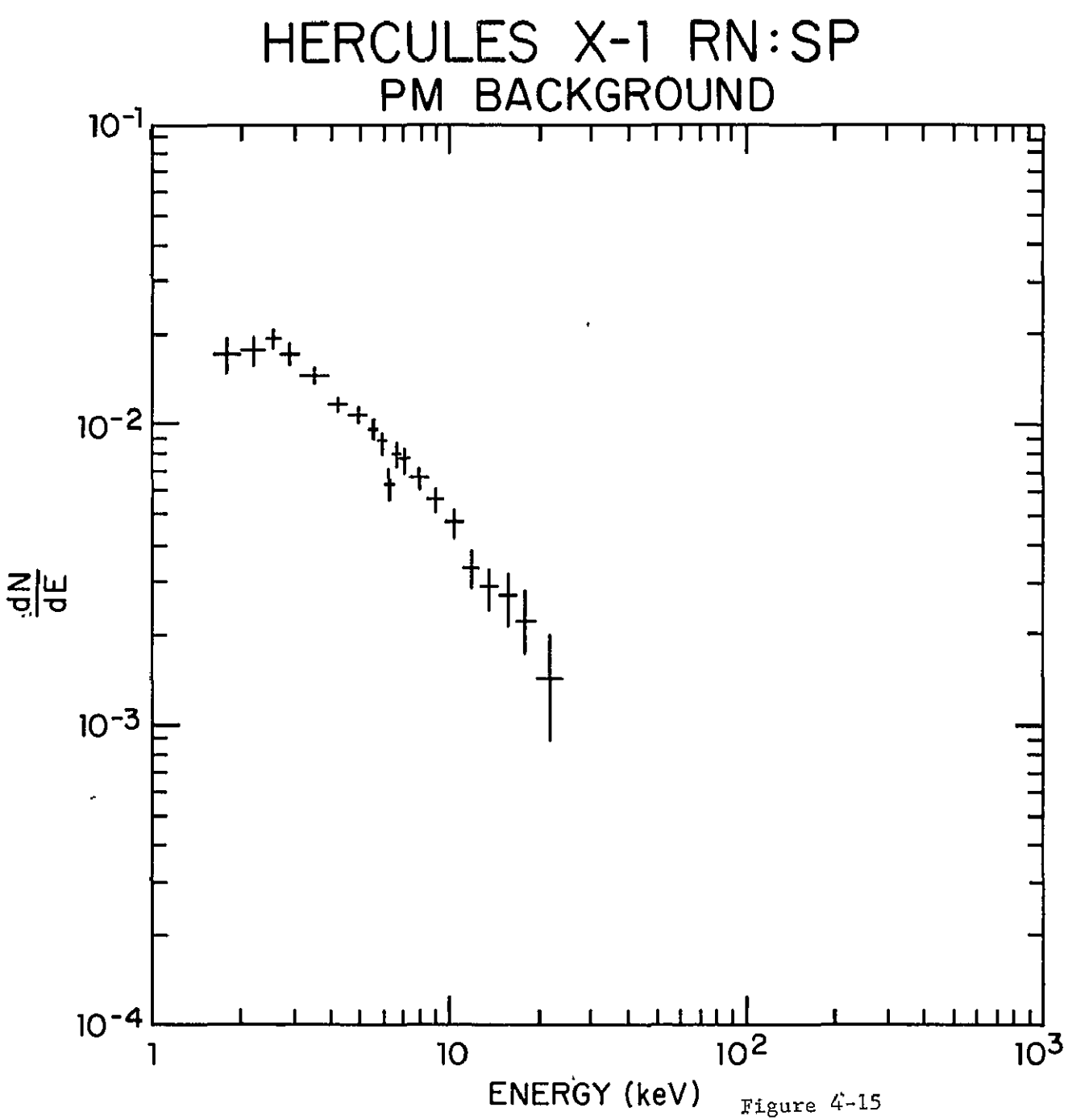
HERCULES X-1 RN:SP
PM BACKGROUND
$10^{-1}$
$10^{-2}$
$10^{-3}$
$10^{-4}$
$\frac{dN_p}{dE}$
1
10
$10^2$
$10^3$
ENERGY (keV)

Figure 4-15

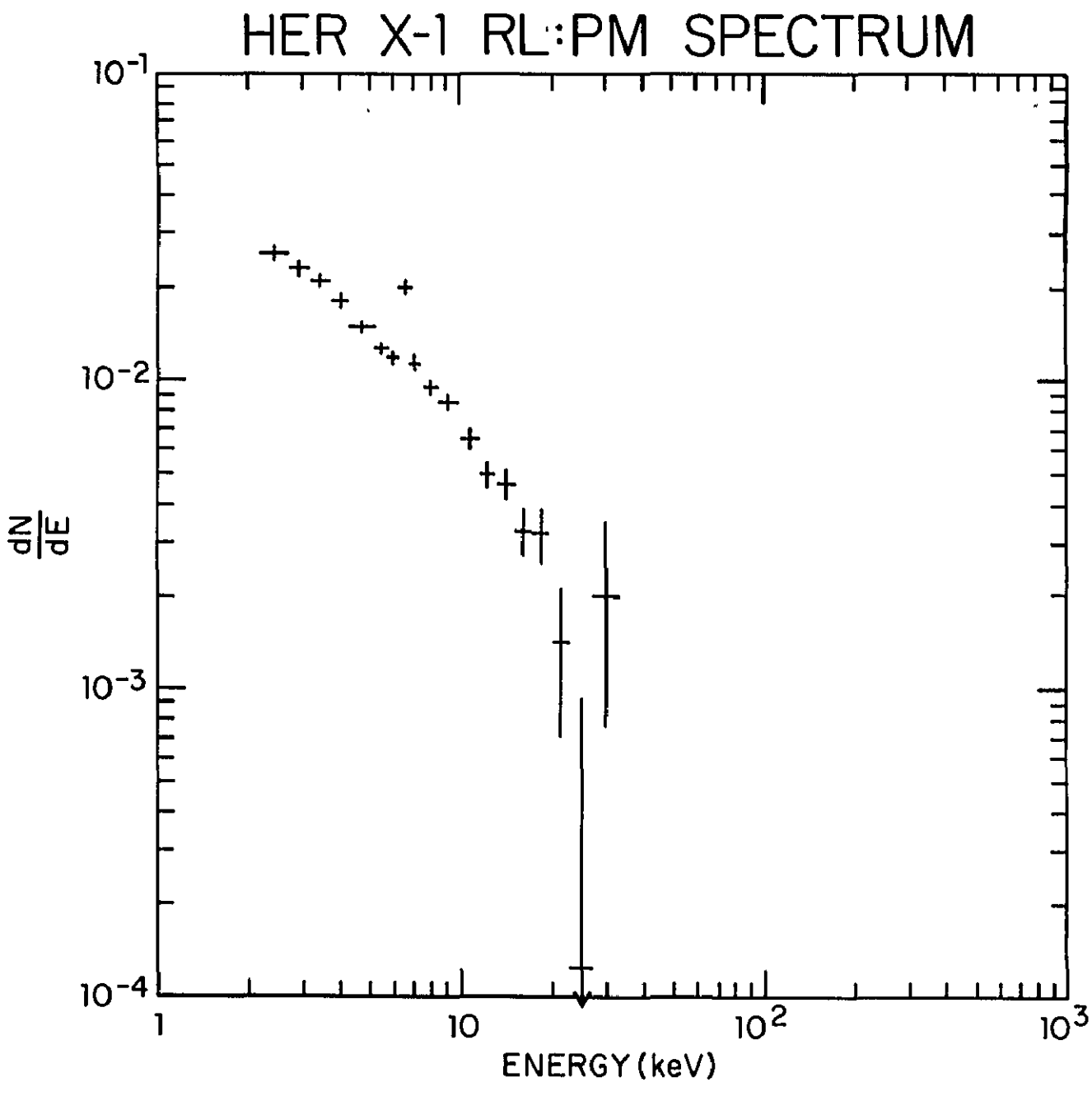
HER X-1 RL:PM SPECTRUM
$10^{-1}$
$10^{-2}$
$10^{-3}$
$10^{-4}$
dN/dE
1
10
$10^2$
$10^3$
ENERGY (keV)

Figure 4-16

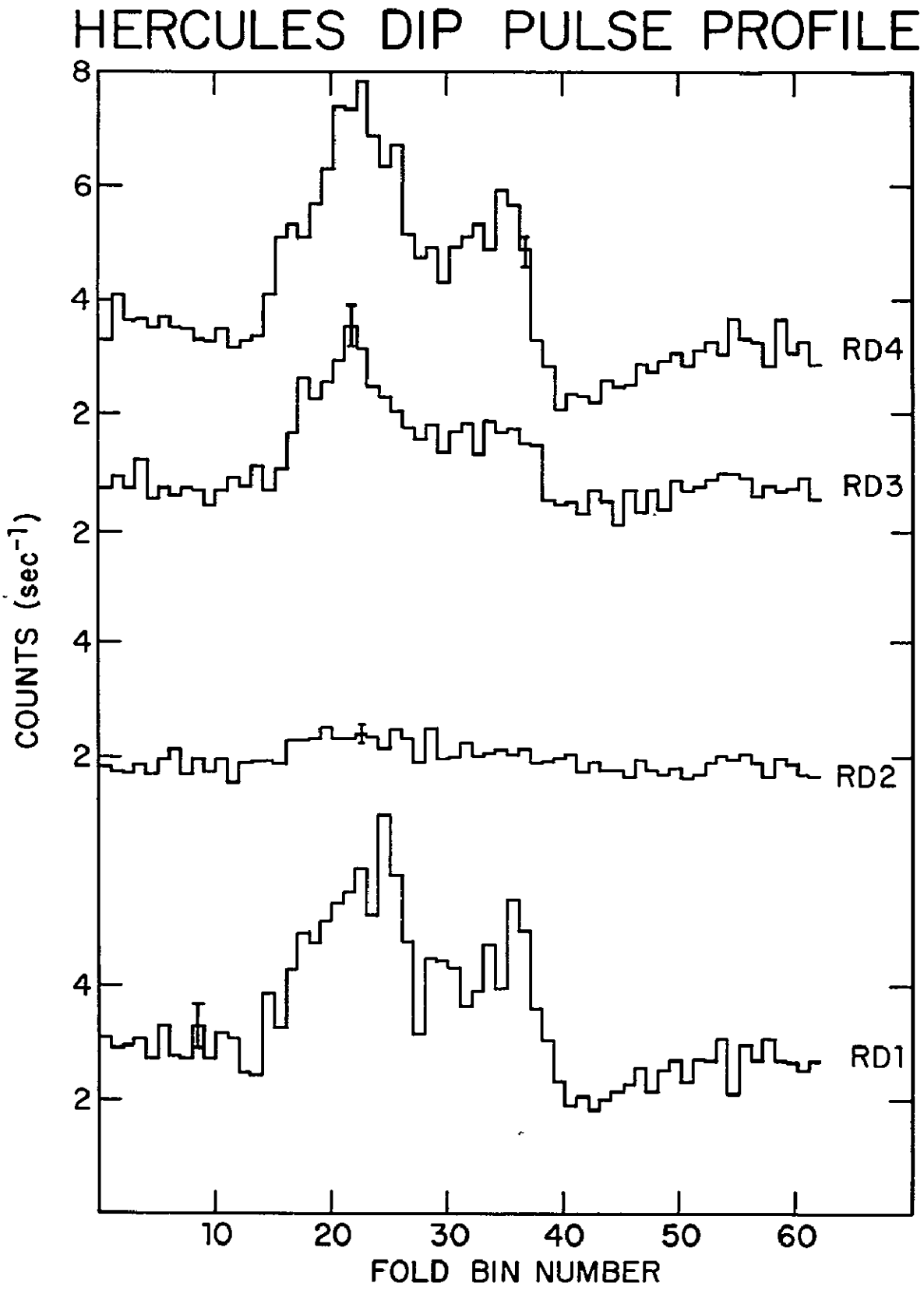
HERCULES DIP PULSE PROFILE
COUNTS (sec⁻¹)
8
6
4
2
2
4
2
4
2
RD4
RD3
RD2
RD1
10
20
30
40
50
60
FOLD BIN NUMBER

Figure 4-17

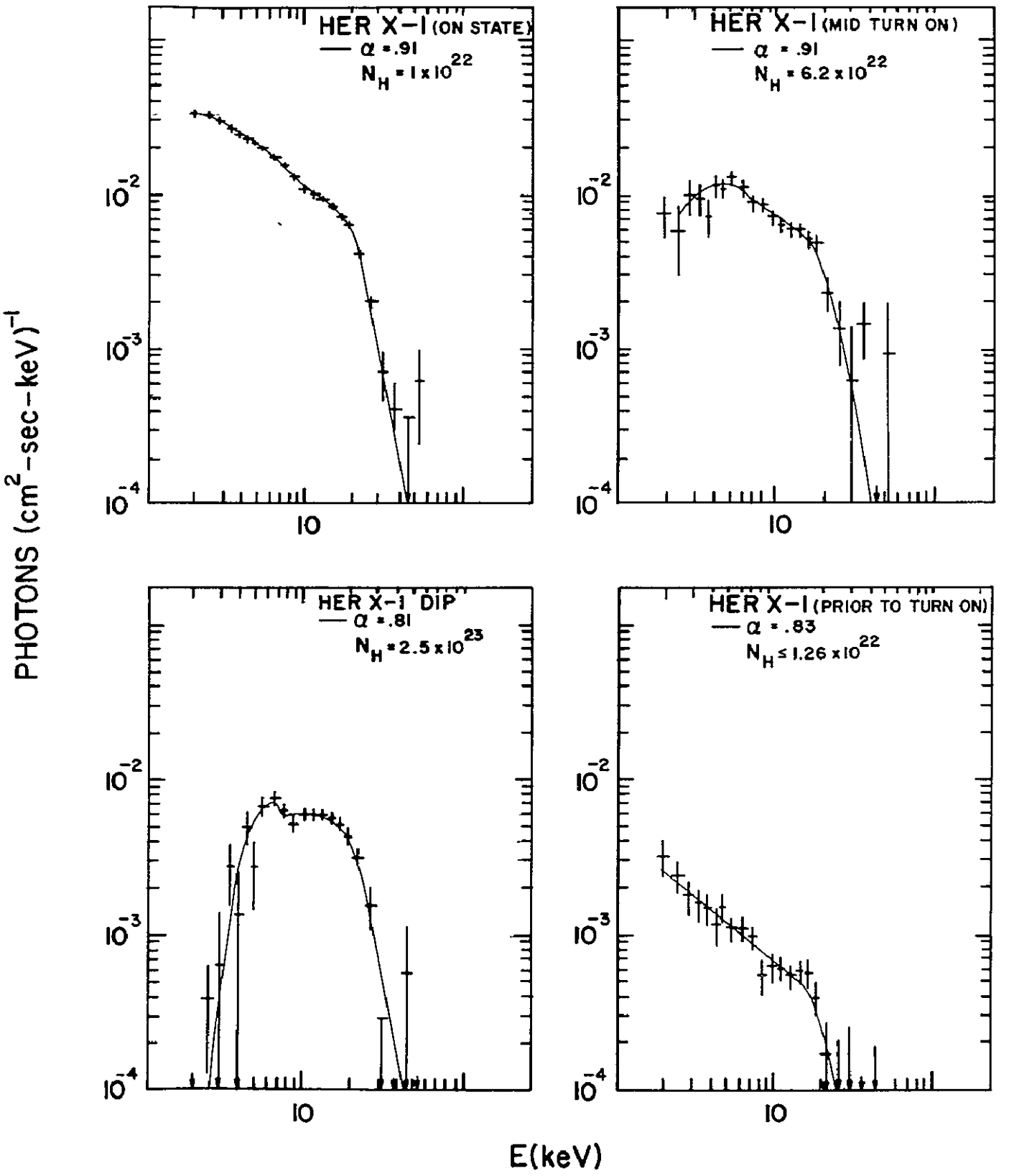
HER X-1 (ON STATE)
— α = .91
N_H = 1 x 10^22
HER X-1 (MID TURN ON)
— α = .91
N_H = 6.2 x 10^22
HER X-1 DIP
— α = .81
N_H = 2.5 x 10^23
HER X-1 (PRIOR TO TURN ON)
— α = .83
N_H ≤ 1.26 x 10^22
PHOTONS (cm^2-sec-keV)^-1
E(keV)
10^-2
10^-3
10^-4
10

Figure 4-18

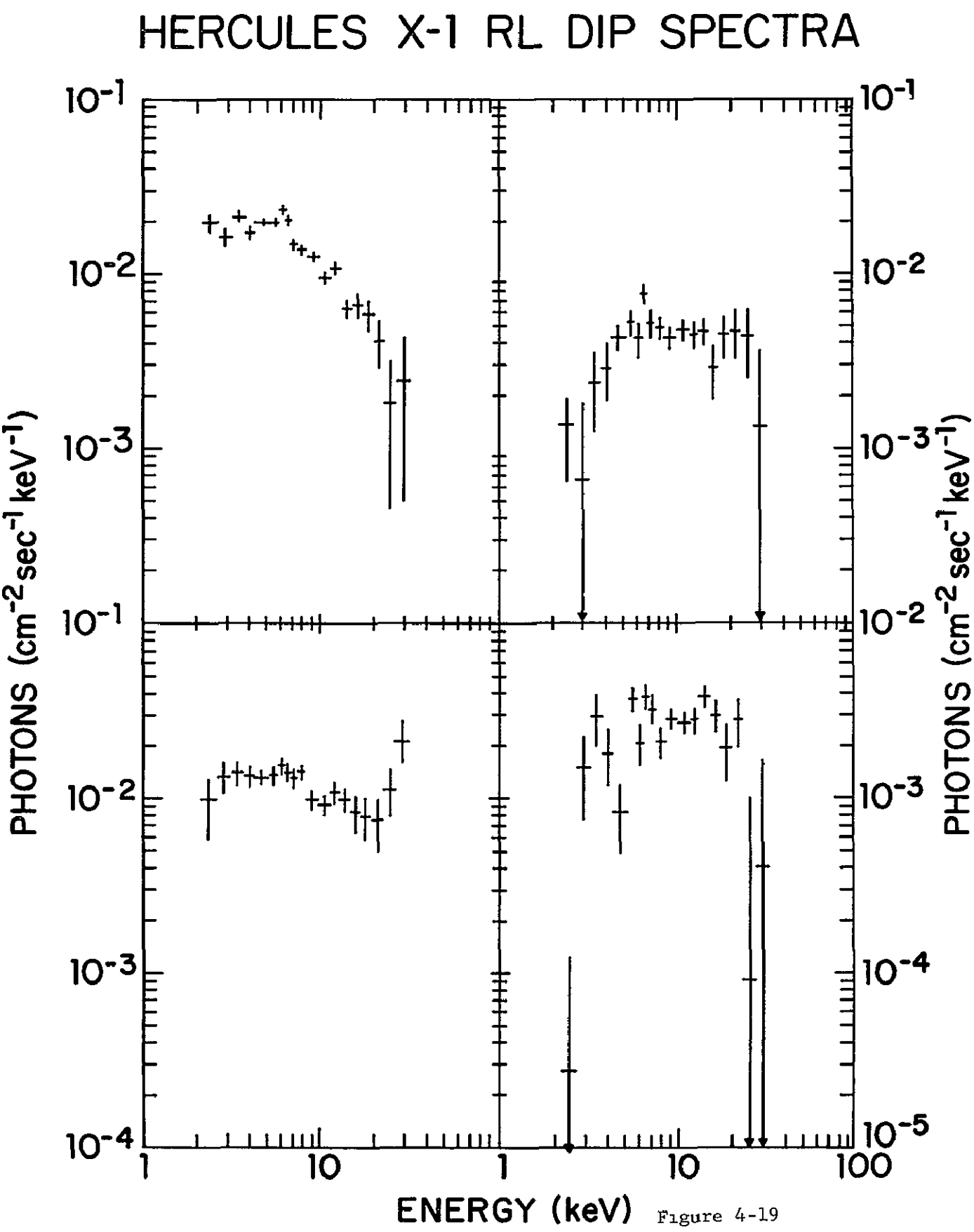
HERCULES X-1 RL DIP SPECTRA
PHOTONS (cm$^{-2}$sec$^{-1}$keV$^{-1}$)
PHOTONS (cm$^{-2}$sec$^{-1}$keV$^{-1}$)
ENERGY (keV)
$10^{-1}$
$10^{-2}$
$10^{-3}$
$10^{-4}$
$10^{-5}$
1
10
100

Figure 4-19

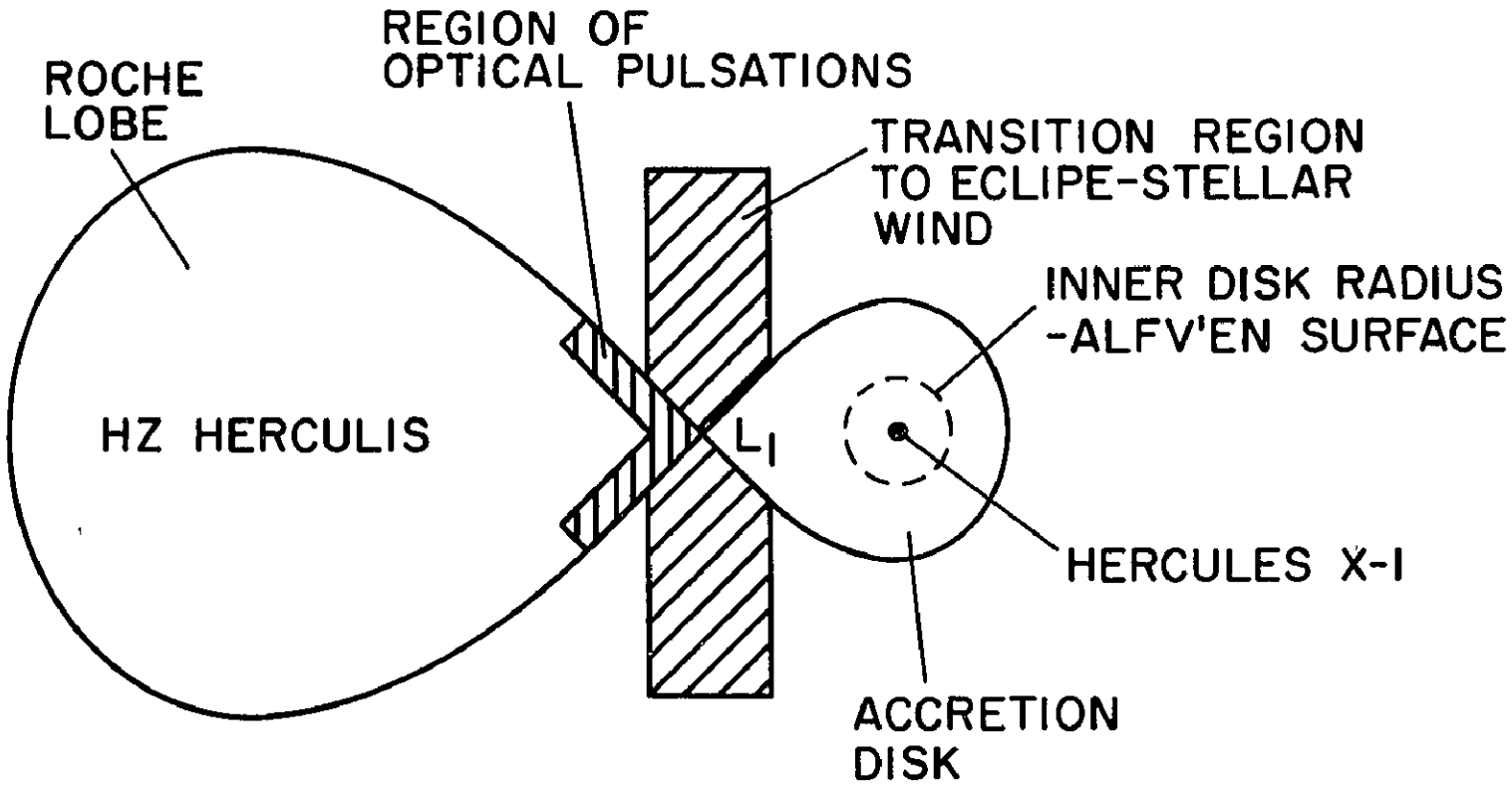
ROCHE
LOBE
REGION OF
OPTICAL PULSATIONS
TRANSITION REGION
TO ECLIPE-STELLAR
WIND
INNER DISK RADIUS
-ALFV'EN SURFACE
HZ HERCULIS
$L_1$
HERCULES X-I
ACCRETION
DISK

Figure 5-1

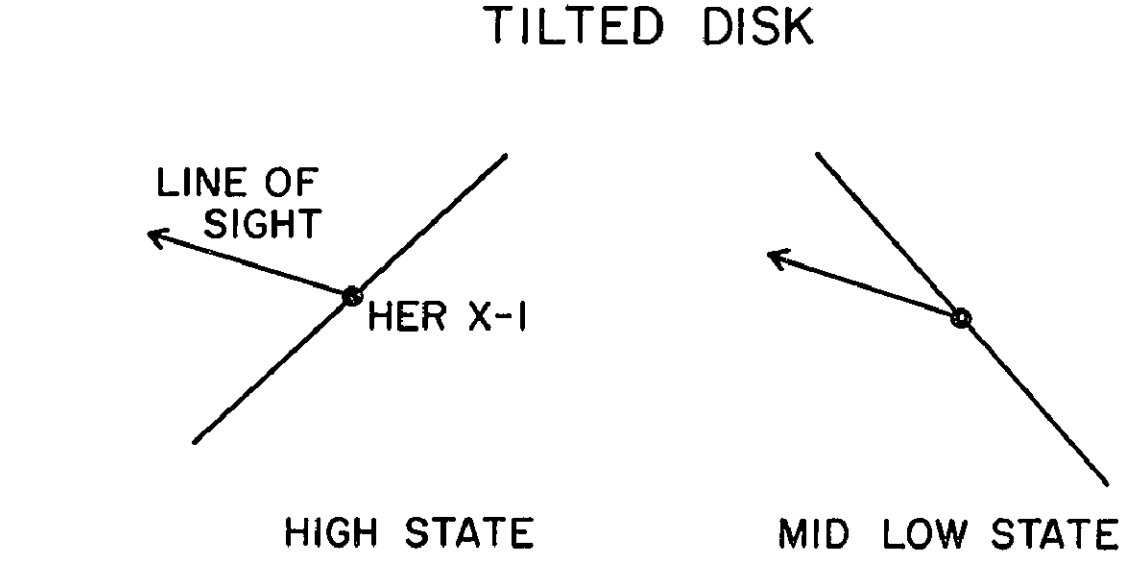
TILTED DISK
LINE OF SIGHT
HER X-1
HIGH STATE
MID LOW STATE
TWISTED DISK
PRECESSION
GRADUAL DECLINE
RAPID ONSET

Figure 5-2

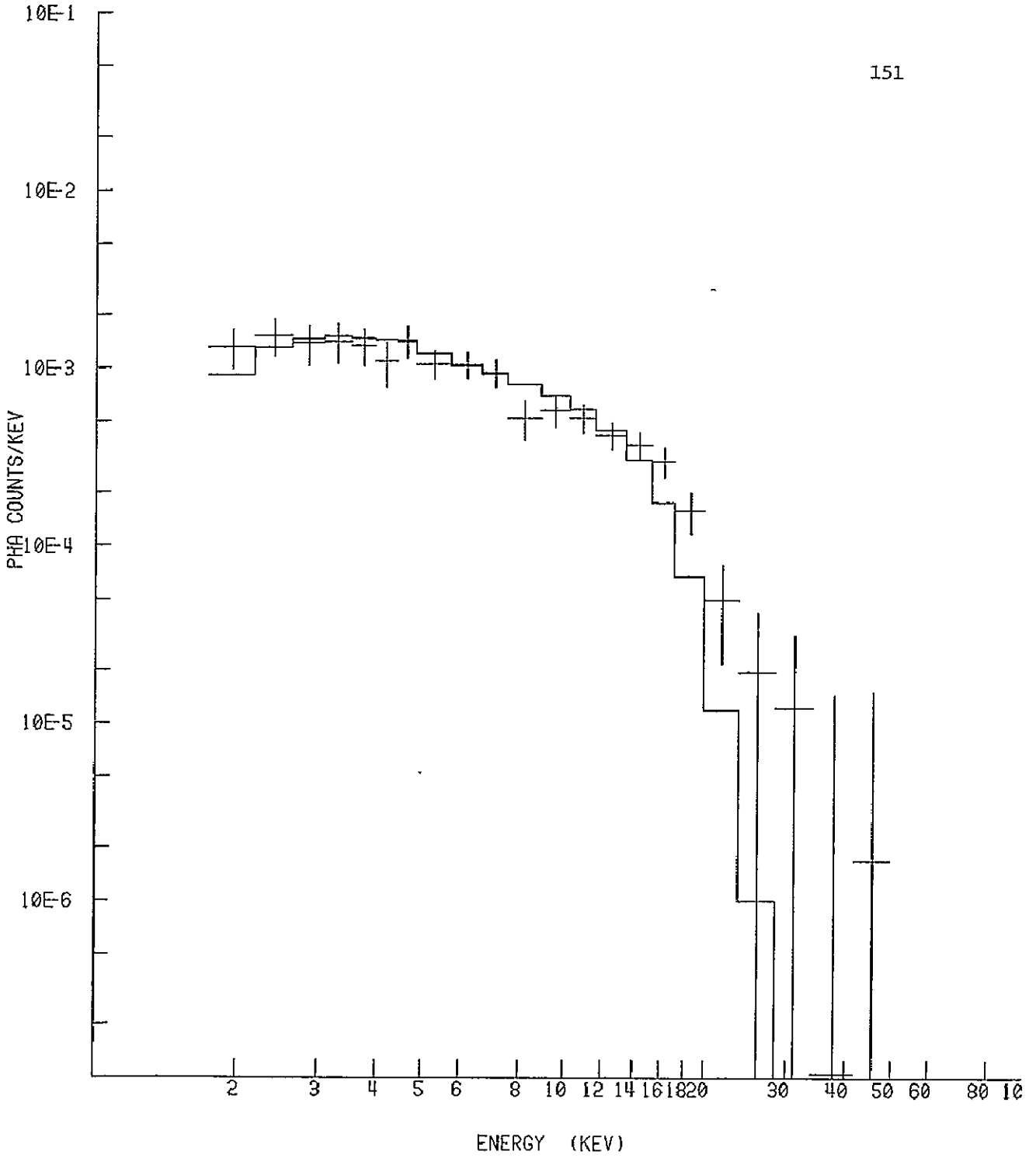


Figure 5-3

ABS(P4)/((E/P3)**P1+(E/P3)**P2)*CTAU(P5)

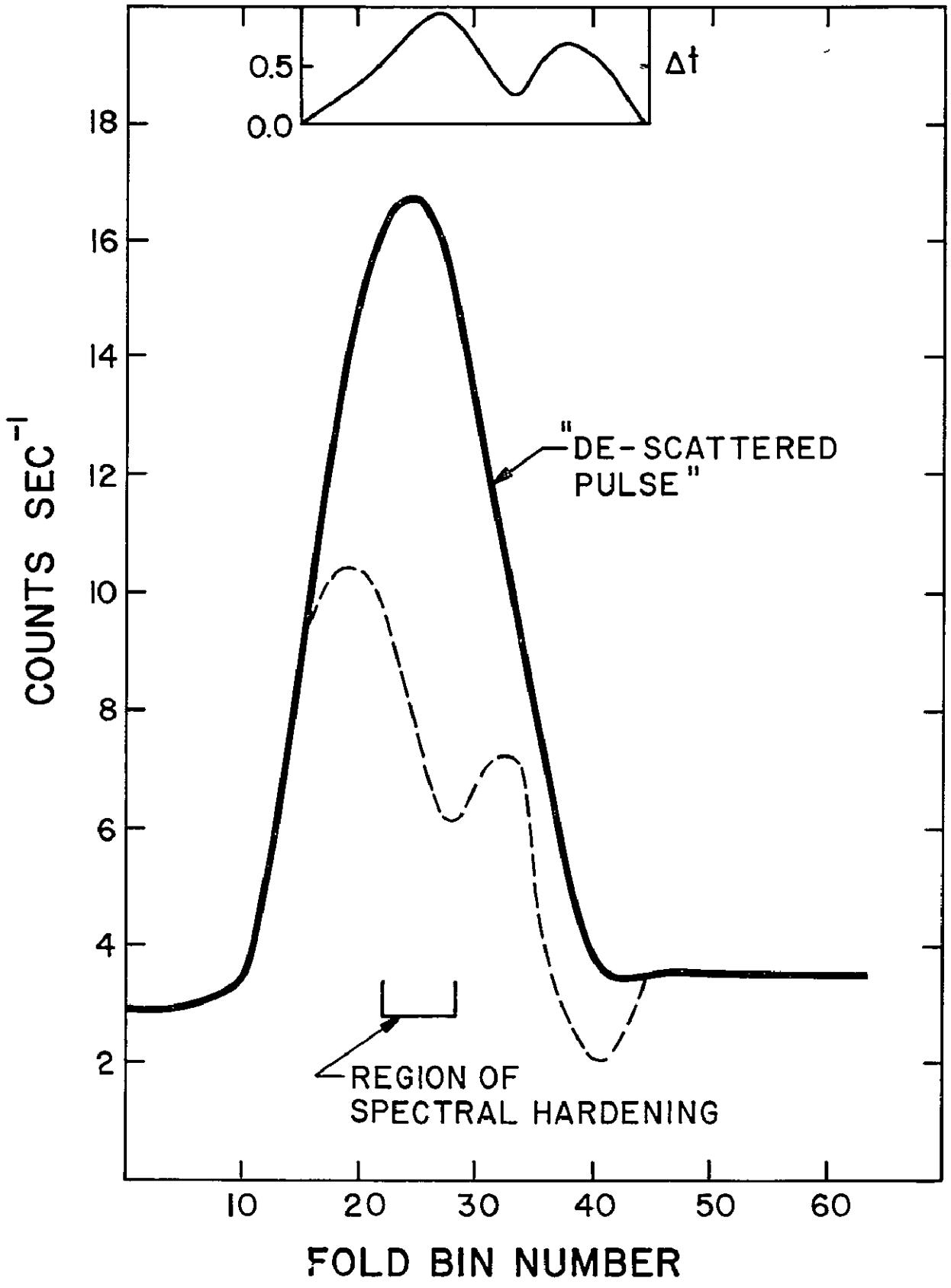


Figure 5-4

REPRODUCIBILITY OF THE ORIGINAL PAGE IS POOR

REPRODUCIBILITY OF THE
ORIGINAL PAGE IS POOR



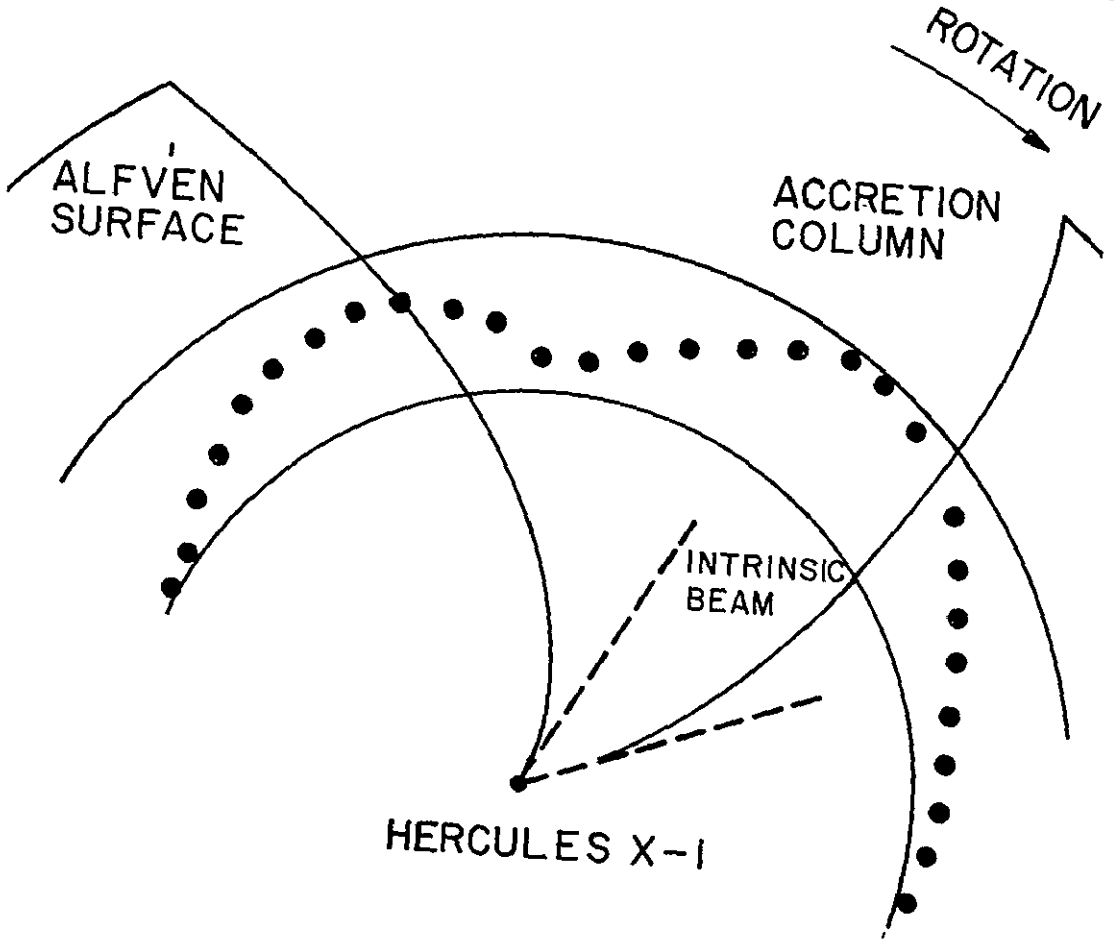


Figure 5-5

# OSO-I DETECTOR C-1

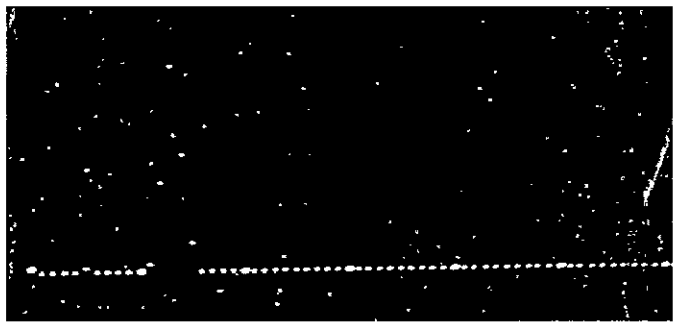

$Fe^{55}$; LAYER 1

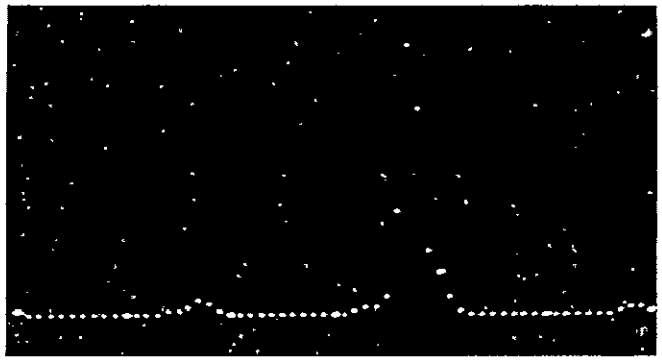

$Cd^{109}$; LAYER 1

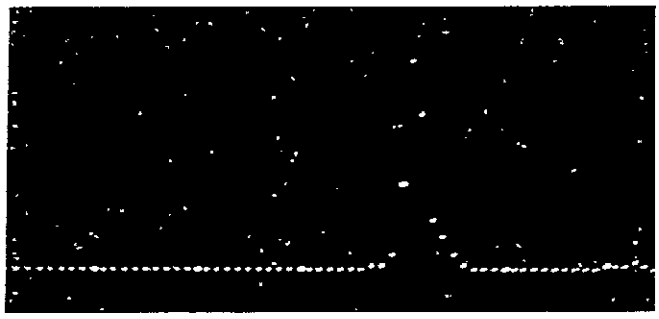

$Cd^{109}$; LAYER 2

Figure A-1